

INFORMATION TO USERS

This manuscript has been reproduced from the microfilm master. UMI films the text directly from the original or copy submitted. Thus, some thesis and dissertation copies are in typewriter face, while others may be from any type of computer printer.

The quality of this reproduction is dependent upon the quality of the copy submitted. Broken or indistinct print, colored or poor quality illustrations and photographs, print bleedthrough, substandard margins, and improper alignment can adversely affect reproduction.

In the unlikely event that the author did not send UMI a complete manuscript and there are missing pages, these will be noted. Also, if unauthorized copyright material had to be removed, a note will indicate the deletion.

Oversize materials (e.g., maps, drawings, charts) are reproduced by sectioning the original, beginning at the upper left-hand corner and continuing from left to right in equal sections with small overlaps.

Photographs included in the original manuscript have been reproduced xerographically in this copy. Higher quality 6" x 9" black and white photographic prints are available for any photographs or illustrations appearing in this copy for an additional charge. Contact UMI directly to order.

Bell & Howell Information and Learning
300 North Zeeb Road, Ann Arbor, MI 48106-1346 USA
800-521-0600

UMI[®]

UNIVERSITY OF CALIFORNIA
SANTA BARBARA

Three-dimensional Photonic Devices and Circuits

A dissertation submitted in partial satisfaction
of the requirements for the degree of

Doctor of Philosophy

in

Electrical and Computer Engineering

by

Bin Liu

Committee in Charge:

Professor John E. Bowers, Chairperson
Professor Daniel Blumenthal
Professor Nadir Dagi
Professor Ali Shakouri

March 2000

UMI Number: 3001462

Copyright 2000 by
Liu, Bin

All rights reserved.

UMI[®]

UMI Microform 3001462

Copyright 2001 by Bell & Howell Information and Learning Company.

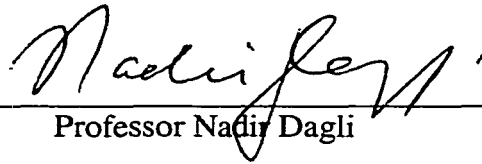
All rights reserved. This microform edition is protected against
unauthorized copying under Title 17, United States Code.

Bell & Howell Information and Learning Company
300 North Zeeb Road
P.O. Box 1346
Ann Arbor, MI 48106-1346

The dissertation of Bin Liu is approved:



Professor Dan Blumenthal



Professor Nadir Dagli



Professor Ali Shakouri



Professor John E. Bowers, Chairperson

March 2000

Three-dimensional Photonic Devices and Circuits

Copyright © by

Bin Liu

All rights reserved

March 2000

Department of Electrical and Computer Engineering

University of California, Santa Barbara

Santa Barbara, CA 93106

Acknowledgements

To get my Ph. D. degree at the beginning of a new millennium is really exciting. A lot of people helped me to make it happen.

First, I would like to thank my advisor Professor John E. Bowers. He provided me the great opportunity and the financial support to begin my Ph.D. at UCSB. During the past years, he has always given me the continuous encouragement and a free research environment.

Professor Ali Shakouri deserves my special thanks. Since I came to UCSB, Ali has given me a lot of helps, from teaching me to use BPM to correcting my English mistakes. Without his help, I would not move my research so smoothly and fruitfully. I also thank the other members of the committee, Professor Dan Blumenthal and Professor Nadir Dagli for their helpful discussions and suggestions.

The high quality material is the key for the successful devices. Fortunately, we have several excellent growers in our group. Dr. Abraham Patrick grew more than 30 InP/InGaAsP wafers for me in last three years. I greatly appreciate him for his contribution. I also thank Dr. Yi-Jen Chiu for his effort in MBE grown wafers.

I am also indebted to many people to have helped me during the past years. Dr. Near Margalit trained me wafer fusion process. Dan Cohen and Dr. Shengzhong Zhang taught me how to take SEM pictures. Thomas Liljeberg and Dr. Greg Fish introduced me the dry etching. Dr. Andrew Jackson installed the temperature controlled stage for measurement. Dr. Shengzhong Zhang helped me a lot to collect the data. I would like to thank other groupmates and officemates for their help and friendship. They are Alexis Black, Adil Karim, Chris LaBounty, Kehl Sink, Dr. Joachim Piprek, Maura Rabum, Volkam Kaman, Daniel Lasaosa, Xiaofeng Fan, Shanhua Xue, Gehong Zeng, Helen Reese, Kian-Giap Gan, Staffan

Bjorlin, Dr. Weishu Wu, Chris Scholz, Scott Humphries, Lavanya Rau. I also appreciate the help from Vickie Edwards, Christina Loomis and Diana Thurman.

Prior to coming to UCSB, I worked at Shanghai Institute of Optics and Fine Mechanics (SIOM), Chinese Academy of Sciences. Professor Zujie Fang introduced me to this field and taught me the basic skills for the fabrication of optoelectronic devices. I benefited a lot from the experiences I got during that period. I met Dr. Tien-Pei Lee, who was the former director of Optoelectronic Technology Research of Bell Communications Research (Bellcore) in Red Bank, NJ, in 1994 and 1995. Dr. Lee suggested me to do my doctoral work at UCSB. His recommendation led me to join Professor John Bowers' group finally. I want to thank him for his kindness.

My parents put their hearts on my brother and me. Without their support, I cannot imagine that I could have had the chance to get my Ph.D. in United States. I owe them a lot. Finally, I would like to thank my wife, Hong Yuan. She always brings me a happy life and lets me have more time to concentrate on my work. My Ph.D. also belongs to her.

This dissertation is dedicated to
my lovely daughter Xinyue Liu

Vita

September 1986 - July 1990	B.S., Electrical Engineering ZheJiang University, China
September 1992 - July 1995	M.S., Optoelectronics Shanghai Institute of Optical and Fine Mechanics, Chinese Academy of Sciences
September 1996 - March 2000	Ph.D., Electrical Engineering University of California, Santa Barbara

Publications in Technical Journals

- [1] B. Liu, A. Shakouri, P. Abraham, and John E. Bowers, "A wavelength multiplexer using cascaded 3D vertical couplers," *Appl. Phys. Lett.*, vol. 76, pp. 282-284, 2000.
- [2] B. Liu, A. Shakouri, P. Abraham, and John E. Bowers, "Optical add/drop multiplexers based on X-crossing vertical coupler filters," *IEEE Photon. Technol. Lett.*, 2000 (to be published).
- [3] B. Liu, A. Shakouri, and J. E. Bowers, "Characteristic equations for different ARROW structures," *Optical and Quantum Electronics*, vol. 31, pp. 1267-1276, 1999.
- [4] B. Liu, A. Shakouri, P. Abraham, and J. E. Bowers, "Vertical coupler with separated inputs and outputs fabricated using double-sided process," *Electronics Letters*, vol. 35, pp. 1552-4, 1999.
- [5] B. Liu, A. Shakouri, P. Abraham, and J. E. Bowers, "Push-pull fused vertical coupler switch," *IEEE Photonics Technology Letters*, vol. 11, pp. 662-4, 1999.
- [6] B. Liu, A. Shakouri, P. Abraham, Y. J. Chiu, and J. E. Bowers, "Fused III-V vertical coupler filter with reduced polarisation sensitivity," *Electronics Letters*, vol. 35, pp. 481-2, 1999.
- [7] B. Liu, A. Shakouri, P. Abraham, Y. J. Chiu, S. Zhang, and J. E. Bowers, "Fused InP-GaAs vertical coupler filters," *IEEE Photonics Technology Letters*, vol. 11, pp. 93-5, 1999.
- [8] A. Shakouri, B. Liu, P. Abraham, and J. E. Bowers, "3D photonic integrated circuits for WDM applications," *Critical Reviews of Optical Science and Technology*, vol. CR71, pp. 181-204, 1999.
- [9] B. Liu, A. Shakier, P. Abraham, and J. E. Bowers, "Fused vertical coupler switches," *Electronics Letters*, vol. 34, pp. 2159-61, 1998.
- [10] B. Liu, A. Shakouri, P. Abraham, K. Boo-Gyoun, A. W. Jackson, and J. E. Bowers, "Fused vertical couplers," *Applied Physics Letters*, vol. 72, pp. 2637-8, 1998.

- [11] A. Shakouri, B. Liu, K. Boo-Gyoun, P. Abraham, A. W. Jackson, and A. C. Gossard, "Wafer-fused optoelectronics for switching," *Journal of Lightwave Technology*, vol. 16, pp. 2236-42, 1998.
- [12] K. Boo-Gyoun, A. Shakouri, B. Liu, and J. E. Bowers, "Improved extinction ratio in ultra short directional couplers using asymmetric structures," *Japanese Journal of Applied Physics, Part 2 (Letters)*, vol. 37, pp. L930-2, 1998.
- [13] B. Liu, R. Qiu, and Z. Fang, "Theoretical calculation of gain and threshold current density for InGaN quantum well lasers," *Chinese Journal of Lasers*, vol. A25, pp. 1-6, 1998.
- [14] D. Zhu, Z. Wang, J. Liang, B. Xu, Z. Zhu, J. Zhang, Q. Gong, C. Jin, L. Cong, X. Hu, Q. Han, Z. Fang, B. Liu, and Y. Tu, "High-power, high-temperature operation of AlGaAs single quantum well lasers," *Chinese Journal of Semiconductors*, vol. 18, pp. 391-4, 1997.
- [15] B. Liu, Z. J. Fang, "Modified rate equation for quantum well lasers," *ACTA OPTICA SINICA*, Vol.16, pp. 274-7, 1996.
- [16] B. Liu, Z. J. Fang, "Mode characteristics of a corner reflector coupled InGaAs strained layer quantum well phased array," *ACTA OPTICA SINICA*, Vol. 15, 1996.
- [17] H. Zhao, H. Ding and B. Liu, "Experimental study on photosensitivity in hydrogen loaded fibers," *Sino-French workshop on fiber and integrated optics*, pp. 95-7, 1995.
- [18] B. Liu and Z. J. Fang, "Microcavity Lasers," *Overseas Lasers*, No. 10, 1992.
- [19] B. Liu and Z. J. Fang, "Perturbation theory of uniform phase-locked arrays," *Chinese J. Quantum Electronics*, Vol. 9, pp. 253-9, 1992.
- [20] B. Liu, *et. al*, "Experimental study of multi-quantum well lasers grown by MBE," *Semiconductor Information*, No. 6, pp. 76-8, 1991.

Conference Presentations

- [1] B. Liu, A. Shakouri , P. Abraham and John E. Bowers, "Optical add/drop multiplexers based on X-crossing vertical coupler filters," OFC'2000, Baltimore, Maryland, March 7-10, 2000.
- [2] B. Liu, A. Shakouri , P. Abraham and John E. Bowers, "Wavelength multiplexers by cascading 3D vertical couplers," LEOS'99, San Francisco, CA, November 8-11.
- [3] John E. Bowers, G. Fish, L. Coldren, B. Liu, A. Shakouri "InGaAsP optical cross connect technologies," OSA annual meeting, Santa Clara, CA, September 26-30, 1999.
- [4] B. Liu, A. Shakouri , P. Abraham and John E. Bowers, "Push-pull fused vertical coupler switch," OFC'99, San Diego, CA, March 21-25.
- [5] B. Liu, A. Shakouri , P. Abraham, Y. J. Chiu, S. Zhang and John E. Bowers, "InP-GaAs fused vertical coupler filters," LEOS'98, Orland, FL, December 1-4.
- [6] B. Liu, A. Shakouri , P. Abraham and John E. Bowers, "Fused vertical couplers," OFC'98, San Jose, CA, Feb. 22-27.
- [7] B. G. Kim, A. Shakouri, B. Liu, and John E. Bowers, "Improved Extinction Ratio in Ultra Short Directional Couplers Using Asymmetric Structures," Integrated Photonics Research Conference Proceedings, Victoria, British Colomibia, Canada, March 30- April 1, 1998.
- [8] J. E. Bowers, N. Margalit, K. A. Black, A. Hawkins, B. Liu, A. Shakouri, P. Abraham and E. Hu, "Wafer Fused Optical Devices," IPR'98. Victoria, British Colomibia, Canada, March 30- April 1, 1998.
- [9] B. Liu, A. Shakouri and John E. Bowers, "Fused vertical directional couplers," LEOS'97, San Francisco, CA, November 11-13.

Abstract

Three-dimensional Photonic Devices and Circuits

By

Bin Liu

Photonic integrated circuits have held the promise that the success of electronic integrated circuits could be transferred to the realm of optics. The complexity of both electronic and photonic ICs comes from a combination of pushing the performance of individual components and increasing the complexity of their interconnections. Compared to the development of microelectronic ICs, one missing key technology in PICs is the three-dimensional optical interconnection. The major breakthrough for PICs can be expected when technology is ready for 3D multilevel photonic devices and circuits with an increased functionality due to large-scale integration.

In this dissertation, we explore the possibility of the fabrication of 3D photonic devices and circuits using the wafer bonding technique. Several novel 3D multilevel photonic devices and circuits for WDM applications are demonstrated. They include wafer fused vertical coupler with a very short coupling length, push-pull coupler switch by inverting the crystal symmetry macroscopically, multi-channel wavelength multiplexers using cascaded vertical couplers, and optical add/drop multiplexers based on X-crossing vertical coupler filters. The detailed design, fabrication and characterization of these devices are presented in this dissertation. Since wafer bonding gives us an extra degree of freedom for the integration of different materials and structures, it is a potential and viable tool for future complex 3D photonic devices and circuits.

Table of Contents

1 INTRODUCTION	1
1.1 WAVELENGTH DIVISION MULTIPLEXING NETWORKS	1
1.2 COMPARISON OF ELECTRONIC IC AND PHOTONIC IC	4
1.3 3D MULTILEVEL PHOTONIC DEVICES AND CIRCUITS	9
REFERENCES.....	13
2 WAFER BONDING	15
2.1 HISTORY OF WAFER BONDING.....	15
2.2 APPLICATIONS OF WAFER BONDING.....	16
2.3 WAFER BONDING PROCESS	18
2.4 OPTICAL LOSS AT BONDED INTERFACE	20
2.5 SUMMARY	27
REFERENCES.....	28
3 DESIGN OF WAVEGUIDE DEVICES	31
3.1 INTRODUCTION.....	31
3.2 TRANSFER MATRIX METHOD	31
3.3 EFFECTIVE INDEX METHOD.....	35
3.4 COUPLED MODE THEORY AND NORMAL MODE THEORY	36
3.5 BEAM PROPAGATION METHOD (BPM).....	40
3.6 DESIGN OF VERTICAL COUPLERS	40
3.7 SUMMARY	48
REFERENCES.....	49
4 FUSED VERTICAL COUPLER AND SWITCH	51

4.1 VERTICAL COUPLER AND HORIZONTAL COUPLER	51
4.2 SIMULATION OF 3D VERTICAL COUPLERS	54
4.3 FUSED VERTICAL COUPLER.....	59
4.4 FUSED VERTICAL COUPLER SWITCH.....	62
4.5 VERTICAL COUPLER WITH SEPARATED INPUTS AND OUTPUTS.....	78
4.6 SUMMARY OF THE CHAPTER	80
REFERENCES.....	81
5 VERTICAL COUPLER BASED WAVELENGTH MULTIPLEXERS.....	85
5.1 INTRODUCTION.....	85
5.2 DESIGN OF VERTICAL COUPLER MULTIPLEXER	88
5.3 DOUBLE-SIDED WAFER PROCESSING	97
5.4 MULTI-CHANNEL WAVELENGTH MULTIPLEXERS	98
5.5 WAVELENGTH SELECTIVE SWITCH	109
5.5 SUMMARY AND DISCUSSION	111
REFERENCES.....	112
6 X-CROSSING VERTICAL COUPLER ADD/DROP FILTER	115
6.1 OVERVIEW OF OPTICAL FILTERS	115
6.2 DESIGN OF X- CROSSING VERTICAL COUPLER FILTERS	117
6.3 DEVICE FABRICATION	127
6.4 RESULTS.....	129
6.5 FUTURE WORK.....	138
6.6 SUMMARY	148
REFERENCES.....	149
7 SUMMARY	153
REFERENCES.....	157

APPENDIX A WAVEGUIDE LOSS MEASUREMENT	159
REFERENCES.....	162
APPENDIX B CHARACTERISTIC EQUATIONS FOR DIFFERENT ARROW STRUCTURES.....	163
B.1 INTRODUCTION	163
B.2 CHARACTERISTIC EQUATIONS	164
B.3 EXAMPLES	167
B.4 CONCLUSION.....	170
REFERENCES.....	171

Chapter 1

Introduction

1.1 Wavelength Division Multiplexing Networks

During the last decade, we have witnessed an explosive growth of the Internet and a rapid increase of data and voice traffic in telecommunications and computer networks. A conservative estimate of Internet traffic growth is that it will double every six months. If this growth rate continues, the aggregate bandwidth required for the Internet by 2005 in the United States will be in excess of 280Tb/s [1]. This current unprecedented demand for network capacity drives revolutionary changes of communication networks: Optical wavelength division multiplexing (WDM) [2-4] networking is replacing the conventional communication networks. WDM systems combine multiple wavelengths so they can be amplified as a group and transported over a single fiber. Using a WDM system for capacity expansion offers a more economical and efficient way to increase transport capacity without upgrading the existing fibers or terminal equipment. In addition, it allows room for future capacity expansion to the full bandwidth of the existing fiber plant by making many more wavelengths available on each fiber.

Although the concepts for WDM started being explored in the laboratory more than two decades ago, cost-effective WDM systems were commercialized after the creation and perfection of various photonic devices and circuits used to combine, distribute, isolate and amplify optical signals at different wavelengths. Figure 1.1 shows the implementation of those photonic devices in a point-to-point WDM system. Current photonic devices and circuits may be entirely adequate for many of today's point-to-point applications, but they fall short of what is required

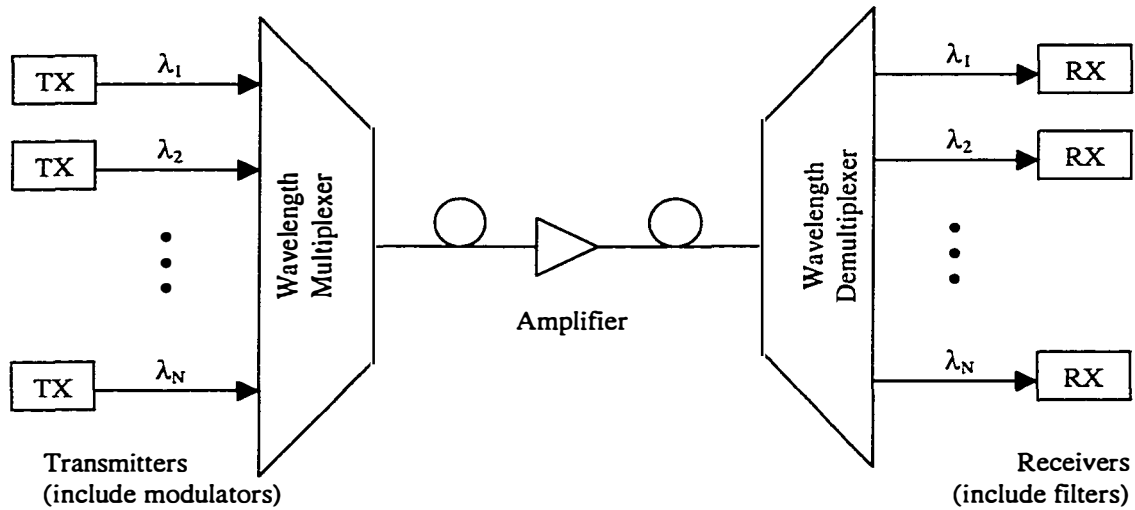


Figure 1.1. Implementation of a typical point-to-point WDM link.

for practical implementation of the future networking techniques as optical networking grows in sophistication and complexity. After point-to-point WDM links have been successfully deployed worldwide, future growth of optical

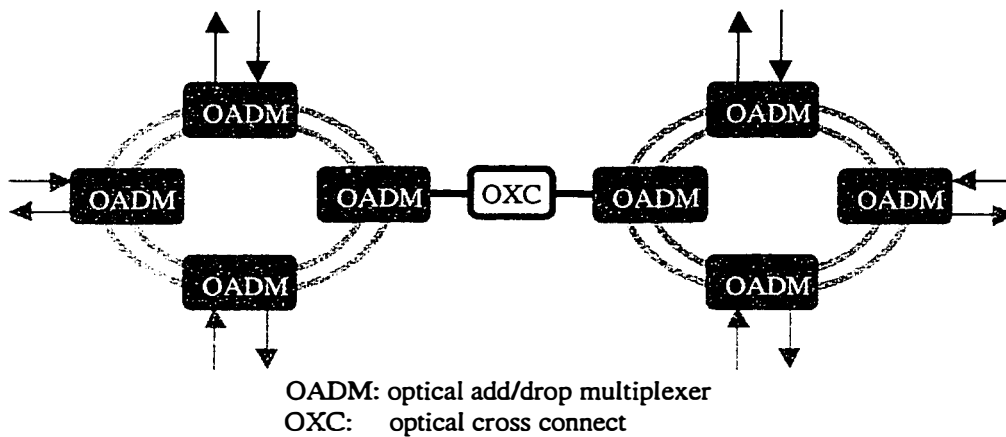


Figure 1.2. Optical transport networking

networks requires new photonic components and circuits, such as optical add/drop multiplexers (OADM) and optical cross connects (OXC), to select and route

individual wavelengths. The ability of these WDM nodal elements allows optical channels to be manipulated in WDM networks and enables new optical transport networks (also called all-optical networks, Figure 1.2). An all-optical network implies that the service providers will have optical access to traffic at various nodes in the networks, just as they have electrical access to today's networks. To make all nodes optical, which will solve the limitation of slow electrical circuits, photonic devices and circuits must be more sophisticated and cost-effective. In current WDM experiments carried out in the research laboratory, fiber optically interconnected photonic devices, such as lasers, waveguide modulators, tunable filters, optical amplifiers, isolators, couplers, attenuators, and detectors, are arranged on an optical table. Even if the combination of all individual photonic devices can meet the system requirements, a major problem here is that making the fiber connections to the various photonic devices used in these experiments is a laborious and costly process, and the coupling loss is often too large. This situation is often tolerable in point-to-point WDM links when only one or a few fiber connections are needed. However, when each node in the future optical transport networks must be optically accessible, such connections will become requirements and the cost will be unacceptable. One solution for this problem is photonic integrated circuits (PICs). PICs refer to the integration of optically interconnected guided-wave devices. By replacing the separate, sequential alignment of fiber interconnections between the discrete devices with single-crystal optical waveguides, PIC technology would not only yield substantial savings, but would also improve system robustness and produce more functional components to meet specific new requirements imposed by the coming and the future WDM networks.

1.2 Comparison of Electronic IC and Photonic IC

PICs have held the promise that the success of electronic integrated circuits could be transferred to the realm of optics. Unfortunately, so far, this promise has fallen short of expectations. Electronic integrated circuits (EICs) began with the invention of transistors in 1947, and the idea of electronic integrated circuits was patented in 1959. After the first microprocessor was reported in 1971, the widescale deployment of the microprocessor in PC's began during the 1980's. The development of PICs began with the invention of semiconductor lasers in 1962. The concept of integrated optics was introduced in 1969 [5]. The first OEIC (opto-electronic integrated circuits) was reported in 1978 [6] and complex PICs have been reported from 1990 [7] onwards. Compared to today's EICs, which contain millions of transistors on a single silicon chip, the state-of-the-art for semiconductor PICs has been limited to a handful of devices.

Two factors are hampering the break-through of PICs. The first is the lack of a large-scale market justifying the investments in developing complex PICs in the last decade. But this situation has now changed with the introduction of all optical networks. The second is the technical limitation to integrate the large variety of photonic devices on one chip, which comes from the nature of photons and will be the main challenge for PICs.

It is believed that the competitive edge of PICs comes from increased scale of integration plus the corresponding cost reduction, which is in fact based on an implicit analogy between photonic and electronic ICs. This analogy, however, has to be treated with care. Although signals in both EICs and PICs are carried by electromagnetic waves, there are fundamental differences between them. In this section, we want to identify the physical and technical reasons, which have limited the development of PICs.

The complexity of both electronic and photonic ICs comes from a combination of pushing the performance of individual components and increasing

the complexity of their interconnections. However, there are big differences

		EIC	PIC
Components	Basic Element	simple and similar	many and complicated
	Dimension	$\mu\text{m}\times\mu\text{m}$	$100\mu\text{m}\times 100\mu\text{m}$ to $\text{cm}\times\text{cm}$
	Scale	millions	handful
	Substrate	one (Si)	\geq one (InP, GaAs, Si etc)
Interconnections	Connect of cells	wires	waveguides
	3D Multilayer vertical interconnect	7 layers	none (strongly needed)
	Enabling technology	thin film technology flip-chip bonding	Not available (wafer bonding ?)

Table 1.1. The comparison between EICs and PICs

between electronic and photonic components and their interconnections. Table 1.1 is the comparison between EICs and PICs. In electronic ICs, there are only a few basic components (transistors, resistors, for example) and they have the similar structures formed on a common host: a silicon substrate. The initial material choices (silicon substrates, silicon dioxide gates and intermediate dielectrics, aluminum interconnections) and processes such as planar technology and photolithography have stood the test of 40 years in EICs. The development of individual components is mainly reflected by decreasing transistor size, which not only reduce costs, but also improve performance in terms of speed, functionality and power dissipation [8]. Modern transistors have dimensions of only a few microns and the gate length is only submicron. In contrast, there are many types of photonic components with totally different structures (lasers, detectors, modulators, couplers, routers and etc.) in PICs. For optimization of the

performance of different photonic devices, generally several different substrates (such as InP for lasers and detectors, Si for routers and pigtail coupling, LiNbO₃ for modulators) and different active regions are needed. Therefore, each component in a PIC makes some compromise with its neighbors to achieve integration and may not have as sterling a figure of merit as the best discrete device. There are devices which do not play well with others at all, and resist integration entirely (such as optical isolators) for III-V semiconductors. In the last decade, several approaches to those problems in PICs have been considered. One is the universal substrate approach [9] in which only a single compromise structure is grown. The design of this structure is such that perhaps all of the individual device structures depart from optimum to an extent, but an overall functional advantage is gained from their integration. The second approach is to use multiple growth and etch process [10]. This approach allows for separately optimized device structures, but makes waveguide alignment and coupling difficult. The third approach is selective area growth (SAG) [11], which allows the engineer to selectively determine the local bandgap of many devices within a single plane simultaneously and makes the integration of low loss waveguides, modulators, switches, lasers and detectors all in a single optical plane possible. But, even with these complicated processing techniques, a large scale PIC is still beyond our vision. This is mainly because photonic devices have lengths ranging from hundreds of microns to several centimeters, which limits the number of photonic components that can be cascaded on a single chip to only a few. The further shrinkage of the physical dimension of current photonic devices will depend on new concepts.

We have seen that the laws of physics and the sciences of materials and devices are becoming increasingly less friendly as we approach the photonic regime. This will be seen more obviously when we compare the interconnections between EICs and PICs. In EICs, millions of electronic components are electrically interconnected with wires. As the EICs' complexity increased, the concept of true three-dimensional (3D) multiple layers of interconnection (see Figure 1.3) were developed in 1980's, and the size of EICs (microprocessors) has



Figure 1.3. 3D multilayer vertically interconnection in EIC

been reduced dramatically and the speed has been dramatically increased. With multichip module (MCM) technology, the performance of EICs is further advanced. But this development has not occurred in photonics. Conventional photonic ICs rely upon a single plane of interconnections (Figure 1.4). The main reason is that optical interconnections via optical waveguides have more stringent requirements and tolerances than electrical interconnections. In electrical interconnections, the electrical signals can be easily routed by higher conductivity Al or Cu wires and the use of dielectrics with a sufficiently small k is enough to isolate the possible crosstalk between wires and layers. Because of the strong confinement of electromagnetic waves in EICs, the vertical interconnection for 3D EICs is not a problem. The electrical currents in wires can be arbitrarily

directed to different positions and layers without suffering a high loss. The

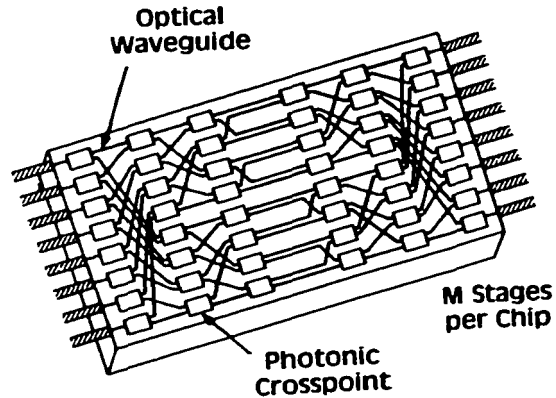


Figure 1.4. 2D photonic IC. Interconnections only happen on a single plane.

enabling technologies for vertical interconnection in EICs are still the conventional planar technique and flip-chip bonding for MCMs. The current number of vertically interconnected layers is 7 and it will likely increase to 9 in 2012. The situation is totally different for PICs when the signals propagate along an optical waveguide. In optical waveguides, the confinement of optical waves is relatively weak due to the finite index contrast (the smallest index is 1 for air) and the requirement of the single mode operation, which forbids optical waveguide bends with a small curvature. Otherwise, bending waveguides will suffer from an unacceptable optical loss. Therefore, to change the propagation direction of optical signals via waveguides in PICs, a large space to bend the waveguides is needed, which limits the integration density of two-dimensional PICs. Another factor to limit the complexity of PICs is that the routing of a large number of waveguides in two-dimensions inevitably involves a large number of waveguide crossings, which would increase the crosstalk and excess loss. The same problem happened in EICs and was solved by 3D vertical interconnection technology. Similar to EICs, the addition of a third dimension to photonic ICs will overcome some of the inherent problems in 2D PICs and increase the complexity of PICs

greatly. However, conventional thin film planar technologies are not suitable to vertically interconnect multiple layers in 3D PICs. In semiconductor PICs, different layers have to be crystalline, and non-planar crystalline deposition of low loss waveguides after patterning is difficult with epitaxy and impossible by sputtering or evaporation (as is done in EICs). The vertical bending (Figure 1.5)

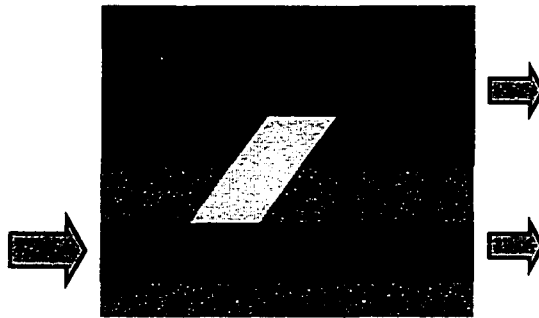


Figure 1.5. Different layers are connected by a slope waveguide.

of optical waveguides further complicate the process of PICs. Polymers [12] may be a choice for this purpose, but the functions of such PICs are limited without the optical properties of semiconductors.

1.3 3D multilevel photonic devices and circuits

As we mentioned before, the nature of photonics makes the shrinkage of photonic devices difficult. It means that the advance of future PICs will mainly depend on increasing of the complexity of optical interconnections. The major breakthrough for PICs can be expected when technology is ready for 3D multilevel photonic devices and circuits with an increased functionality due to large-scale integration.

This dissertation describes the design and fabrication of several novel 3D multilevel photonic devices and circuits. The fabrication of 3D waveguide devices is based on a new technique, called wafer bonding or wafer fusion [13, 14], which was initially developed for integrating two dissimilar materials and surmounting the lattice mismatch in III-V semiconductors. Since wafer bonding can combine two patterned wafers together and enables processing both sides of epi-films, it provides us a viable method to stack planar processed circuits vertically to form novel 3D devices and circuits. An example is shown in Figure 1.6. Two arrays of waveguides on two different substrates are bonded to form a 3D 4×4 optical

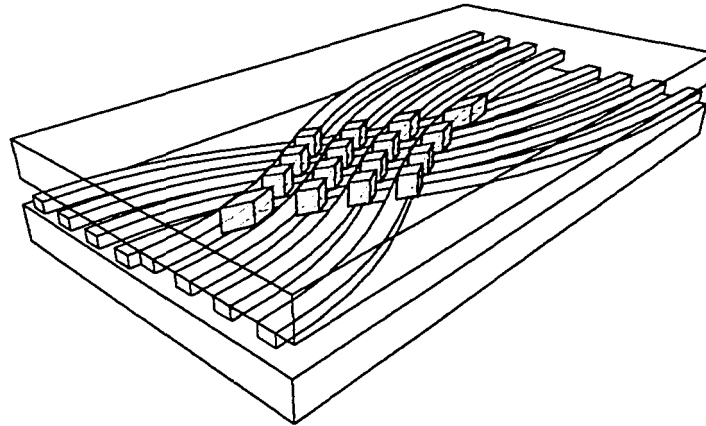


Figure 1.6. Proposed 4×4 crossbar switch array based on vertical coupling between two substrates by wafer fusion.

switch. In this device, the vertical optical interconnection is provided by vertical coupling at the crossing points between different array layers and the air gap is the best isolation layer between top and bottom waveguides (see Figure 1.7). Inter- and intra-chips photonic interconnections can be realized based on this idea.

It is worth noting that 3D optical interconnect technologies may be a solution for future high-bandwidth inputs and outputs (I/O) to very-large-scale integrated circuits (VLSI) [15]. Therefore, the development of 3D multilevel

photonic and optoelectronic interconnects may be driven by both the photonic and electronic industries.

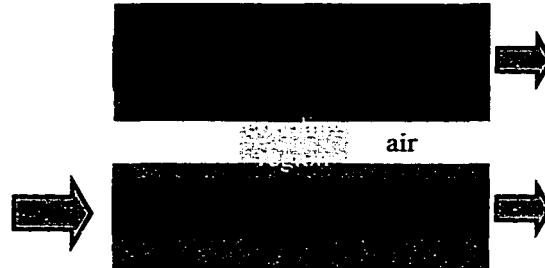


Figure 1.7. Vertical coupling between two layers.

3D multilevel photonic devices and circuits are in their infancy. The final success will depend on new enabling technologies and device concepts. It is not only a big challenge for researchers in the field of optoelectronics, but also provides the researchers more freedom to fabricate novel photonic devices and circuits, as we will see in this dissertation.

This dissertation will begin with a brief review of the history and application of wafer bonding in Chapter 2. The waveguide loss introduced by wafer fused interfaces will be investigated at the same time. Chapter 3 will give several useful techniques for the design and optimization of optical waveguide devices, including transfer matrix method, effective index method, coupled mode theory, normal mode theory and beam propagation method. The extinction ratio of couplers with very short coupling lengths will be emphasized. In Chapter 4, 5 and 6, the design and fabrication of several 3D multilevel photonic devices and circuits will be described. Wafer fused vertical couplers with very short coupling lengths and push-pull switches by the inversion of crystal symmetry will be discussed in Chapter 4. Chapter 5 will introduce wavelength multiplexers by cascading 3D vertical couplers. The design and fabrication of optical add/drop

multiplexers based on X-crossing vertical coupler filters will be described in Chapter 6. Chapter 7 will summarize all of the work in this dissertation.

Reference:

- [1] R. Castelli and T. Krause, "Market trends and evolution for optical transmission systems," *Alcatel Telecommunications Review*, pp. 165-75, 1998.
- [2] G. R. Hill, "Wavelength domain optical network techniques," *Proceedings of the IEEE*, vol. 78, pp. 121-32, 1990.
- [3] T. Miki, "Optical transport networks," *Proceedings of the IEEE*, vol. 81, pp. 1594-609, 1993.
- [4] M. J. O'Mahony, "Optical multiplexing in fiber networks: progress in WDM and OTDM," *IEEE Communications Magazine*, vol. 33, pp. 82-8, 1995.
- [5] S. E. Miller, "Integrated optics: An introduction," *Bell System Technical Journal*, vol. 48, pp. 2059-69, 1969.
- [6] C. P. Lee, S. Margalit, I. Ury, and A. Yariv, "Integration of an injection laser with a Gunn oscillator on a semi-insulating GaAs substrate," *Applied Physics Letters*, vol. 32, pp. 806-7, 1978.
- [7] T. L. Koch, F. S. Choa, U. Koren, R. P. Gnall, F. Hernandez-Gil, C. A. Burrus, M. G. Young, M. Oron, and B. I. Miller, "Balanced operation of a GaInAs/GaInAsP multiple-quantum-well integrated heterodyne receiver," *IEEE Photonics Technology Letters*, vol. 2, pp. 577-80, 1990.
- [8] "The National Technology Roadmap for Semiconductors," Semiconductor Industry Association November 1997.
- [9] A. C. Crook, M. L. Osowski, G. M. Smith, J. Frame, M. Grupen, and T. A. DeTemple, "A universal optical heterostructure for photonic integrated circuits: a case study in the AlGaAs material system," *IEEE Journal of Selected Topics in Quantum Electronics*, vol. 2, pp. 341-7, 1996.

- [10] T. L. Koch and U. Koren, "Semiconductor photonic integrated circuits," *IEEE Journal of Quantum Electronics*, vol. 27, pp. 641-53, 1991.
- [11] M. Suzuki, M. Aoki, T. Tsuchiya, and T. Taniwatari, "1.24-1.66 μm quantum energy tuning for simultaneously grown InGaAs/InP quantum wells by selective-area metalorganic vapor phase epitaxy," *Journal of Crystal Growth*, vol. 145, pp. 249-55, 1994.
- [12] S. M. Garner, L. Sang-Shin, V. Chuyanov, A. Chen, A. Yacoubian, W. H. Steier, and L. R. Dalton, "Three-dimensional integrated optics using polymers," *IEEE Journal of Quantum Electronics*, vol. 35, pp. 1146-55, 1999.
- [13] Z. L. Liao and D. E. Mull, "Wafer fusion: a novel technique for optoelectronic device fabrication and monolithic integration," *Appl. Phys. Lett.*, vol. 56, pp. 737-9, 1990.
- [14] Y. H. Lo, R. Bhat, D. M. Hwang, M. A. Koza, and T. P. Lee, "Bonding by atomic rearrangement of InP/InGaAsP 1.5 μm wavelength lasers on GaAs substrates," *Appl. Phys. Lett.*, vol. 58, pp. 1961-3, 1991.
- [15] A. V. Krishnamoorthy and D. A. B. Miller, "Scaling optoelectronic-VLSI circuits into the 21st century: a technology roadmap," *IEEE Journal of Selected Topics in Quantum Electronics*, vol. 2, pp. 55-76, 1996.

Chapter 2

Wafer Bonding

Wafer bonding or wafer fusion is a versatile technique of jointing similar or different materials together without considering their crystallographic orientation, structure, and lattice mismatch and without any adhesives. This technique has been developed and used for the fabrication of long wavelength vertical cavity surface emitting lasers (VCSELs) at UCSB since 1992. This chapter will review the history and some applications of the wafer bonding technique in Section 2.1 and 2.2. In Section 2.3, a brief description of the bonding process will be given. More attention will be focused on the investigation of the optical propagation loss introduced by wafer bonding in fused optical waveguides in section 2.4.

2.1 History of wafer bonding

It has been well known for more than two hundred years that flat pieces of glass mirror polished to optical quality and smooth metal surfaces, if atomically clean, can stick to each other. The first systematic investigation on the room temperature adherence of pieces of silica was reported by Lord Rayleigh in 1936 [1]. Many phenomena he observed and investigated have been rediscovered and conformed by researchers in the last decade. In the early 1960s, Nakamura *et al.* [2] found that an oxidized silicon could be bonded on a normal silicon chip without any adhesives. Kenny [3] succeeded in the bonding assisted by 2000 psi hydrostatic pressure and the high temperature annealing of 1225 °C. Later, Wallis and Pomerantz [4] introduced a field-assisted method for bonding of glass to metal, or silicon to quartz. This method, called anodic bonding or field-assisted

bonding, is based on electrostatic forces pulling the two materials together. However, no attention was paid to their work because at that time there was only negligible application for silicon-on-insulator (SOI) materials. In addition, the wafer cleaning and polishing technology was not yet advanced enough to guarantee low contamination interfaces and sufficient surface flatness.

The current interest in wafer bonding (also called wafer fusion, fusion bonding, bonding by atomic rearrangement or direct bonding) originated in the work performed by two different groups in the middle of the 1980s. Lasky [5] from IBM reported room temperature bonding of silicon to silicon dioxide, and silicon dioxide to silicon dioxide followed by a high temperature annealing. Shimbo *et al.* [6] from Toshiba reported the silicon to silicon direct bonding for power devices. Direct wafer bonding of compound semiconductors (GaAs to InP) was first reported by Liao and Mull [7] and Lo *et al.* [8]. Since then, the potential of the wafer bonding technique became widely recognized and different applications of wafer bonding were discovered.

2.2 Applications of wafer bonding

Apart from the scientific studies of semiconductors and semiconductor interfaces, the possible applications are the main impetus to the development of wafer bonding technique. A wide range of applications will be briefly described in this section; more attention will be paid to optoelectronic devices.

A. Silicon-on-Insulator (SOI)

Wafer bonding starts as a specific way to fabricate inexpensive thick ($>1\mu\text{m}$) film SOI materials of high quality. The use of SOI wafers for MOS production is apparent, but bipolar devices on SOI films may also become interesting. The details of SOI applications can be found in several review papers [9] [10].

B. Micromechanics

Wafer bonding has added a new tool to the tool-box of the researchers developing micro-mechanical devices [11]. One of the earliest uses of wafer bonding was in the packaging of pressure sensors. Now it is commercially used for sensor and actuator fabrication. The most significant area of application for wafer bonding is in wafer-level packaging, which makes it possible to realize tremendous overall savings in cost. An important role for wafer bonding in microstructures is in the creation of multi-wafer laminations. This concept is very valuable for photonic integrated circuits as we discussed in the first chapter.

C. Bonding of dissimilar materials

Wafer bonding of different compound semiconductors is of great interest since it suggests a technique for combining the best features of compound semiconductors. Heteroepitaxial growth by means of molecular beam epitaxy (MBE) and metal organic chemical vapor deposition (MOCVD) has been developed to integrate different materials. These attempts have been somewhat successful but the compound semiconductors grown in such processes are generally poorer than films grown on the same substrates because of the constraint of *lattice mismatch*. Wafer bonding promises to become a powerful new tool for combining dissimilar materials without degrading the crystal quality. Since this technology was first introduced to III-V compound semiconductors, many novel and innovative device applications have been demonstrated. In many cases, record performances have been achieved. A few prominent examples are: long wavelength vertical cavity surface emitting lasers (VCSEL) by bonding GaAs/AlAs mirrors to InGaAsP active regions [12] [13]; high brightness LEDs by replacing an absorptive substrate, GaAs, with a transparent substrate, GaP [14]; high gain bandwidth product avalanche photo detectors (APDs) by combining silicon with InGaAs [15] and resonant cavity detectors. One interesting

application of wafer bonding is to form a compliant substrate on which defect-free heteroepitaxial layers with large lattice mismatches to the substrate may be grown [16].

D. Different crystallographic orientation bonding

Besides the advantage of overcoming lattice mismatch, wafer bonding allows the integration of materials with different crystallographic orientations. This is a unique feature of bonding and it cannot be realized by epitaxial growth because the orientation is determined by the substrate. This concept has been applied to obtain structures by stacking GaAs layers, whose crystallographic orientations could be changed periodically, and produce a quasi-phase-matching effect for second harmonic generation [17] [18]. A push-pull operation switch was demonstrated recently by bonding two waveguides with different crystal orientations [19]. The details of the latter device will be discussed in Chapter 4.

E. Three-dimensional structures

Wafer bonding enables processing of the wafers prior to bonding, which is a way of fabricating novel device geometries. An example of applications is three-dimensional circuits, especially 3D photonic integrated circuits. This is one main goal of this dissertation, as we discussed in Chapter 1. Noda *et al.* [20] successfully demonstrated a 3D photonic crystal by multiple bonding of several layers of GaAs stripes using wafer bonding. In this dissertation, we will demonstrate a few novel 3D optical waveguide devices based on this idea.

2.3 Wafer bonding process

Although there may be some specifics in different bonding experiments, three basic steps are always needed in any wafer bonding process: surface cleaning, contacting, and annealing. In this section, the main procedure for wafer

bonding at UCSB will be described and the more details can be found in Babic's [21] and Margalit's [22] Ph. D. dissertations.

Prebonding wafer surface cleaning is critical to the bonding quality and the uniformity of the bonded films. In general, the process of cleaning consists of solvent cleaning, oxidation and oxide removal. The solvent cleaning includes several immersions in boiling acetone, isopropanol rinsing and nitrogen drying. Then the wafers are descummed with oxygen plasma for 10 minutes at 100W power. Concentrated ammonium hydroxide is used to remove the oxide. Subsequently, the samples are exposed to about 1 hour of ultraviolet-ozone for the second oxidation. Wafers are then placed in concentrated NH_4OH and transported to the bonding furnace. For 3D waveguide structures, because the wafers have gone through several lithographic processes and dry/wet etchings with a silicon nitride mask before bonding, a more careful surface cleaning is needed. Before the routine bonding cleaning, a gentle rubbing with Q-tips soaked with acetone and isopropanol is used to clean both surfaces of each wafer, and then the samples are placed in buffered-HF for 10 minutes to remove the possible residual SiN. It also helps to remove the oxide on InP surface.

The contacting of two samples to be bonded is performed in a methanol solution: It is called wet bonding. One wafer is flipped on the top of another and they are pressed together. After two wafers are weakly bonded in solution by a slight pressure, they are taken out of solution and placed in the graphite bonding fixture. This method can prevent the reoxidation of the surfaces.

The annealing furnace at UCSB is a modified Liquid Phase Epitaxy (LPE) setup. The quartz tube is evacuated to a pressure of about 10 mTorr after inserting the bonding fixture and then filled to atmospheric pressure with hydrogen. The annealing temperature is about 630°C and kept there for about 30 minutes. This is the general bonding condition that we used for the fabrication of waveguide devices.

2.4 Optical loss at bonded interface

The topic of this dissertation is the application of wafer bonding to the fabrication of novel optical waveguide devices. As we mentioned before, most of the previous applications of wafer bonding to III-V semiconductors are for active devices. But for monolithic integration, passive elements such as couplers and filters must be incorporated to realize high performance photonic integrated circuits. Optical waveguides with a small propagation loss are the core of most of passive devices. Although the mechanical, electrical and optical properties of the bonded interfaces have been extensively studied and the bonded interfaces were believed to be electrically conductive and optically transparent, there have been no reports on optical loss introduced by bonding interface. To get an estimate of bonded interface optical loss, we placed the bonded junction in an optical waveguide; the optical propagation loss of bonded and unbonded waveguides will be compared in this section.

2.4.1 Wafer bonded waveguide fabrication

The single mode waveguide structure is shown in Figure 2.1. It was grown by MOCVD with a 0.5 μm InGaAsP ($\lambda_{\text{gap}}=1.3 \mu\text{m}$) guiding layer, a 0.24 μm InP cladding layer which includes two 0.1 μm InP layers and two 0.02 μm InGaAsP etching stop layers ($\lambda_{\text{gap}}=1.15 \mu\text{m}$), and finally a 0.6 μm InP ridge layer. For the purpose of comparison, we used the same wafer and single mode waveguide geometry with and without a bonded interface near the core region. Two bonded waveguide structures are fabricated in this experiment. To fabricate structure A, two $1 \times 0.8 \text{ cm}^2$ samples are cut from the MOCVD grown wafer. In one of the sample, the 0.6 μm InP ridge layer and 0.1 μm cladding layer with two etch stop layers are removed using selective wet etching (Fig. 2.1(a)). 10 μm wide, 0.6 μm deep channels with 160 μm spacing are opened in another sample. The two

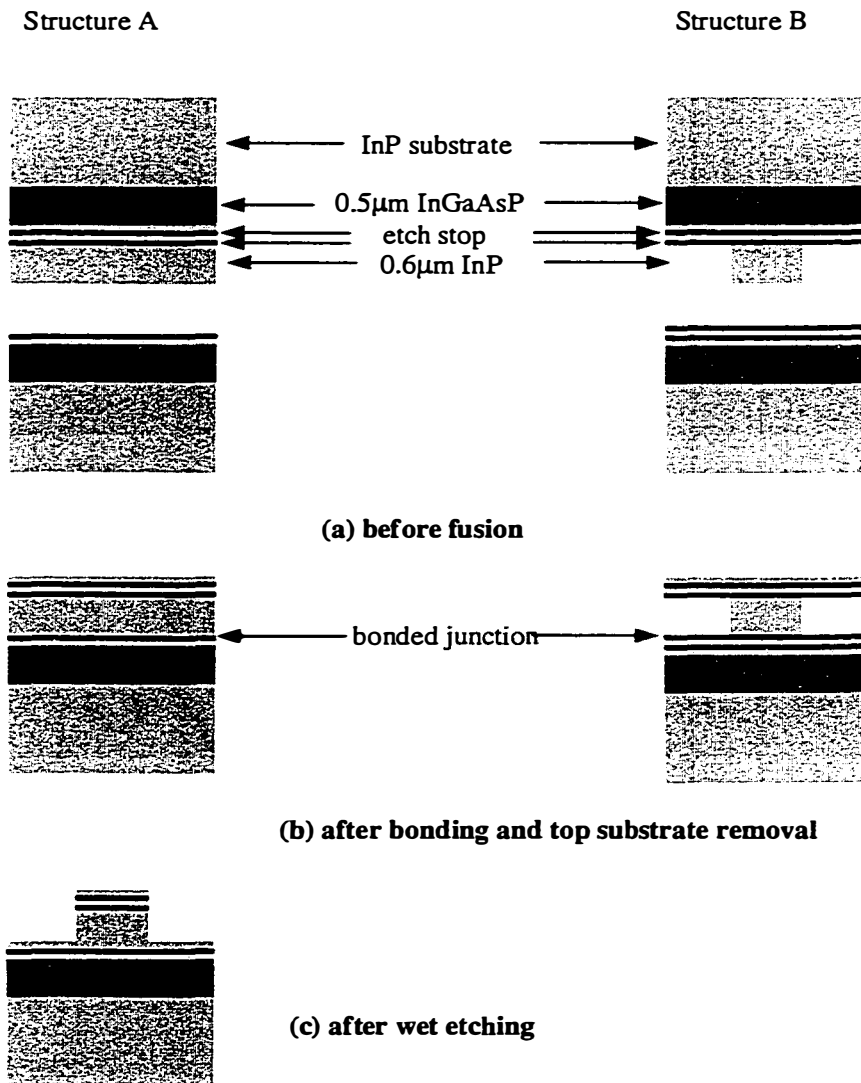
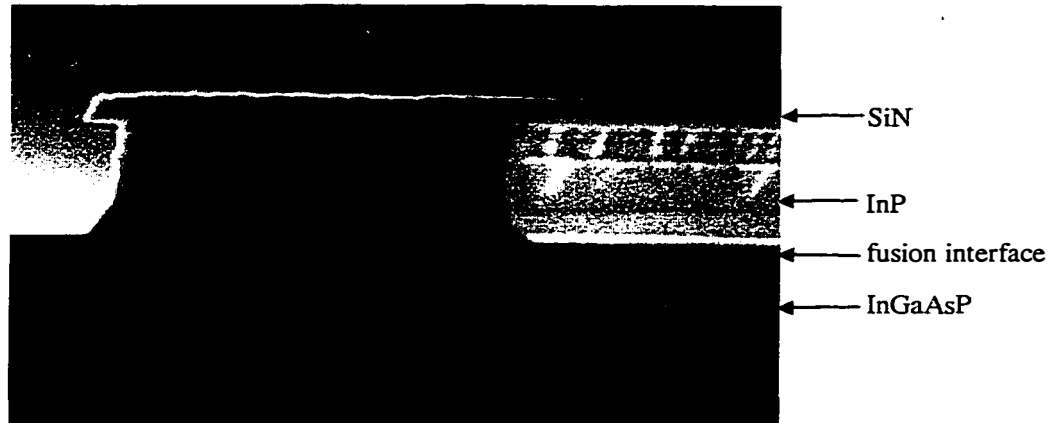
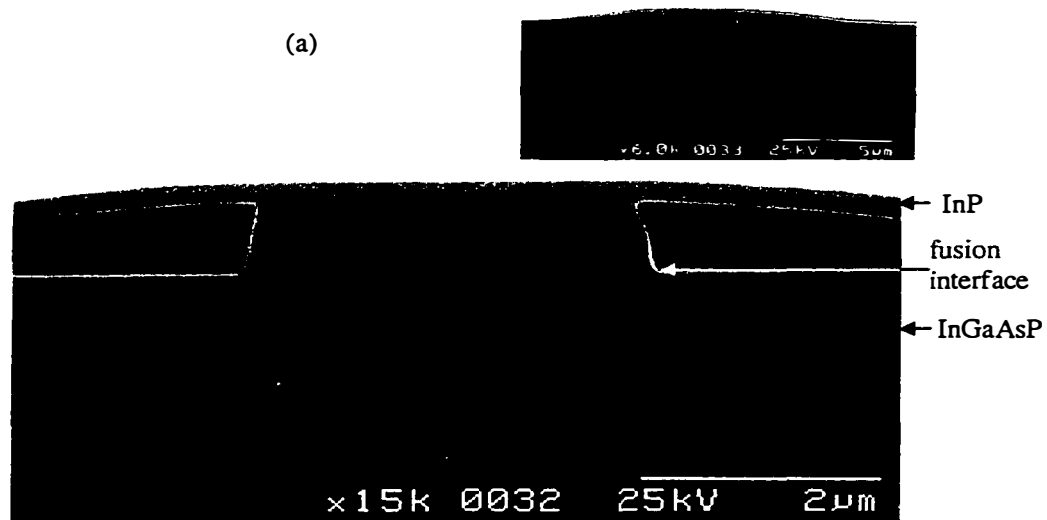


Figure 2.1. The fabrication steps for bonded waveguides

samples are then bonded at 630 °C for 30 minutes. Subsequently, the InP substrate and 0.5 μm InGaAsP guiding layer of the top sample are removed (Figure 2.1(b)). Finally, 3 μm wide ridge waveguides are formed using wet etching (2:1 HCl:DI



(a)



(b)

Figure 2.2 The stain-etched SEM pictures of structure A and B. In structure B, after removing the top substrate and InGaAsP guiding layer, $0.2\mu\text{m}$ InP is left above the ridge. This is because the etching will attack the waveguide slab layer. A large scale picture is also shown.

water) (Fig. 2.1(c)). Different from structure A, only the $0.6\mu\text{m}$ InP ridge layer of one sample is removed and the $3\mu\text{m}$ wide ridges with $125\mu\text{m}$ spacing have been fabricated on another sample before bonding in structure B. Thus after the substrate and the $0.5\mu\text{m}$ guiding layer of the top wafer are removed, the single

mode waveguides are formed. Compared to A, the bonding area of structure B is very small. All waveguides are along the [011] direction and the processing of all waveguides including the unbonded ones are same. The lengths of waveguides are around 6mm.

2.4.2 Optical loss

Figure 2.2(a) and (b) show two stain-etched SEM pictures of finished waveguides of structures A and B. To avoid etching the slab InP layer, the top 0.2 μm InP layer of structure B is left above the ridge. The bonded interfaces cannot be seen in both pictures. This is an indication of the high quality of the bonded interface. The Fabry-Perot resonance technique (see Appendix A) was used to measure the optical propagation loss. The optical loss of an unbonded waveguide is about 2.4 dB/cm. The loss of structure A is 3.5 dB/cm and the loss of structure B is 5.6 dB/cm at 1.55 μm . Since the geometry and materials are identical, the 1.1 dB/cm excess loss in structure A should be attributed to the bonding interface.

The theoretical analysis indicates that the field strength at the bonding interface of structure A is 49% of the maximum field; for structure B it is 35%. If the excess loss is only introduced by the bonded interface, structure B should have less loss than A. One reason of the higher loss of B is that the top 0.2 μm InP layer is so thin that it is broken randomly along the waveguides after the removal of the substrate, which introduces a high scattering loss. This can be overcome by changing the device design. Another reason is the very high pressure during bonding for structure B. In structure A, after fabrication of narrow channels on one of the samples prior to bonding, typically over 90% of the surface of the samples is in contact during the bonding process. In structure B where the bonding was only over the surface on the top of waveguides, only 4% of the surface of the two wafers is in contact during bonding. There is one order of

magnitude pressure difference between structure A and B during bonding. A large pressure may introduce more defects at the bonding interface.

The main mechanism that causes optical loss at bonded interface is still not clear. The possible reasons are non-uniform bonding interface and free carrier absorption. We checked the bonded interface using SEM. There are no visible microscopic voids in most areas of the bonded In(GaAs)P/In(GaAs)P junction, which indicates a good uniformity of the bonding junction, and that the optical scattering loss caused by non-uniformity of bonding interface is negligible. The excess loss may be caused mainly by free carrier absorption. This is because the bonded interface is a defect-rich region and the bonding procedure introduces many residual impurities at the junction. Second Ion Mass Spectroscopy (SIMS) measurements confirmed that very high levels of oxygen exist at the InP/GaAs bonded junction [22]. As a result of crystallographic defects and impurities, charge trapping centers are present. Charge trapping, recombination and generation processes are expected to cause carrier absorption. More investigations are needed to understand the details of the bonded interface excess loss.

Compared with structure A, structure B will be more attractive, since it provides an extra degree of freedom to realize new functional devices (see Chapters 5 and 6). Three-dimensional devices can be realized easily by patterned or structured bonding.

2.4.3 Uniformity

The issue of the bonded area uniformity for large scale monolithic integration is very important. The size of our bonded wafers is about 1 cm×0.8 cm. After thinning and cleaving, the size of sample for measurement is about 6 mm×6 mm. The yield of the bonded waveguides is more than 90%, which is almost the same as un-bonded sample. Channels in structure A provide 150 μm wide multimode waveguides. We didn't observe any "dark" spot in these

multimode waveguides under different exciting positions. This also indicates that the bonding material has a good uniformity.

The most important problem for the uniformity of wafer bonding is the presence of "voids" or "bubbles" at the bonding interface, where the bonding has failed. It is widely believed that both the macroscopic surface flatness and the microscopic surface roughness are crucial for a successful uniform bonding. Commercially available well-polished Silicon, GaAs, InP wafers, having a flatness variation of several μm and a micro roughness of several \AA , are generally good enough to realize uniform bonding. However, after several processing steps, the surface roughness will be worse. Despite this fact, thanks to the mass transport effect under high pressure and high temperature [7], a uniform bonding is still possible, especially for In(GaAs)P/In(GaAs)P systems.

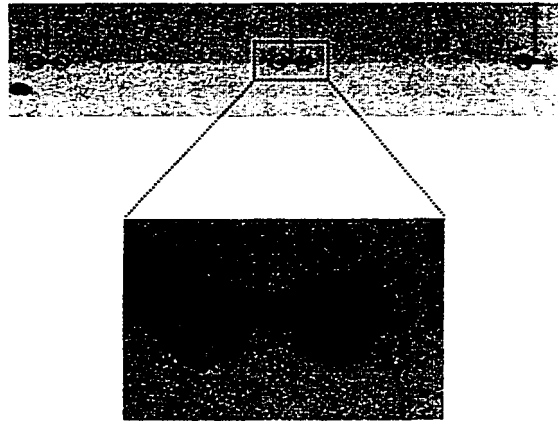


Figure 2.3 The microscopic pictures of InP/GaAs cleaved channels.
The top one: 200 \times magnification; The bottom one: 1000 \times magnification.
Some liquid is diffusing out of channels.

Since there are always some water, oxygen or hydrocarbons adsorbed at the wafer surface, the desorption of those liquids/gases trapped at the interface at an elevated temperature forms voids; or even large bubbles. This is the main problem in III-V material bonding. To solve this problem, channels are etched in

one of wafers prior to bonding [21]. This phenomenon was observed a long time ago; Lord Rayleigh in 1936 noticed that scratches with ridges are detrimental to bonding whereas some scratches without ridges can be bonded easily. In 1991

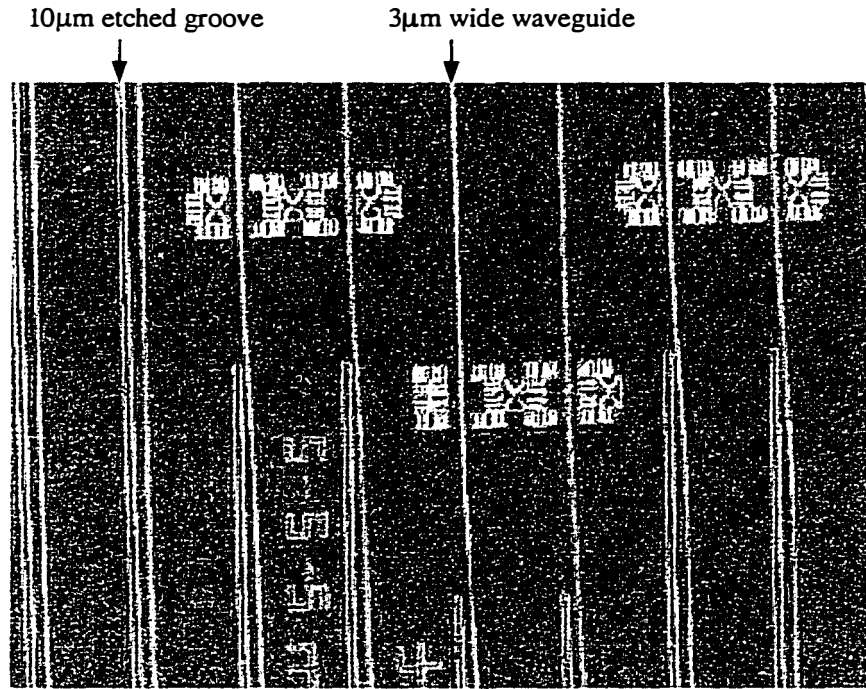


Figure 2.4 Uniform wafer fusion. The spacing between two waveguides is $125\mu\text{m}$. This sample has gone through 4 steps of SiN depositions, photolithographs, dry and wet etches (two before fusion and two after fusion)

special grooves etched in the surface of one wafer were shown to exhibit no void formation and ensure a very high yield [23]. This demonstrates that the intrinsic voids are caused by gases trapped at the interface. The function of those channels is believed to provide an outlet for liquids/gases desorption during annealing. Figure 2.3 shows a microscopic picture of cleaved channels. The composition of the liquid that actually flows out of the channels is not known. Detailed investigation of the composition of the liquid is needed to better understand the functions of the channels. All of the bonding done in this dissertation is on

patterned substrates, *i.e.*, a certain structure is etched in one of the wafers prior to bonding. Thus, no intentional channels are used. One interesting observation is that a large area ($1.2 \times 1.6 \text{ cm}^2$) uniform bonding can always be realized even if all channels don't go through the whole wafer. Figure 2.4 shows a microscopic picture of wafer-bonded wavelength multiplexers (see Chapter 5). This sample has gone through four steps of SiN depositions, photolithographs and dry/wet etches (two before bonding and two after bonding). As we can see from this picture, there are no microscopically visible defects in the surface.

2.5 Summary

In this chapter, the history and the main applications of wafer bonding technology have been reviewed. The optical propagation loss introduced by the bonded layer was investigated. An excess loss of 1.1dB/cm at $1.55\mu\text{m}$ has been measured for waveguides, which incorporate a bonded junction near the core region. Since wafer bonding technique opens a new degree of freedom for combining materials and for fabrication of novel devices, there is no doubt that it will play an increasing important role in a wide field. Although a great deal of progress has been made to advance the wafer bonding technique as a viable production process, numerous questions are still remaining regarding the physics and the enabling technologies of bonding. For the fabrication of three-dimensional circuits, one key challenge is high precision (submicron) alignment during the bonding process. To realize the potential of wafer bonding, continued progress is needed to develop more reliable and flexible bonding equipment.

References

- [1] L. Rayleigh, *Proc. Phys. Soc. A*, vol. 156, pp. 326, 1936.
- [2] T. Nakamura, "Patent 3.228.656," . U.S., 1966.
- [3] D. M. Kenny, "Patent 3.332.137," . U.S., 1967.
- [4] G. Wallis and D. I. Pomerantz, "Field assisted glass-metal sealing," *Journal of Applied Physics*, vol. 40, pp. 3946-9, 1969.
- [5] J. B. Lasky, "Wafer bonding for silicon-on-insulator technologies," *Appl. Phys. Lett.*, vol. 48, pp. 78-80, 1986.
- [6] M. Shimbo, K. Furukawa, K. Fukuda, and K. Tanzawa, "Silicon-to-silicon direct bonding method," *Journal of Applied Physics*, vol. 60, pp. 2987-9, 1986.
- [7] Z. L. Liao and D. E. Mull, "Wafer fusion: a novel technique for optoelectronic device fabrication and monolithic integration," *Appl. Phys. Lett.*, vol. 56, pp. 737-9, 1990.
- [8] Y. H. Lo, R. Bhat, D. M. Hwang, M. A. Koza, and T. P. Lee, "Bonding by atomic rearrangement of InP/InGaAsP 1.5 μ m wavelength lasers on GaAs substrates," *Appl. Phys. Lett.*, vol. 58, pp. 1961-3, 1991.
- [9] K. Mitani, U. M. Gosele, "Wafer bonding technology for silicon-on-insulator applications: a review," *Journal of Electronic Materials*, vol. 21, pp. 669-76, 1992.
- [10] S. Bengtsson, "Semiconductor wafer bonding: a review of interfacial properties and applications," *Journal of Electronic Materials*, vol. 21, pp. 841-62, 1992.
- [11] M. A. Schmidt, "Wafer-to-wafer bonding for microstructure formation," *Proceedings of the IEEE*, vol. 86, pp. 1575-85, 1998.

- [12] N. M. Margalit, D. I. Babic, K. Streubel, R. P. Mirin, D. E. Mars, J. E. Bowers, and E. L. Hu, "Laterally oxidized long wavelength cw vertical-cavity lasers," *Applied Physics Letters*, vol. 69, pp. 471-2, 1996.
- [13] Y. Qian, Z. H. Zhu, Y. H. Lo, H. Q. Hou, M. C. Wang, and W. Lin, "1.3- μ m Vertical-cavity surface-emitting lasers with double-bonded GaAs-AlAs Bragg mirrors," *IEEE Photonics Technology Letters*, vol. 9, pp. 8-10, 1997.
- [14] F. A. Kish, F. M. Steranka, D. C. DeFevre, D. A. Vanderwater, K. G. Park, C. P. Kuo, T. D. Osentowski, M. J. Peanasky, J. G. Yu, R. M. Fletcher, D. A. Steigerwald, M. G. Craford, and V. M. Robbins, *Very high-efficiency semiconductor wafer-bonded transparent-substrate (Al/sub x /Ga/sub $1-x$)/sub 0.5/In/sub 0.5/P/GaP light-emitting diodes*.
- [15] A. R. Hawkins, W. Weishu, P. Abraham, K. Streubel, and J. E. Bowers, "High gain-bandwidth-product silicon heterointerface photodetector," *Applied Physics Letters*, vol. 70, pp. 303-5, 1997.
- [16] F. E. Ejeckam, Y. H. Lo, S. Subramanian, H. Q. Hou, and B. E. Hammons, "Lattice engineered compliant substrate for defect-free heteroepitaxial growth," *Applied Physics Letters*, vol. 70, pp. 1685-7, 1997.
- [17] L. Gordon, G. L. Woods, R. C. Eckardt, R. R. Route, R. S. Feigelson, M. M. Fejer, and R. Byer, "Diffusion-bonded stacked GaAs for quasiphasematched second-harmonic generation of a carbon dioxide laser," *Electron. Lett.*, vol. 29, pp. 1942-4, 1993.
- [18] S. J. B. Yoo, R. Bhat, C. Caneau, and M. A. Koza, "Quasi-phase-matched second-harmonic generation in AlGaAs waveguides with periodic domain inversion achieved by wafer-bonding," *Applied Physics Letters*, vol. 66, pp. 3410-12, 1995.

- [19] B. Liu, A. Shakouri, P. Abraham, and J. E. Bowers, "Push-pull fused vertical coupler switch," *IEEE Photonics Technology Letters*, vol. 11, pp. 662-4, 1999.
- [20] S. Noda, N. Yamamoto, and A. Sasaki, "New realization method for three-dimensional photonic crystal in optical wavelength region," *Japanese Journal of Applied Physics, Part 2 (Letters)*, vol. 35, pp. L909-12, 1996.
- [21] D. I. Babic, "Double-fused long-wavelength vertical-cavity lasers," in *ECE Department*. Santa Barbara: University of California, 1995.
- [22] N. Margalit, "High-temperature long-wavelength vertical-cavity lasers," in *ECE Department*. Santa Barbara: University of California, 1998.
- [23] W. Kissinger, G. Kissinger, J. Kruger, and H. Hofmann, "High yield in wafer bonding with surface structured wafers," *Materials Letters*, pp. 266-9, 1991.

Chapter 3

Design of Waveguide Devices

3.1 Introduction

Optical waveguides are the "wires" used to transmit and route optical signals (photons), which provide the basis for numerous integrated optic devices for the applications of lightwave telecommunications, optical signal processing and more. Effective and simple theoretical calculation techniques are needed for the design and optimization of waveguide devices. In this chapter, we will briefly discuss the design tools for optical waveguide devices. First, the transfer matrix method (TMM) for multilayer slab waveguide calculations will be given in Section 3.2. Then, the effective index method (EIM) for simplifying 3D waveguide problems to two slab waveguides will be described in Section 3.3. Coupled Mode Theory (CMT) and Normal Mode Theory (NMT) for the design of couplers and filters will be described in Section 3.4. Beam Propagation Method (BPM) will be mentioned in Section 3.5. Finally, in Section 3.6, these different methods are used to design vertical couplers. Fabrication of these couplers will be presented in Chapter 4. More examples of vertical coupler devices will be shown in Chapter 5 and 6.

3.2 Transfer Matrix Method (TMM)

The transfer matrix method [1] is a powerful and effective technique to find the propagation constants of modes in a planar waveguide without explicitly deriving an expression for the transcendental characteristic equation. This numerical technique is particularly well suited to design and optimize multilayer

waveguides, where the modes can have a complex propagation constant due to loss or leak mechanisms.

We consider a planar multilayer waveguide as shown in Figure 3.1. The general solution of the wave equation in each layer is well known:

$$E_{y,j} = A_j \exp(k_j(x - x_j)) + B_j \exp(-k_j(x - x_j)) \quad (3.1)$$

where $k_j = \sqrt{\beta^2 - k_0^2 n_j^2}$, A_j and B_j are the complex field coefficients, k_0 is the free space wavenumber, $\beta = k_0 n_{\text{eff}}$ is the propagation constant, n_{eff} is the effective index and x_j is the position of layer j . By imposing the continuity of the field and

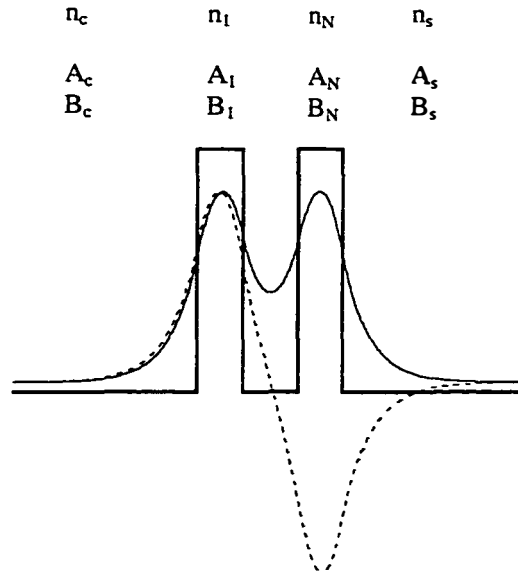


Figure 3.1. Schematic diagram of a multilayer slab waveguide. The field profiles of two modes are also shown (thin lines).

its derivative for each interface, it is easy to find:

$$\begin{bmatrix} A_{j+1} \\ B_{j+1} \end{bmatrix} = T_j \begin{bmatrix} A_j \\ B_j \end{bmatrix}$$

where

$$T_j = \frac{1}{2} \begin{bmatrix} (1 + \zeta_j \frac{k_j}{k_{j+1}}) \exp(k_j d_j) & (1 - \zeta_j \frac{k_j}{k_{j+1}}) \exp(-k_j d_j) \\ (1 - \zeta_j \frac{k_j}{k_{j+1}}) \exp(k_j d_j) & (1 + \zeta_j \frac{k_j}{k_{j+1}}) \exp(-k_j d_j) \end{bmatrix}, d_j \text{ is the thickness of the } j\text{th layer}$$

and $\zeta_j = \begin{cases} 1 & TE \\ \frac{n_{j+1}^2}{n_j^2} & TM \end{cases}$. Thus we can relate the field coefficients in the cover (A_c and B_c) with the coefficients in the substrate (A_s and B_s):

$$\begin{bmatrix} A_s \\ B_s \end{bmatrix} = T \begin{bmatrix} A_c \\ B_c \end{bmatrix} \tag{3.2}$$

$$T = T_N \cdots T_1 T_c = \begin{bmatrix} t_{11} & t_{12} \\ t_{21} & t_{22} \end{bmatrix}$$

For the guiding modes, the fields should be evanescent in the cap and the

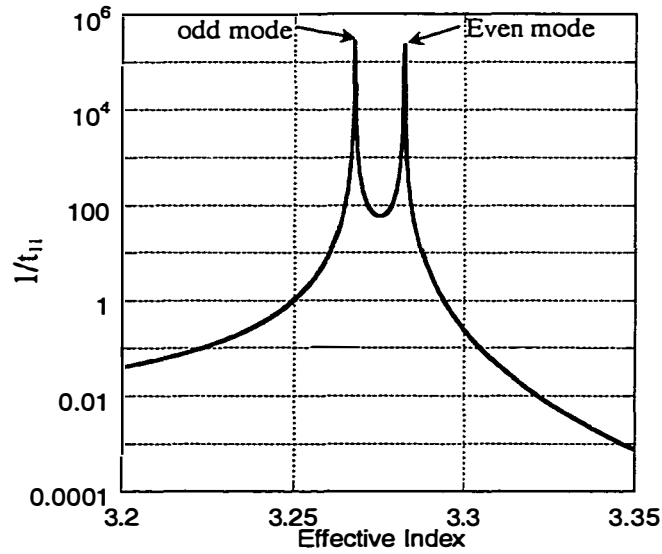


Figure 3.2. $1/t_{11}$ as a function of effective index for a 5 layer waveguide structure (see Figure 3.1)

substrate layers, so the conditions $A_s=0$ and $B_c=0$ results in the characteristic equation:

$$t_{11}(\beta)=0 \quad (3.3)$$

For lossless waveguides, all roots of equation (3.3) are real. It is simple to find all roots in a real axis. The simplest way is to plot $1/|t_{11}|$ as a function of effective index, the peaks in this plot correspond to the eigenvalues of all guiding modes. Figure 3.2 is the plot $1/|t_{11}|$ for the coupler structure (shown in Figure 3.1). This coupler includes two $0.5 \mu\text{m}$ InGaAsP ($n=3.371$) guiding layers and a $0.6 \mu\text{m}$ InP ($n=3.167$) coupling layer. The two peaks correspond to the even (symmetric) and odd (anti-symmetric) modes.

For general waveguides with complex refractive indices or leaky waveguides (such as anti-resonant-reflecting optical waveguides (ARROWs), see Appendix B), the effective indices are complex due to the loss. So the root searching of Equation (3.3) must be carried in the complex plane. An iterative numerical method is needed to find the complex effective index. A simple approach called the "downhill" method [2] is used for complex root searching. This algorithm works in the following way. First, the starting value n_0 of the effective index is chosen to be the solution of the eigenvalue equation without the imaginary part of the index. Then $|t_{11}|$ is determined at $n_0 \pm \delta_1$ and $n_0 \pm i\delta_2$ where δ_1 and δ_2 are the step size along the real and imaginary axes. The argument of the smallest $|t_{11}|$ from the above five points is chosen as the next starting point. If the old and new starting points are identical, step sizes are reduced to $0.1\delta_1$ and $0.1\delta_2$. The iteration is ended when step sizes are smaller than the preset value.

3.3 Effective Index Method (EIM)

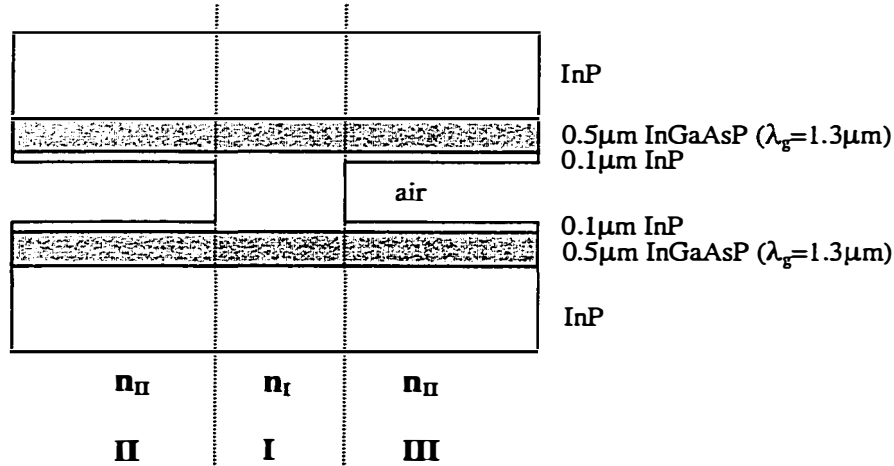


Figure 3.3. The structure of the 3D vertical coupler

For any slab waveguides in which the modes are only guided in one dimension, the mode effective index and the field profile can be rigorously evaluated using TMM. For practical applications, two-dimensional guiding is required (both in the transverse and lateral directions). A number of numerical methods are available to solve the modal properties of the 3D waveguides. Among these methods, the effective index method [3] is popular and easy to implement. This method logically breaks the three-dimensional guide into two sequential slab waveguide problems, which can be easily solved by TMM. In the following, we use the vertical coupler as an example to describe EIM briefly.

Figure 3.3 is a 3D vertical coupler, which can be fabricated by the wafer bonding technique (see chapter 4). To use EIM, first, the structure is sliced vertically to three parts I, II and III. The effective indices n_I , n_{II} and n_{III} are evaluated for each part. Then the three new effective indices are now used to form a new slab waveguide. Thus the mode index can be solved again by using TMM. To maintain the polarization in the same direction, the mode polarization in the second step should be opposite to that in the first step. Although EIM is an

approximate method, and is restricted by the assumption of the slowly varying field along the second step direction, it is still valid for the fundamental mode of all waveguide cross-sectional shapes and the first two normal modes of the weakly coupled directional coupler. We will compare the calculation results from EIM with Beam Propagation Method (BPM) results in Chapter 4.

3.4 Coupled Mode Theory and Normal Mode Theory

3.4.1 Coupled mode theory (CMT)

Vertical directional couplers are the basis of all work in this dissertation. To

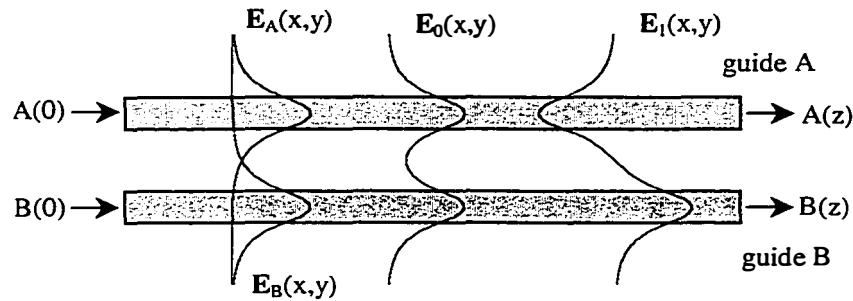


Figure 3.4. Illustration of the individual ($E_A(x,y)$, $E_B(x,y)$) and normal ($E_0(x,y)$, $E_1(x,y)$) modes of a directional coupler

analyze these coupled waveguide structures, coupled mode theory (CMT) [4-6] has been extensively used. CMT is essentially a perturbation approach that centers on the phase relationship and the mode field overlap between coupled waveguides. The theory is useful in providing a rational but somewhat oversimplified description of field interaction and power transfer in coupled waveguides.

Consider a coupler with two waveguides as shown in Figure 3.4, the longitudinal variation of the field amplitudes $A(z)$ and $B(z)$ in the waveguides can be written as

$$\begin{aligned} \frac{d}{dz} A(z) &= i\nu_a A(z) + i\kappa_{ab} B(z) \\ \frac{d}{dz} B(z) &= i\nu_b B(z) + i\kappa_{ba} A(z) \end{aligned} \quad (3.4)$$

where the propagation constants are:

$$\begin{aligned} \nu_a &= \beta_a + [\tilde{\kappa}_{aa} - C_{ab}\tilde{\kappa}_{ba} + C_{ab}C_{ba}(\beta_a - \beta_b)] / (1 - C_{ab}C_{ba}) \\ \nu_b &= \beta_b + [\tilde{\kappa}_{bb} - C_{ba}\tilde{\kappa}_{ab} + C_{ab}C_{ba}(\beta_b - \beta_a)] / (1 - C_{ab}C_{ba}) \end{aligned}$$

and the coupling coefficients are:

$$\begin{aligned} \kappa_{ab} &= \{\tilde{\kappa}_{ab} + C_{ab}[\beta_a - \beta_b - \tilde{\kappa}_{bb}]\} / (1 - C_{ab}C_{ba}) \\ \kappa_{ba} &= \{\tilde{\kappa}_{ba} + C_{ba}[\beta_b - \beta_a - \tilde{\kappa}_{aa}]\} / (1 - C_{ab}C_{ba}) \end{aligned}$$

β_a and β_b are the propagation constants of the individual waveguides. C_{ab} and C_{ba} describe the individual waveguide mode overlap:

$$C_{pq} = \frac{1}{2} \iint (E'_q \times H'_p) dx dy \quad p, q = a, b.$$

$\tilde{\kappa}_{ab}$ and $\tilde{\kappa}_{ba}$ represent the perturbations to the individual waveguides:

$$\tilde{\kappa}_{pq} = \frac{\omega}{4} \iint \Delta\varepsilon_q (E'_p \cdot E'_q - E_p^z \cdot E_q^z) dx dy.$$

$\Delta\varepsilon_q = \varepsilon' - \varepsilon_q$ is the perturbation. Where ε_q ($q=a, b$) is the permittivity of the individual waveguide. E_a and E_b are the normalized fields of the fundamental modes of the unperturbed waveguides A and B.

The above theory is the improved coupled mode theory, which was developed by Hardy [5] and Chuang [6]. For weak coupling cases (such as directional coupler filters), we can neglect the self-coupling terms ($\tilde{\kappa}_{aa}$, $\tilde{\kappa}_{bb}$) and the cross mode overlap terms (C_{ab} , C_{ba}), and Equation (3.4) will be reduced to the

familiar coupled mode equation. For strongly coupling cases, these terms must be included [6, 7].

The solution of Equation (3.4) can be expressed in matrix format:

$$\begin{bmatrix} A \\ B \end{bmatrix} = \begin{bmatrix} \cos \psi z - i \frac{\Delta}{\psi} \sin \psi z & i \frac{\kappa_{ab}}{\psi} \sin \psi z \\ i \frac{\kappa_{ba}}{\psi} \sin \psi z & \cos \psi z + i \frac{\Delta}{\psi} \sin \psi z \end{bmatrix} \begin{bmatrix} A_0 \\ B_0 \end{bmatrix} \quad (3.5)$$

Where $\Delta = \frac{\nu_b - \nu_a}{2}$, $\psi = \sqrt{\Delta^2 + \kappa_{ab}\kappa_{ba}}$. For any waveguide coupling systems (no grating), Equation (3.5) can always be used to synthesize and optimize the performance.

With input boundary conditions $A(0)=1$, $B(0)=0$, the output power [8] is:

$$P_a(z) = 1 - \left(\frac{1 - C_{ab}C_{ba}}{1 + \Delta^2} \right) e^{2 \sinh^{-1} C \Delta} \sin^2(\sqrt{\kappa_{ab}\kappa_{ba}(1 + \Delta^2)}z) \quad (3.6)$$

$$P_b(z) = C_{ab}C_{ba} + \frac{1 - C_{ab}C_{ba}}{1 + \Delta^2} \sin^2(\sqrt{\kappa_{ab}\kappa_{ba}(1 + \Delta^2)}z) \quad (3.7)$$

3.4.2 Normal Mode Theory (NMT)

Coupled mode theory is formulated on the basis of the mode fields and propagation constants of the individual unperturbed waveguides. It is still an approximation approach. As we have seen in last subsection, a lot of numerical integrals are needed before applying the CMT equation. It is not efficient. A more precise description of the guiding characteristics of a directional coupler is given in terms of the structure normal modes, (denominated "supermodes" or "system modes"). These normal modes are an exact solution of the wave equation. Considering the structure in Figure 3.4 as a whole composite waveguide, generally, there are two normal modes (supermodes): symmetrical (in-phase) mode (or even mode) and anti-symmetrical (out of phase) mode (or odd mode).

We denote the two normal mode field profiles as \mathbf{E}_e , \mathbf{E}_o (shown in Figure 3.4) and the propagation constants as β_e and β_o .

Although individual modes can be used to construct the normal modes via CMT, it is not accurate to do so in strongly coupled devices. The more accurate method is to use the TMM (combined with EIM for 3D structures) directly to the composite structure to solve the normal modes. This allows us to determine the normal field profiles and the propagation constants accurately, even in the case of strong coupling. It is worth noting that the coupling coefficients can be expressed in terms of normal modes as:

$$\beta_e + \beta_o = \beta_a + \beta_b \quad (3.8)$$

$$\sqrt{\Delta^2 + \kappa_{ab}\kappa_{ba}} = \frac{\beta_e - \beta_o}{2} \quad (3.9)$$

It is considerably more convenient than the integral to find the coupling coefficient in CMT if $\kappa_{ab} \approx \kappa_{ba}$, which is true for most of cases.

After constructing the normal modes, power transfer between coupled waveguides under normal mode theory can be described by interference between normal modes and longitudinal coupling between normal modes and individual waveguide modes. In the weak coupling case, the individual modes may be represented in terms of normal modes. For simplicity, we consider two identical coupled waveguides ($\mathbf{E}_a = \mathbf{E}_b$) with the input from waveguide a:

$$\begin{aligned} E_a(x, y) &= \frac{1}{\sqrt{2}} [\eta_e E_e(x, y) \exp(-i\beta_e z) + \eta_o E_o(x, y) \exp(-i\beta_o z)] \\ E_b(x, y) &= \frac{1}{\sqrt{2}} [\eta_e E_e(x, y) \exp(-i\beta_e z) - \eta_o E_o(x, y) \exp(-i\beta_o z)] \end{aligned} \quad (3.10)$$

Where η_e and η_o are the excitation efficiency between the individual modes and the normal modes:

$$\eta_i = \iint E_a(x, y) E_i(x, y) dx dy, \quad i=e,o.$$

The output power from waveguide a and b can be expressed as:

$$P_a(z) = 2(\eta_e \eta_o) \cos^2\left(\frac{\beta_e - \beta_o}{2} z\right) + \frac{(\eta_e - \eta_o)^2}{2} \quad (3.11)$$

$$P_b(z) = 2(\eta_e \eta_o) \sin^2\left(\frac{\beta_e - \beta_o}{2} z\right) + \frac{(\eta_e - \eta_o)^2}{2} \quad (3.12)$$

3.5 Beam Propagation Method (BPM)

Undoubtedly, the most precise numerical approach of the waveguide devices is Beam propagation method (BPM) [9, 10]. BPM determines an approximate solution to the wave (Helmholtz) equation using several techniques such as Fourier transform or finite difference methods in the well-known parabolic or paraxial approximation, imposing the appropriate boundary conditions according to the changing index distribution. In this dissertation, a commercial BPM software [11] called BeamPROP, developed by Rsoft Inc., is used. Principally, BPM provides a general simulation tool for computing the propagation properties of light wave in arbitrary waveguide geometries if the refractive index distribution $n(x,y,z)$ can be described. But it takes a long time for BPM to get accurate results, particularly for 3D and long devices, from several minutes to several hours or even several days. It is not an efficient way to design and optimize waveguide devices. Generally, we always use approximate methods (EIM via TMM) to get the initial design structure, then modify and refine the structure by BPM.

3.6 Design of vertical couplers

In this section, we will use the methods discussed in the above sections to design and simulate couplers. Since a directional coupler is characterized by the coupling length and the extinction ratio, we will first give the coupling length from CMT and NMT. Then we will discuss the extinction ratio of vertical couplers with ultra-short coupling lengths.

3.6.1 Coupling length

For weak coupling symmetrical directional couplers (the two waveguides are identical), $\kappa_{ab} = \kappa_{ba} = \kappa$ and $\Delta = 0$. When light is launched into an input waveguide, the minimum length required for one to achieve complete power transfer from waveguide A to waveguide B is defined as the coupling length L_c :

$$L_c = \frac{\pi}{2\kappa} \quad (3.13)$$

which can be derived from (3.7).

Under normal mode theory, the coupling length can be rewritten as

$$L_c = \frac{\lambda}{2(n_e - n_o)} = \frac{\lambda}{2\Delta n}, \quad (3.14)$$

from (3.12), where n_e and n_o are the effective indices of even and odd supermodes, λ is the free space wavelength. Therefore, the coupling length can be easily found by calculating the effective indices of the normal modes.

3.6.2 Extinction ratio

A. Straight coupler

A high extinction ratio is the most important requirement for a coupler. Although we would like to get all the power from one of two output waveguides, it is generally observed that a small amount of power always exists in another output waveguide, causing cross talk problem. Besides the imperfect processing technology, there are some inherent limitations, such as unequal excitation of an input mode to the symmetric and anti-symmetric normal modes [12], to cause cross talk. Checking equation (3.6), we can see that complete power transfer requires $C_{ab}C_{ba}=0$ for synchronous coupling ($\Delta=0$) at positions $z=(2n+1)l_c$. But condition $C_{ab}C_{ba}=0$ can never be satisfied for coupled waveguides because it means there is no interaction (coupling) between two individual waveguides.

From Equations (3.6) and (3.7), it is easy to get the extinction ratio at the coupling length for synchronous coupling:

$$ER = \frac{P_a(z = L_c)}{P_b(z = L_c)} = C_{ab} C_{ba} \quad (3.15)$$

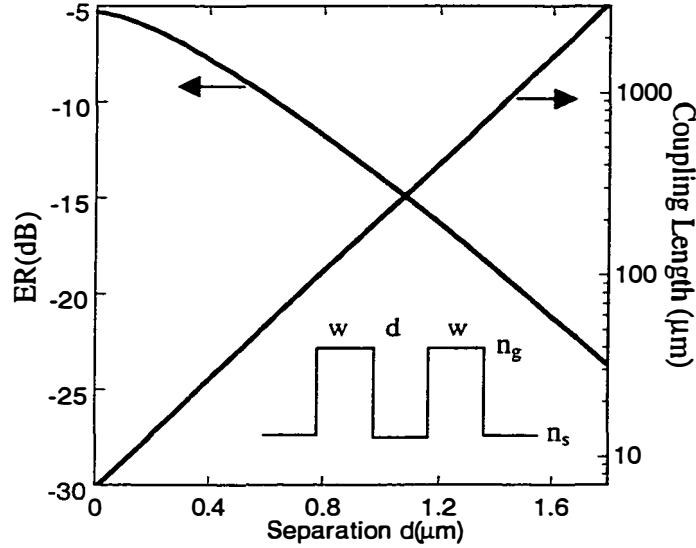


Figure 3.5. Extinction ratio and coupling length vs. the waveguide separation d .

It is clear that the incomplete power transfer is because of the overlap between two individual waveguide modes. The shorter the coupling length is, the worse the cross-talk gets.

From the viewpoint of normal modes, we can understand the extinction ratio more clearly. From Equations (3-11) and (3-12), we can derive the extinction ratio:

$$ER = \frac{P_a(z = L_c)}{P_b(z = L_c)} = \left(\frac{\eta_e - \eta_o}{\eta_e + \eta_o} \right)^2 \quad (3.16)$$

In general, the excitation to even supermode η_e is stronger than that to odd mode η_o . Thus the cross-talk always exists. Further, (3.16) can be related to the overlap of two individual modes:

$$ER = \left(\frac{\eta_e - \eta_o}{\eta_e + \eta_o} \right)^2 = \left(\frac{\iint E_a(x, y)(E_e(x, y) - E_o(x, y)) dx dy}{\iint E_a(x, y)(E_e(x, y) + E_o(x, y)) dx dy} \right)^2$$

$$\approx \left(\frac{\iint E_a(x, y)E_b(x, y) dx dy}{\iint E_a(x, y)E_a(x, y) dx dy} \right)^2 \quad (3.17)$$

Where we assume $\eta_e \approx \eta_o$. It is a good approximation for most couplers.

Figure 3.5 shows the extinction ratio (calculated from the individual mode overlap) and the coupling length (calculated using NMT) as a function of the separation of two waveguides. The structure is shown in Figure 3.5. The parameters used in the calculations are $w=0.5 \mu\text{m}$, $n_s=3.167$, $n_g=3.371$, $\lambda=1.55 \mu\text{m}$. Although the extinction ratio has been overestimated by the mode overlap, it is obvious that the crosstalk is very serious when the coupling length becomes short.

To improve the extinction ratio for a coupler with a very short coupling length, introduction of a slight asymmetry between two strongly coupled waveguides has been suggested [6, 7]. The basic idea is to equalize the overlap

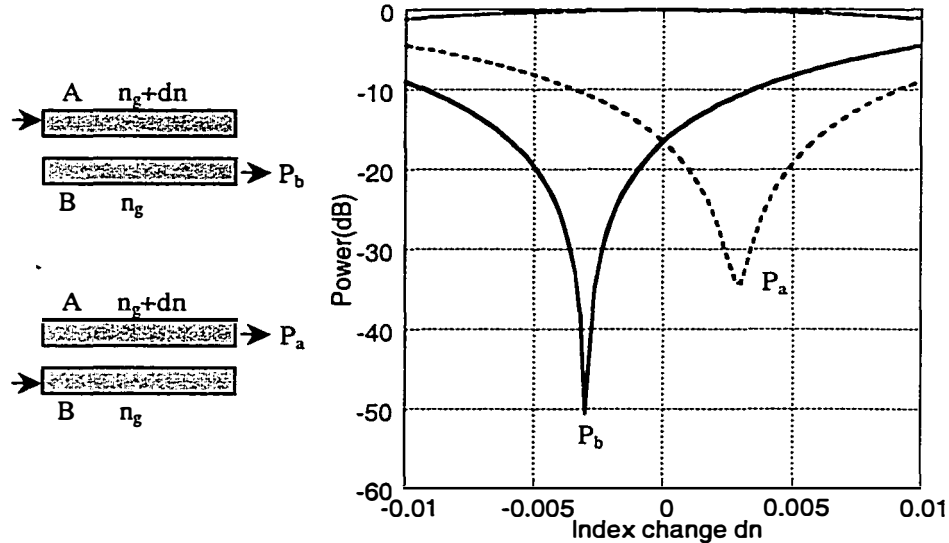


Figure 3.6. The output as a function of the index change.

integral of the input individual waveguide mode with the even and odd supermodes. We use BPM to simulate the coupler structure in Figure 3.5 ($d=0.6 \mu\text{m}$). Figure 3.6 shows the output power of two waveguides A and B as a function of index change of the waveguide A. When $dn=0$, the extinction ratio is only -16 dB and the coupling length is $52.7 \mu\text{m}$. With the introduction of a slight asymmetry ($dn=-0.003$), the extinction ratio can be increased to -50 dB and the

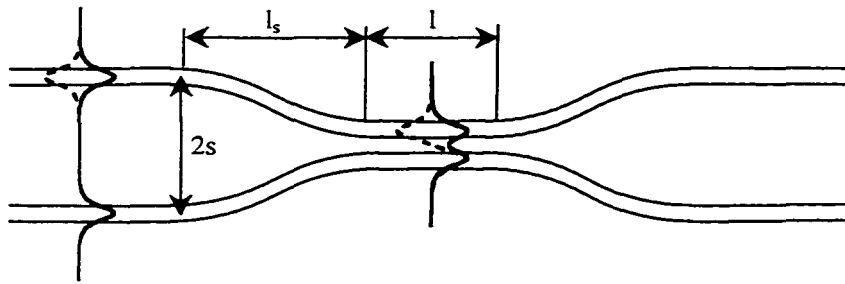


Figure 3.7. Symmetrical coupler with separated inputs and outputs. Normal modes at input and center coupling regions are plotted.

coupling length is only changed to $51.9 \mu\text{m}$, if the input is from waveguide A. It seems that this was a promising method to improve the extinction ratio. But when we change the input to the other waveguide B, the extinction is only -10 dB. To get the maximum extinction ratio, now the index change dn of waveguide A should be 0.003. This is because we cannot modify the individual modes of both waveguides at the same time to get the equal excitation to the even and odd supermodes. Therefore this method is only suitable to 1×2 structures. For 2×2 devices, the symmetry should be kept to exhibit the equal extinction ratios from their two output ports.

B. Coupler with well separated inputs and outputs

From the normal mode theory point of view, the high extinction ratio requires the same excitation amplitudes (η_e and η_o). As we know, if the structure

is symmetric (identical guides) and the guides are sufficiently well separated, the two excitation amplitudes will be identical when one guide is excited, regardless of the excitation distribution. This is the ideal initial condition. Therefore, tapering the input and output waveguides of a coupler may eliminate crosstalk [13]. We consider a symmetrical coupler consisting of a symmetric converging waveguide flare, the center guide region, and the symmetric diverging waveguide

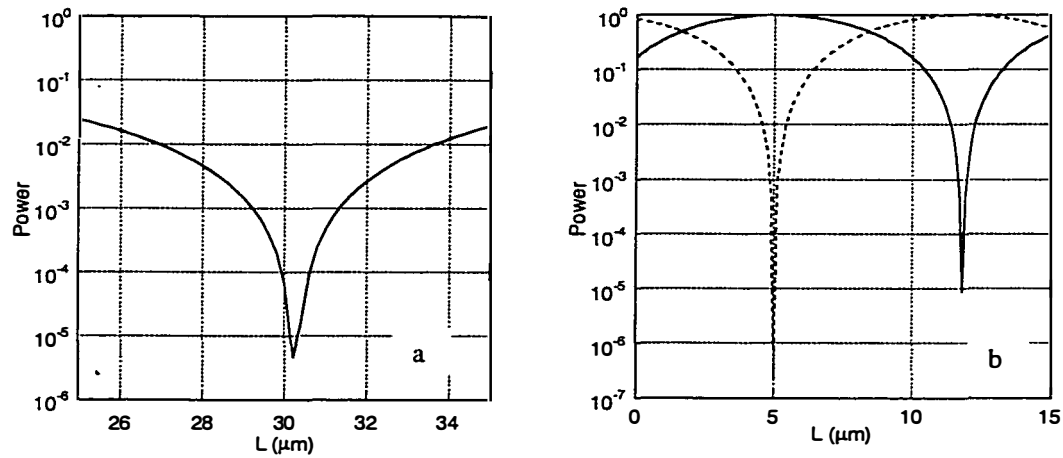


Figure 3.8. The output power as a function of the coupler length L.
(a). $d=0.6\mu\text{m}$; (b). $d=0$

flare, with a constant amplitude excitation ratio, shown in Figure 3.7. Since the two normal modes are always orthogonal and they don't exchange energy, the output state of the coupled guides after the guides are again well separated can still expressed as Equations (3.11) and (3.12):

$$P_a(z) = 2(\eta_e \eta_o) \cos^2\left(\frac{\phi}{2}\right) + \frac{(\eta_e - \eta_o)^2}{2} \quad (3.18)$$

$$P_a(z) = 2(\eta_e \eta_o) \sin^2\left(\frac{\phi}{2}\right) + \frac{(\eta_e - \eta_o)^2}{2} \quad (3.19)$$

Where Φ is the total relative propagation phase difference between two normal modes and the adiabatic normal mode propagation is assumed. So the extinction ratio of a symmetrical coupler is entirely dependent on the relative mode amplitude and the profiles at the coupler end point where the coupling becomes negligible. We still use the same center coupler structure as in Figure 3.5 to simulate the performance of the coupler with well separated inputs and outputs. Figure 3.8 shows BPM calculated results with different separations. The S-bend parameters are $s=10\mu\text{m}$ and $L_s=100\mu\text{m}$. With a proper tapering of the inputs and

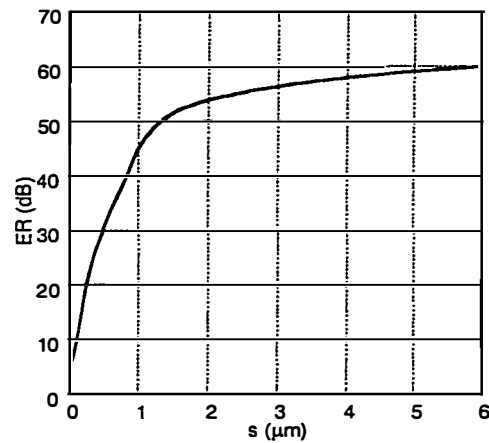


Figure 3.9. The extinction ratio as a function of the separation s between two input waveguides. $d=0$, $L_s=20s$.

outputs, the extinction ratio of $>50\text{dB}$ can always be achieved, even when the separation $d=0$ and the corresponding coupling length is only $6.8\mu\text{m}$. The relationship between the extinction ratio and the S-bend separation for a coupler with the separation $d=0$ in the center coupling region is shown in Figure 3.9. The separation between the inputs and outputs should be larger than $1\mu\text{m}$ to get $>30\text{dB}$ extinction ratio.

For a practical coupler, the separation of two input and output waveguides must be well separated to couple to fibers. The factors that affect the extinction ratio mainly include asymmetry from the imperfect fabrication and nonadiabatic

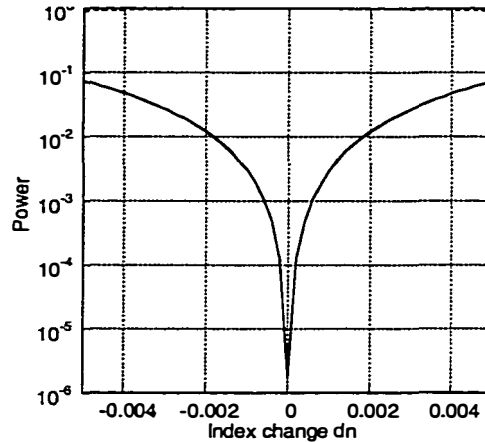


Figure 3.10. The output power of the coupler with well-separated input and output waveguides as a function of index change. $d=0.6\mu\text{m}$, $s=5\mu\text{m}$, $l_s=100\mu\text{m}$.

mode propagation in the tapering regions, which would result in different propagation losses for two normal modes. Figure 3.10 shows the output power at the coupling length with the index change of the input waveguide for $d=0.6\mu\text{m}$. To get >-30 dB extinction ratio, the index change must be smaller than 0.0007 ($\frac{dn}{n}=0.021\%$). This requirement will become more critical when the coupling length is longer. Figure 3.11 shows the index change tolerance to achieve -30 dB extinction ratio as a function of the separation d between two waveguides. The longer the coupling length is, the more symmetric the two coupling waveguides are to get a high extinction ratio. Since the imperfect fabrication always introduces a certain asymmetry between two waveguides, it is quite difficult to get a high extinction ratio for long directional couplers. Fortunately, to some extent, we can modify the waveguide parameters by post-adjustment, such as

applying a bias to change the waveguide index to compensate for the asymmetry to get a high extinction ratio.

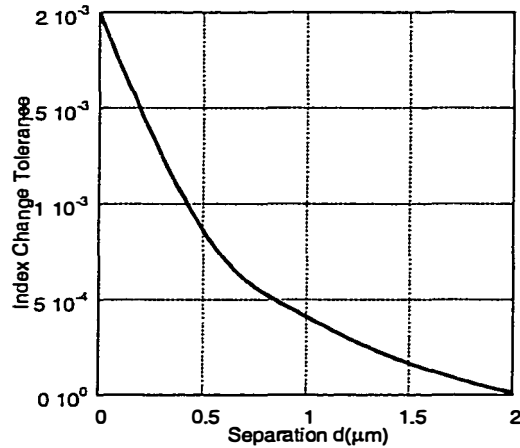


Figure 3.1.1. The index change tolerance as a function of the waveguide separation d to achieve -30dB extinction ratio.

3.7 Summary

In this chapter, some useful waveguide and coupler design and simulation techniques, including transfer matrix method, effective index method, coupled mode theory, normal mode theory and beam propagation method were reviewed. Based on these methods, we analyzed the coupling lengths and the extinction ratios for different couplers. One important result is that the extinction ratio is independent of the coupling length if the two input waveguides and output waveguides are separated enough to excite the two supermodes identically, which is true for most of the practical couplers. In this case, the symmetry between two waveguides is the key factor to get a high extinction ratio. The longer the coupling length is, the more critical the symmetry will be. Compared to horizontal couplers, vertical couplers have very short coupling length. If the two inputs and outputs can be well separated, the high extinction ratio of vertical couplers will be more easily achieved than horizontal couplers.

References

- [1] J. Chilwell and I. Hodgkinson, "Thin-films field-transfer matrix theory of planar multilayer waveguides and reflection from prism-loaded waveguides," *Journal of the Optical Society of America A*, vol. 1, pp. 742-53, 1984.
- [2] H. Bach, "On the downhill method," *Communications of the ACM*, vol. 12, pp. 675-7, 1969.
- [3] K. S. Chiang, "Analysis of optical fibers by the effective-index method," *Appl. Opt.*, vol. 25, pp. 348-54, 1986.
- [4] A. Yariv, "Coupled-mode theory for guided-wave optics," *IEEE J. Quantum Electron.*, vol. 9, pp. 919-33, 1973.
- [5] A. Hardy, W. Streifer, and IEEE, "Coupled mode theory of parallel waveguides," *J. Lightwave Technol.*, vol. 3, pp. 1135-46, 1985.
- [6] S. Chuang, "A coupled mode formulation by reciprocity and a variational principle," *J. Lightwave Technol.*, vol. 5, pp. 5-15, 1987.
- [7] K. Boo-Gyoun, A. Shakouri, L. Bin, and J. E. Bowers, "Improved extinction ratio in ultra short directional couplers using asymmetric structures," *Japanese Journal of Applied Physics, Part 2 (Letters)*, vol. 37, pp. L930-2, 1998.
- [8] S. L. Chuang, *Physics of optoelectronic devices*: John Wiley & Sons. Inc., 1995.
- [9] M. D. Feit and J. A. Fleck, Jr., "Computation of mode properties in optical fiber waveguides by a propagating beam method," *Appl. Opt.*, vol. 19, pp. 1154-66, 1980.
- [10] R. Scarmozzino and R. M. Osgood, Jr., "Comparison of finite-difference and Fourier-transform solutions of the parabolic wave equation with

- emphasis on integrated-optics applications," *J. Opt. Soc. Am. A*, vol. 8, pp. 724-31, 1991.
- [11] R. Inc., "BeamPROP Version," , 3.0 ed. NY: Research Software, 1993-1999.
- [12] C. Kuo-Liang and W. Shyh, "Cross-talk problems in optical directional couplers," *Appl. Phys. Lett.*, vol. 44, pp. 166-8, 1984.
- [13] H. A. Haus and N. A. Whitaker, Jr., "Elimination of cross talk in optical directional couplers," *Appl. Phys. Lett.*, vol. 46, pp. 1-3, 1985.

Chapter 4

Fused Vertical Coupler and Switch

A coupler is a basic component in photonic integrated circuits and fiber optic communications. They have been used widely as power splitters [1], filters [2-4], multiplexers and demultiplexers [5-10], optical switches [11], modulators [12, 13]. Different types of vertical couplers are the core elements in this dissertation. In this chapter, we will investigate wafer fused symmetric waveguide directional vertical couplers and switches. First, we will compare vertical coupler and horizontal couplers in Section 4.1. The simulation results of 3D vertical couplers will be given in Section 4.2. The fabrication and characterization of fused vertical couplers are described in Section 4.3. By inverting the crystal symmetry, push-pull operated fused vertical coupler switches and their fabrications will be discussed in Section 4.4. In Section 4.5, a vertical coupler with laterally separated inputs and outputs will be described.

4.1 Vertical coupler and horizontal coupler

There are two kinds of directional coupler structures. Conventionally, directional couplers are fabricated on a plane using two separated parallel identical guides (see Figure 4.1 (a)); these are known as horizontal couplers. The separation determines the device length. Generally the device length at least equals to one coupling length L_c . Material and fabrication technique constraints (lithography and the need for well-defined etching techniques) have set the coupling length limits of such a horizontally arranged coupler, which usually is several mm. Therefore, horizontal couplers require large space consumption and also have a high device capacitance, which means that it is difficult to achieve high speed

operation and a travelling wave configuration is necessary. For a long coupler

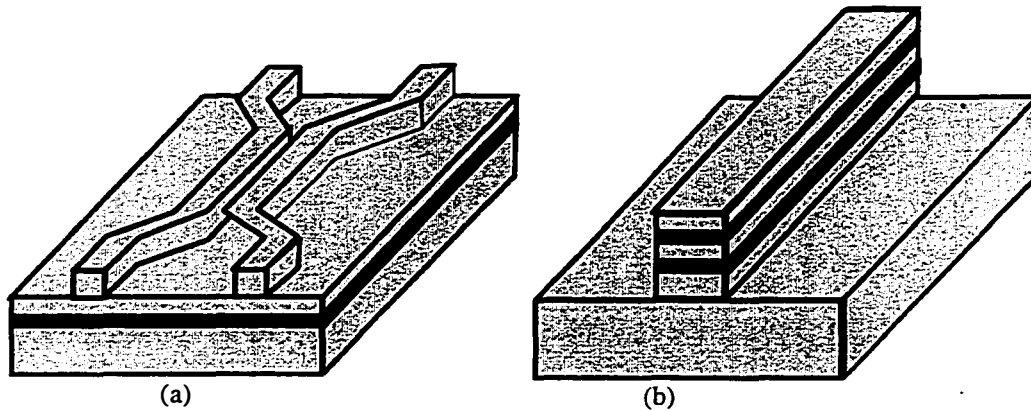


Figure 4.1. The schematic drawing of horizontal coupler (a) and vertical coupler (b).

switch, a high energy will be required to realize optical switching.

A different coupler geometry is used for vertical couplers where the two waveguides are stacked vertically (see Figure 4. 1 (b)). The advantage of such

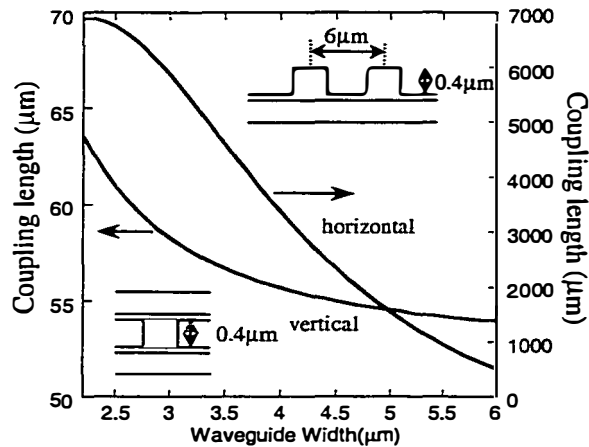


Figure 4.2. Coupling length of the vertical coupler and horizontal coupler as a function of waveguide width

couplers in comparison to conventional horizontal couplers is due to the precise control of the thickness and the separation between two waveguides, which are determined by the state-of-the-art MBE or MOCVD growth. Since the separation

between two guiding layers can be controlled to be smaller than $1\mu\text{m}$, the coupling length can be shorter than $100\mu\text{m}$ [14, 18, 20]. Another advantage of vertical couplers is that the coupling length is much less sensitive to the ridge waveguide width and sidewall smoothness than the horizontal planar couplers. In fact, the difficulty in making reproducibly and uniformly very narrow gap ($<1\mu\text{m}$) horizontal couplers have mitigated their development for ultra short switching devices. Figure 4.2 shows the comparison of the coupling length as a function of waveguide width between a conventional ridge-loaded horizontal coupler and a vertical coupler. The horizontal coupler includes $0.5\mu\text{m}$ InGaAsP (bandgap $1.3\mu\text{m}$), $0.1\mu\text{m}$ InP slab layer and $0.4\mu\text{m}$ InP ridge. The centers of the two waveguides are separated by $6\mu\text{m}$. The vertical coupler has the same structure as before. It can be seen that a change of $1\mu\text{m}$ in waveguide width will change the coupling length about 40%. When the same waveguides are coupled vertically, the coupling length is about 2 orders of magnitude smaller and much less sensitive to waveguide width variation (4-5% change in coupling length for $1\mu\text{m}$ waveguide width change).

Because vertical couplers have very short coupling lengths, they have been studied by various research groups to realize compact optical switches and modulators [14-19] (see Table 4.1). But there is an inherent problem, which limits the practical applications of conventional vertical couplers. In conventional vertical couplers, the two input or output waveguides are so close together that direct coupling of individual waveguides with fibers is impossible. As discussed in the last chapter, the extinction ratio is also limited if the input and output waveguides cannot be well separated. In this dissertation, we will solve this problem by using the wafer bonding technique to process 3D vertical couplers with laterally separated inputs and outputs.

	Wavelength (μm)	Operating Voltage (V)	Extinction Ratio (dB)	Coupling Length (μm)
K. Tada et al. [15] Univ. of Tokyo (1974)	1.15	10	no	no
M. Cada et al. [16] Nova Scotia, Canada (1989)	0.85	1 V/cm	no	160
J. Cavailles et al. [17] Philips, France (1989)	0.88	5	no	90-110
M. Kohtoku et al. [18] Tokyo Inst. Tech. (1991)	1.57	20	no	170
F. Dollinger et al. [14] Munich, Germany (1996)	0.854	5	> 10	85
B. Boche et al. [19] Munich, Germany (1996)	0.86	4	> 16	no
B. Liu et al. [20] UCSB, US (1998)	1.55	12 (2.8)	- 15	62
S. Ikuta et al. [21] Yokohama, Japan (1998)	1.55	-	-	350

Table 4.1. Some examples of waveguide vertical couplers and switches.

4.2 Simulation of 3D Vertical Couplers

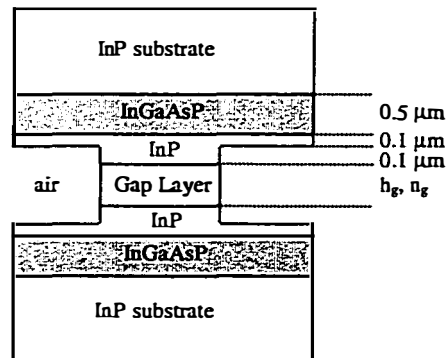


Figure 4.3. The structure of a 3D vertical coupler.

In this section, we will calculate the coupling length and the extinction-ratio of straight wafer fused waveguide structures. The fused vertical coupler (FVC) is shown in Figure 4.3. A ridge-loaded waveguide structure based on an InP

substrate, with a $0.5 \mu\text{m}$ InGaAsP ($\lambda_{\text{gap}}=1.3 \mu\text{m}$) core region, $0.1 \mu\text{m}$ InP cladding and $0.1 \mu\text{m}$ ridge height, is vertically coupled through a fused gap layer to an identical waveguide. The gap thickness varies from 0.1 to $0.6 \mu\text{m}$ with its index ranging from that of InP to that of InGaAsP ($\lambda_{\text{gap}}=1.4 \mu\text{m}$). The operation wavelength is $1.55 \mu\text{m}$.

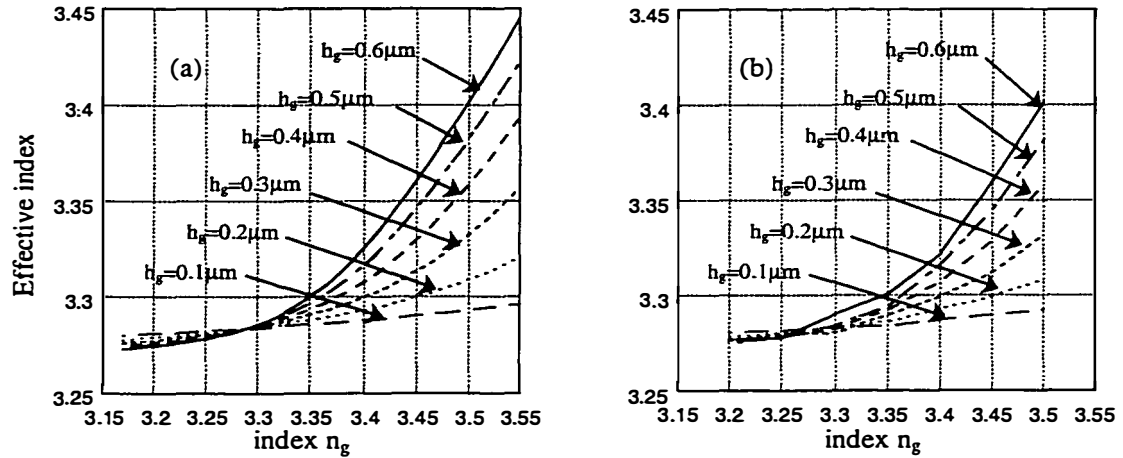


Figure 4.4. The effective index of a symmetric supermode calculated by EIM (a) and BPM (b).

Both the effective index method and the beam propagation method are used to find the effective indices of supermodes. Figure 4.4 and Figure 4.5 are the effective indices of symmetric and anti-symmetric modes as functions of gap layer index for different thickness of gap layer. We find that the results from EIM (a) match with BPM calculations (b) very well. But BPM needs several hours for each data point and EIM only several seconds. We should notice that the calculation step and length must be chosen carefully to get the exact results in BPM calculations. Sometimes, BPM results still have a small error as we see in Figure 4.5(b). From Figure 4.4, we can observe that the effective index of the symmetric mode is very sensitive to the change of the gap layer index, especially with the increase of the thickness of gap layer. Figure 4.5 shows the effective

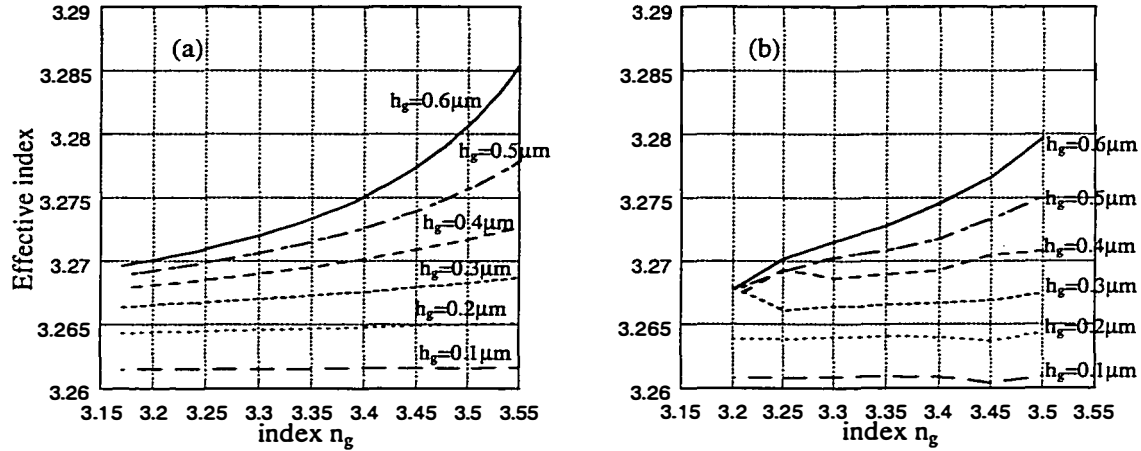


Figure 4.5. The effective index of antisymmetric supernode calculated by EIM (a) and BPM (b).

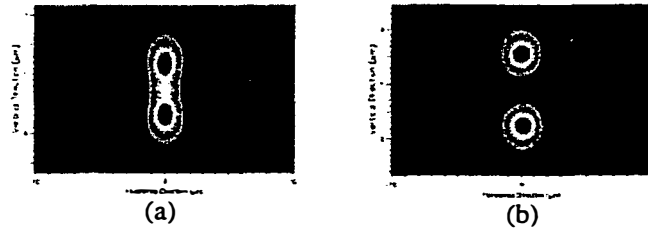


Figure 4.6. Symmetrical (a) and anti-symmetrical (b) supermodes of fused vertical coupler for $h_{\text{gap}}=0.4\mu\text{m}$ and $n_{\text{gap}}=3.4$

index of the anti-symmetric mode, which almost does not change with an increase in the index of the gap layer. The reason is that the intensity of the symmetric mode in the gap layer is much higher than that of the anti-symmetric mode. For the anti-symmetric mode, there is a zero field point in the center of gap layer (Figure 4.6). Figure 4.7 (a) shows the coupling length for different parameters of the gap layer. As expected, increasing the gap layer index reduces the coupling length. On the other hand, the dependence of the coupling length on the gap layer thickness shows a mixed behavior. When the gap region has small indices close to the InP layer, increasing its thickness will decouple the two waveguides and thus increase the coupling length. However, when the index of the gap layer is large (close to $1.3\mu\text{m}$ quaternary), the mode amplitude in this region is no longer

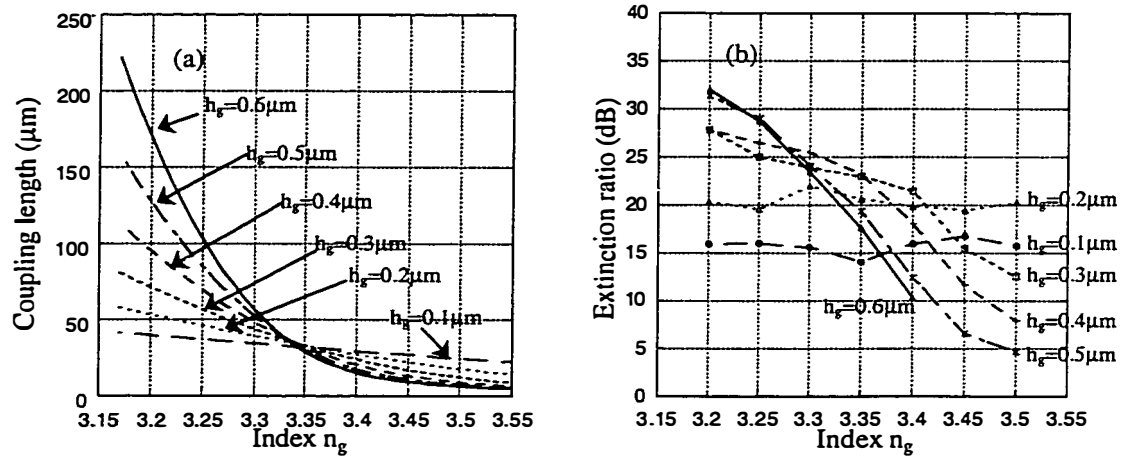


Figure 4.7. The coupling length (a) and the extinction ratio (b) as a function of gap layer index for different thickness of the gap layer.

exponentially decaying, but sinusoidal. So a thicker gap layer will increase the overlap integral between modes of adjacent waveguides and thus reduce the coupling length. When the gap layer thickness is more than $0.3\text{-}0.4\ \mu\text{m}$, an analysis based on the supermodes of three coupled waveguides is more appropriate, but the appearance of undesirable modes in the gap layer will deteriorate the performance of the directional coupler (see Figure 4.7(b)).

The extinction ratios are determined from BPM calculations. The eigenmode of one of the uncoupled waveguides was taken for the input field, and power transfer to the other waveguide as a function of propagation distance was monitored by BPM simulation. Fig. 4.7(b) displays the extinction ratio defined as the ratio of mode powers in the two waveguides after a coupling length. When the gap layer thickness and its index are high, the coupler has poor extinction ratios of 5 to 10 dB. In this case BPM simulation reveals 3 to 4 supermodes in the coupling region. In addition to the expected symmetric and antisymmetric eigenmodes, there are modes of the gap layer and some leaky modes. But for a wide range of parameters (gap thickness from 0.2 to $0.6\ \mu\text{m}$, and gap index from

3.15 to 3.35), extinction ratios of 20 to 32 dB can be achieved. From Fig. 4.7(a) we see that this corresponds to coupling lengths of the order of 40 to 220 microns. Since the two waveguides are very close, it is almost impossible to measure the extinction ratio experimentally. In practice, the two ridge structures will be separated by curved regions and the on/off ratio is limited by non ideal fabrication process, as we discussed in the last chapter.

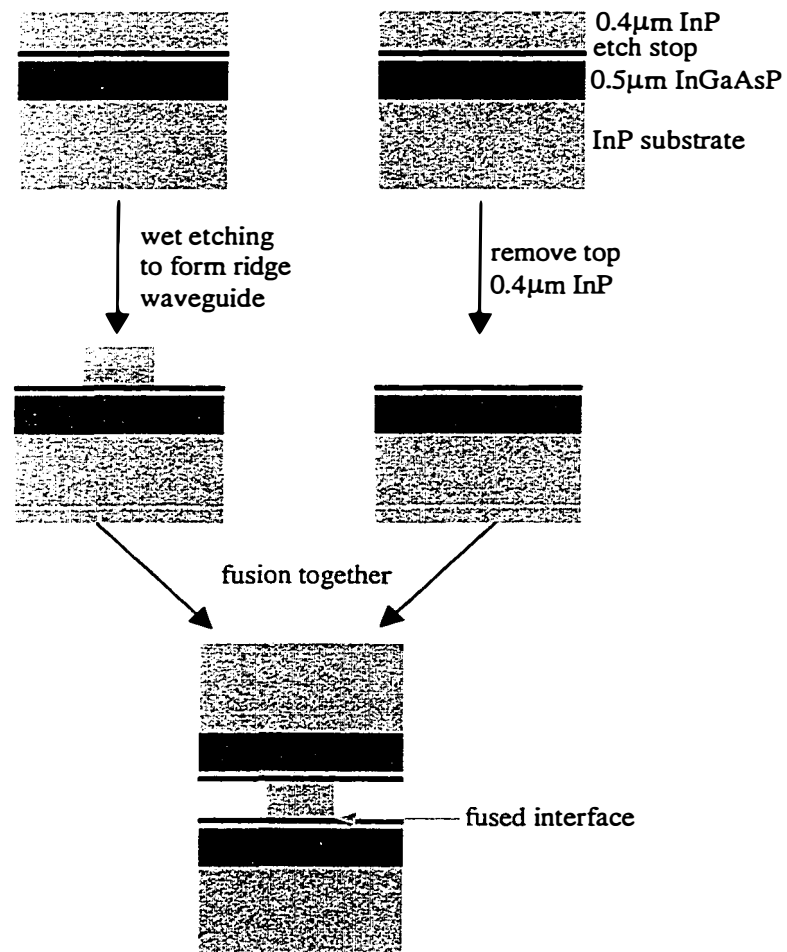


Figure 4.8. Fabrication of fused vertical coupler

4.3 Fused vertical coupler

In this section, we will experimentally study straight passive wafer fused vertical couplers (FVC).

4.3.1 Fabrication of fused vertical coupler

The structure of the fused vertical coupler is identical to that in Figure 4.3, with a $0.2 \mu\text{m}$ thick InP gap layer. The material was grown by metal-organic chemical-vapor deposition (MOCVD) and consisted of a $0.5 \mu\text{m}$ InGaAsP ($\lambda_{\text{gap}}=1.3 \mu\text{m}$) guiding layer on an InP substrate, followed by a $0.1 \mu\text{m}$ InP cladding layer, 20 nm InGaAsP ($\lambda_{\text{gap}}=1.15 \mu\text{m}$) etch stop layer and a $0.4 \mu\text{m}$ InP coupling layer. To fabricate the vertical coupler, two $8 \times 10 \text{ mm}^2$ samples are cleaved from the grown wafer. In the first sample the top $0.4 \mu\text{m}$ InP layer is removed. On the second sample, a ridge waveguide structure is fabricated using standard photolithography and selective wet etching, with SiN used as the wet etching mask. The ridges have

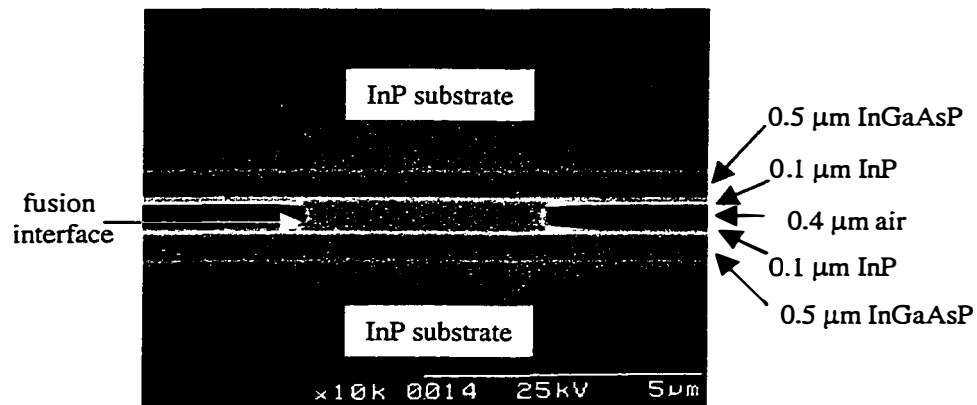


Figure 4.9. The stain etched SEM picture of a fused vertical coupler

$3\text{-}6 \mu\text{m}$ width, $0.4 \mu\text{m}$ height and they are separated by $125 \mu\text{m}$. The two samples are then fused together at a temperature of 630°C in a hydrogen atmosphere for 30 minutes. Figure 4.8 shows the fabrication procedure. Fig.4.9 is the stain etched

scanning electron microscope (SEM) picture of a finished fused vertical coupler (FVC). The fused interface is not visible, even after staining etch. There is mass transport at the edge of the ridge. This is beneficial to get a symmetric coupler and to improve the side wall flatness.



Figure 4.10. The near field patterns of the fundamental mode and the second order mode of fused vertical couplers.

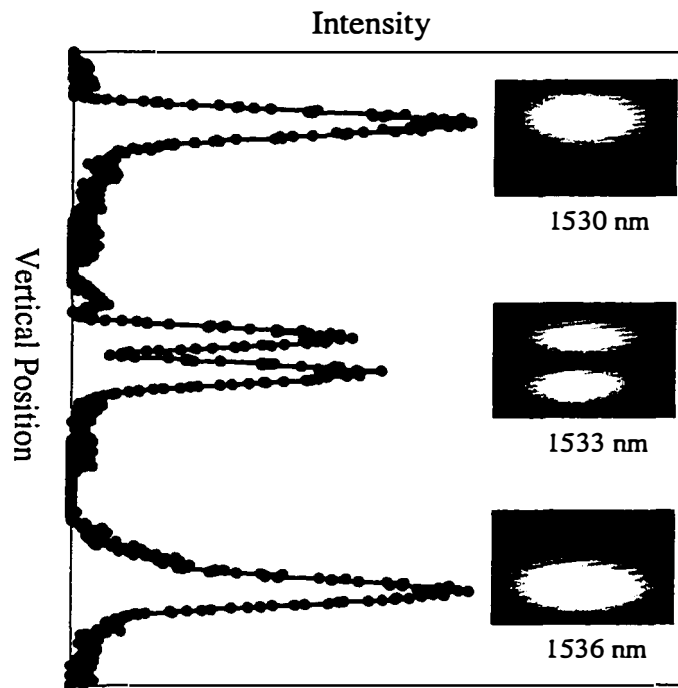


Figure 4.11. Photograph of the near-field pattern at 1530, 1533, and 1536 nm. The width of the ridge is 3 μm , and the distance between the upper and the lower WGs is 1.1 μm . The left curve is the profile of the near field.

4.3.2 Characterization of fused vertical coupler

In order to characterize fused vertical couplers, an IR camera with an 80 \times objective lens is used to record the near field patterns at the output of FVCs. The light is input from a 8 μm diameter single mode fiber. The light source is a tunable semiconductor laser. Figure 4.10 shows the near field patterns of the fundamental mode and the high order mode of fused vertical couplers. It can be seen that by changing the input wavelength, light is switched from the upper to the lower waveguide. The near field profiles at different wavelengths are shown in Figure 4.11. Since the shapes of the two waveguide modes are very similar, one can get a

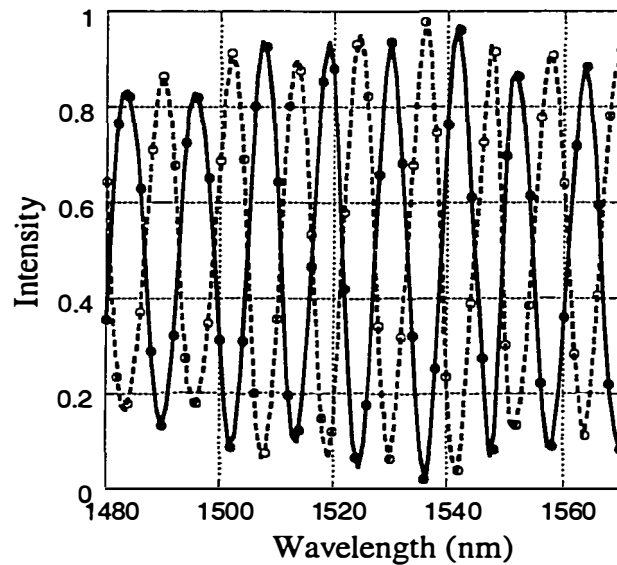


Figure 4.12. Measured intensity of the upper (closed circle) and lower (open circle) waveguides as a function of wavelength.

high extinction ratio. Our measurement shows the extinction ratio is about 15 dB. This is particularly difficult to achieve in conventional high mesa vertical couplers [18]. Figure 4.12 shows the intensities of the upper and lower waveguides as a function of wavelength. The length of the FVC is about 5.5 mm. From the oscillation period (about 12 nm) and considering material and

waveguide dispersions, the index difference between the even and odd modes can be estimated to be 0.0124. The corresponding coupling length is 62 μm at 1.55 μm that agrees very well with the theoretical value of 58 μm result from BPM calculations. One important advantage of this strong vertical coupling is the capability of attaining highly selective WDM multiplexers by making longer couplers with significant overcoupling. Figure 4.12 illustrates the possibility of lossless combination or splitting of two signals separated by just 6 nm. Multiple wavelength multiplexers/demultiplexers will be discussed in the next chapter. The wavelength selectivity of a FVC can be enhanced by using strong asymmetry in the waveguide structure, as we will see in Chapter 6.

4.4 Fused vertical coupler switch

One important application of vertical couplers is an optical switch. To achieve power switching in waveguide couplers, the waveguide index must be changed via the electro-optic effect or thermo-optic effect to introduce a phase mismatch ($\Delta\beta$) [22] between the optical fields in the two waveguides or change the coupling length of the couplers [23]. In this section, we will first analyze different switches and then fabricate a P-I-N fused vertical coupler switch.

4.4.1 Vertical $\Delta\beta$ and $\Delta\kappa$ coupler switches

To switch the input signal from one waveguide to another waveguide in a coupler, a certain perturbation must be introduced. There are two different types of perturbations. One is called $\Delta\beta$ switch, where a push-pull electrode configuration is used to induce positive and negative index change in different waveguides.

Figure 4.13 is a schematic drawing of a $\Delta\beta$ switch. Based on coupled mode theory (see 2.4.1), it is easy to find that the switch is in the cross state when

$$\kappa L = (2m - 1) \frac{\pi}{2}$$

or $L = (2m - 1)L_c$

(4.1)

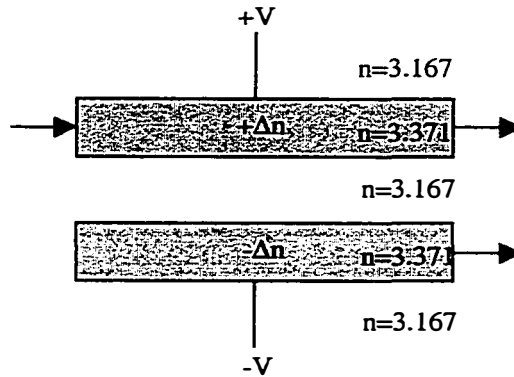


Figure 4.13. Schematic drawing of a $\Delta\beta$ switch.

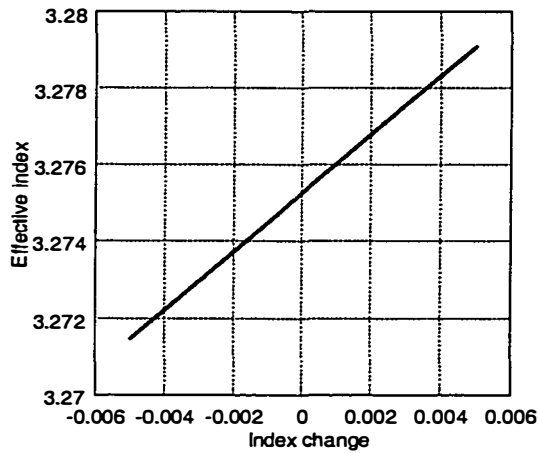


Figure 4.14. The effective index of the uncoupled waveguide mode with the index change of the guiding layer.

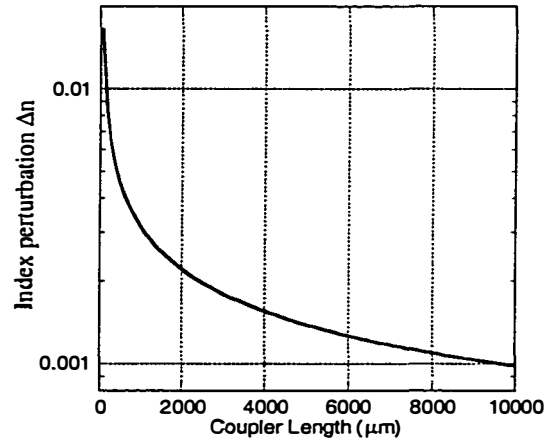


Figure 4.15. The needed switching index perturbation Δn as a function of coupler length.

where κ is the coupling coefficient, L is the coupler length, L_c is the coupling length, m is an integer.

The bar state requires that

$$(\kappa L)^2 + (\Delta L)^2 = (m\pi)^2$$

$$\text{or } \left(\frac{L}{L_c}\right)^2 + \left(\frac{\Delta\beta L}{\pi}\right)^2 = (2m)^2 \quad (4.2)$$

From Equations (4.1) and (4.2), we can find that complete switching depends on the initial state. When the coupler length is an odd multiple of the coupling length, $\Delta\beta$ modulation will drive the switch into the bar state. But when the initial state is the bar state, power switching is incomplete and crosstalk results. This disadvantage can be overcome by using alternative $\Delta\beta$ configurations [22]. Since $\Delta\beta$ switch represents an odd perturbation, it is the most efficient way to realize compact devices with small switching voltages. We take a simple 2D vertical coupler (see Figure 4.13) as an example, where the thickness of the two guiding layers is $0.5 \mu\text{m}$ and the separation between the two guiding layers is $0.6 \mu\text{m}$. First, the effective index of the uncoupled single waveguide mode with the index change of the guiding layer Δn is calculated using TMM, which is shown in Figure 4.14. Then the needed index perturbation Δn for switching can be obtained from Equation (4.2). Figure 4.15 shows the index perturbation as a function of the coupler length.

Another perturbation separate from $\Delta\beta$ switch perturbation is symmetric, called $\Delta\kappa$ switch. This perturbation cannot induce a relative phase shift in the waveguides, but instead it will modulate the coupling coefficient or the coupling length. Since the perturbation is symmetric, the supermodes will always remain orthogonal but with different propagation constants. The switching results from the dephasing between the two supermodes. The switching happens when

$$\Delta\kappa L = \frac{\pi}{2} \quad (4.3)$$

where $\Delta\kappa = \frac{\pi}{\lambda} \Delta(n_e - n_o)$ is the change of the coupling coefficient. We use the same coupler structure as in Figure 4.13 and consider two different index perturbations: case (a) index perturbation happens in both guiding layers and gap

layer; case (b) index perturbation only happens in gap layer, as shown in Figure 4.16. Figure 4.17 shows the calculated effective index difference $n_e - n_o$ between

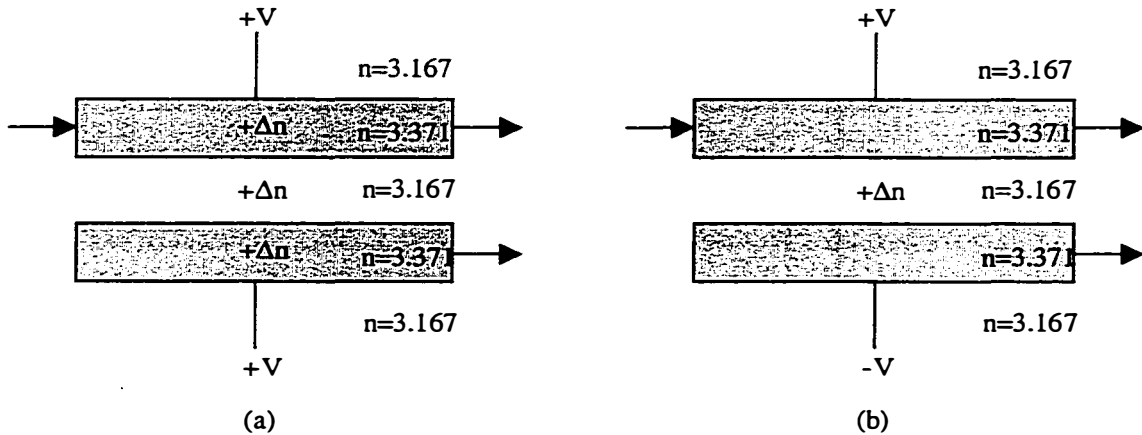


Figure 4.16. Schematic drawing of a $\Delta\kappa$ switch. (a) index perturbation happens in both guiding layers and gap layer. (b) index perturbation only happens in gap layer.

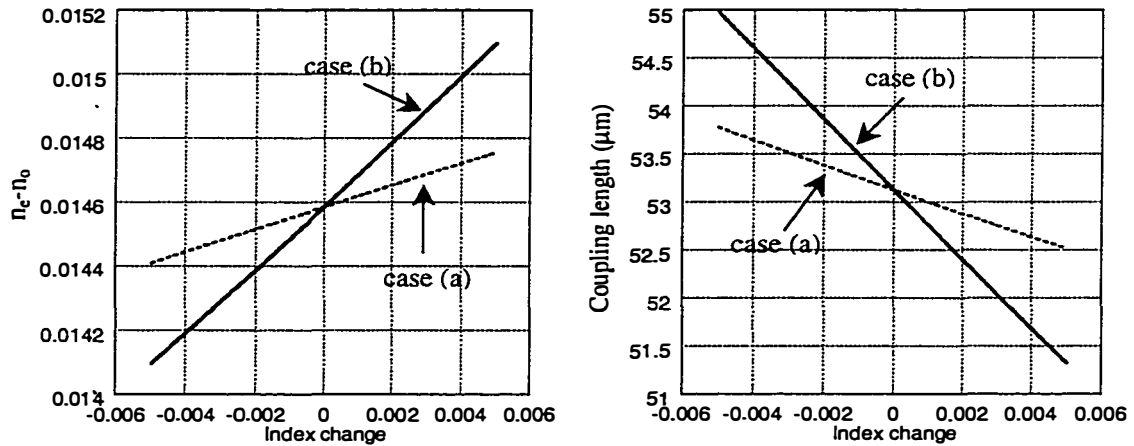


Figure 4.17. The calculated effective index difference between two supermodes and coupling length as a function of index perturbation for case (a) and (b)

two supermodes and the change of coupling length as a function of the index perturbation Δn for both case (a) and (b). Compared to case (a), case (b) is more sensitive to the index perturbation. This is because symmetric and anti-symmetric modes have almost the same intensities in the guiding layers, but the intensity of

the anti-symmetric mode is much smaller than that of the symmetric mode in the gap layer, which have been shown in 4.2. If we can reduce the optical loss induced by P-doping, case (b) is more promising for optical switching. Using Equation (4.3), we can estimate the index perturbation needed for switching. Figure 4.18 shows the switching index perturbation Δn as a function of coupler length. Compared to Figure 4.15, it is clear that the $\Delta\kappa$ switch needs much higher perturbation than the $\Delta\beta$ switch, especially when the device length is short. The main advantage of the $\Delta\kappa$ switch is that complete switching is possible whether the initial state is bar or cross and the relative ease for fabrication, especially for vertical couplers.

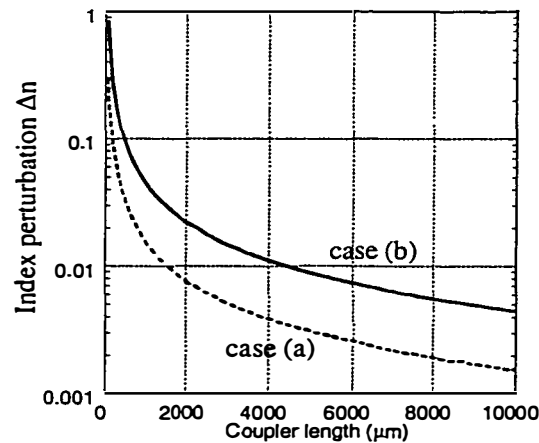


Figure 4.18. The switching index perturbation Δn as a function of coupler length

4.4.2 Fused vertical coupler switch via the thermo-optic effect

The structure of the P-I-N fused vertical coupler is identical to the one in Figure 4.9. The only difference is that the top InP substrate is p-doped and the bottom substrate is n-doped. Two wafers were grown using MOCVD. One was on a n+ InP substrate and the other one on a p+ substrate. These samples had a 0.5 μm InGaAsP ($\lambda_g=1.3 \mu\text{m}$) guiding layer, followed by a 0.1 μm InP cladding layer, a

20 nm InGaAsP ($\lambda_g=1.15 \mu\text{m}$) etch stop layer and finally a $0.4 \mu\text{m}$ InP coupling layer. All layers were undoped. Device fabrication starts by cleaving two approximately $10 \times 12 \text{ mm}^2$ samples from the grown wafers. In one sample the top $0.4 \mu\text{m}$ InP layer is removed. On another sample, a ridge waveguide structure along the [110] direction is fabricated using standard photolithography and selective wet etching techniques. To support the narrow, $2 \mu\text{m}$ to $5 \mu\text{m}$ wide, $0.4 \mu\text{m}$ high ridges during the fusion process, $10 \mu\text{m}$ wide InP layers were etched on both sides of the ridges as shown in Figure 4.19. The adjacent ridge waveguides are separated by $125 \mu\text{m}$. After fusion, the sample was thinned to $200 \mu\text{m}$ using an HCl etchant. Then 300 nm gold was deposited on both sides for applying the bias voltage.

Figure 4.20 shows the measured I-V (current vs. voltage) curve of a FVC. The sample size is $3.5 \times 4.5 \text{ mm}^2$. Since 80% of the area of two samples are fused together, and only 3% of this area are the actual ridge waveguide, there is a large

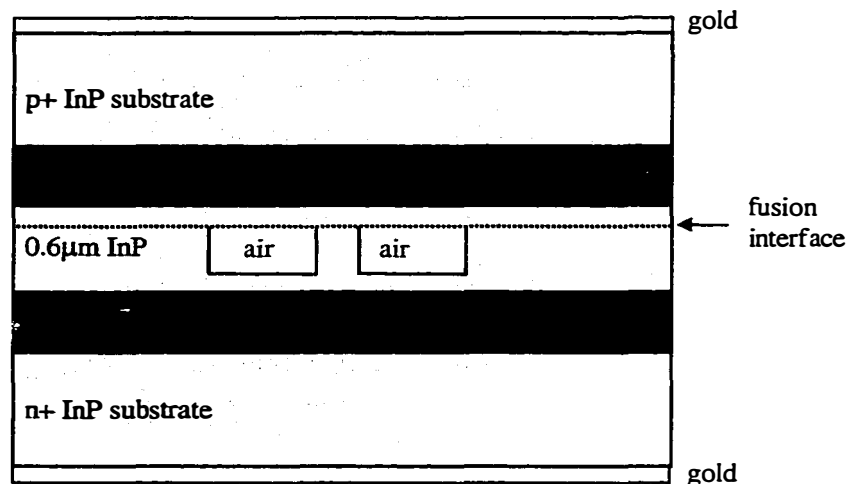


Figure 4.19. Schematic drawing of a fused vertical coupler switch.

leakage current that can be reduced by etching mesas and depositing metal only on the FVC ridge regions (see 4.4.3).

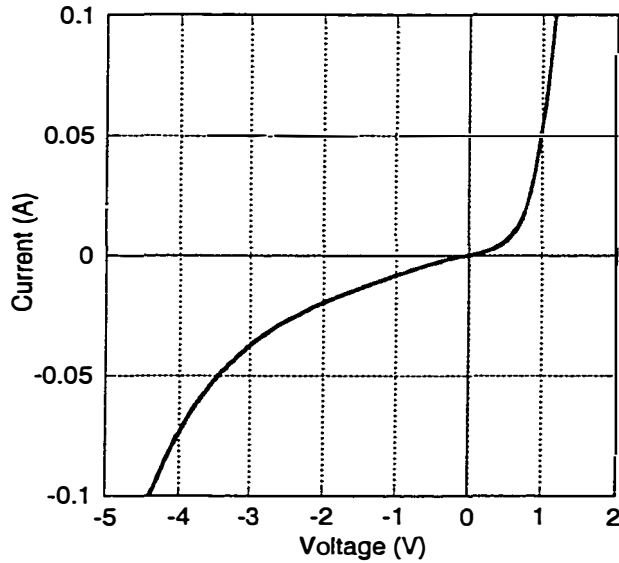


Figure 4.20. I-V curve of broad-area ohmic contact fused vertical couplers

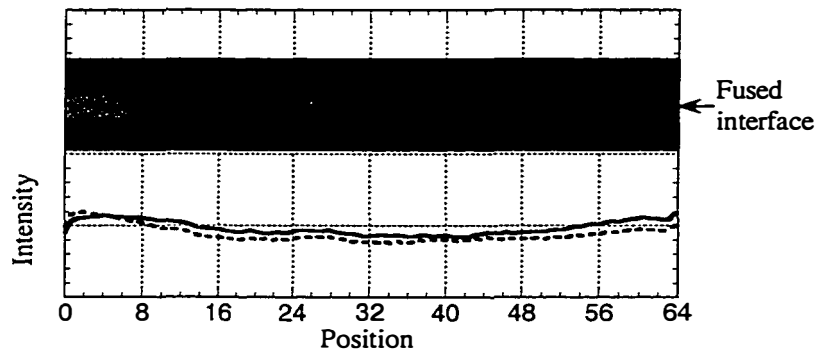


Figure 4.21 Electroluminescence image of 64 μm wide fused area under 200ma current and intensity distribution of upper (dot line) and lower (solid line) guiding layers.

When the wafer bonding technique is used to fabricate VCSELs and detectors, those devices are relatively small and the uniformity of the bonded material is not so critical for individual device operation. Making long waveguide couplers and switches, on the other hand, requires a good uniformity of the

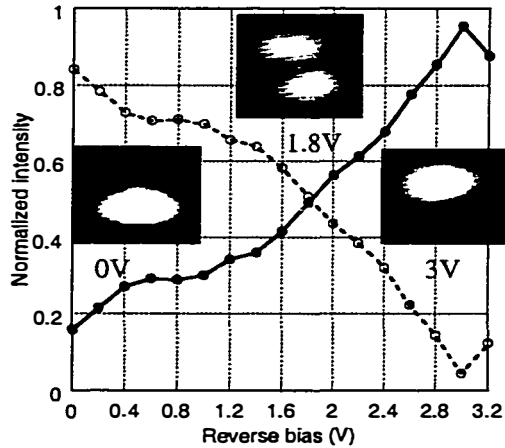


Figure 4.22. Measured intensity of the upper (solid circle) and lower (open circle) waveguides as a function of reverse bias for a broad area ohmic contact FVC.

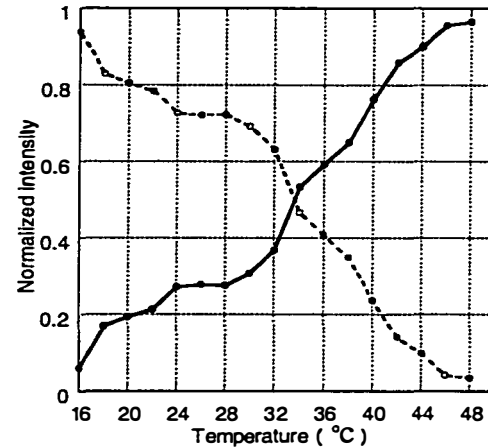


Figure 4.23. Measured intensity of the upper (solid circle) and lower (open circle) waveguides as a function of temperature.

bonding interface. We used electroluminescence images of FVCs to study the bonding uniformity under current flow. The near field pattern at the output facet of the coupler is observed by an IR camera with an 80 \times objective lens. Figure 4.21 shows the luminescence image of the fused area at 200 mA forward current. The image area is 64 μm wide. Luminescence from the two quartanery layers can be clearly distinguished. There are no dark areas and the intensity is very uniform along the fused interface.

To characterize FVCs, a tunable laser is used to launch light at the input of the coupler through an 8 μm diameter single mode fiber. The near field images at the output of a 3.5 mm long FVC for three reverse biases 0V, 1.8V and 3V are shown in Figure 4.22, along with the normalized intensities of upper and lower waveguides. The linear electrooptic effect at 3V is too small to explain the switching. We believe that the thermo-optic effect plays a major role in this device because of the high leakage current which contributes to internal heating of this structure. To confirm this, we changed the stage temperature, and switching was observed with a 30 $^{\circ}\text{C}$ temperature change (see Figure 4.23). To reduce the

thermo-optic effect, we will reduce the leakage current and describe that device in Section 4.4.3.

4.4.3 Push-pull fused vertical coupler switch

As we discussed in Section 4.4.1, push-pull operation is the most efficient way to reduce the driving voltage for optical switch. It is also helpful to reduce the chirping by introducing positive and negative phase shift in two guides. In conventional vertical coupler switches, push-pull operation requires the signs of the electric fields in the upper and lower waveguides to be opposite. This requires the presence of a third electrode between waveguides and application of positive and negative biases to the upper and lower waveguides (see Figure 4.24). Unfortunately, the fabrication of the third electrode in the narrow gap layer is very difficult in conventional vertical couplers.

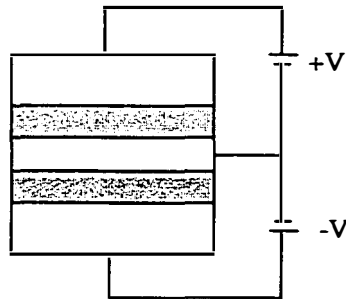


Figure 4.24. Conventional vertical coupler needs the third electrode and two positive and negative biases to realize push-pull operation.

In this section, a single electrode, push-pull fused vertical coupler (FVC) switch using macroscopic crystal inversion symmetry will be demonstrated [24]. The anisotropic linear electrooptic effect in a zinc-blende crystal is used to achieve optical switching under 12 V reverse bias for a 6.9mm long FVC whose two guiding layers have different crystal symmetries. No switching is observed

for the identical structure in which the two guiding layers have the same crystal symmetry.

It is well known that the linear electrooptic effect is anisotropic [25] [26] in zinc-blende crystal structures. When the applied electric field is perpendicular to (001) surface, it gives a positive index change $+\Delta n$ for the TE polarized light propagating along $[110]$ direction and a negative index change $-\Delta n$ for the light propagating along $[\bar{1}\bar{1}0]$ direction. In conventional epitaxial vertical couplers, the upper and lower waveguides have the same crystal orientation (see Figure 4.25 (a)). Consequently push-pull operation requires a third electrode between

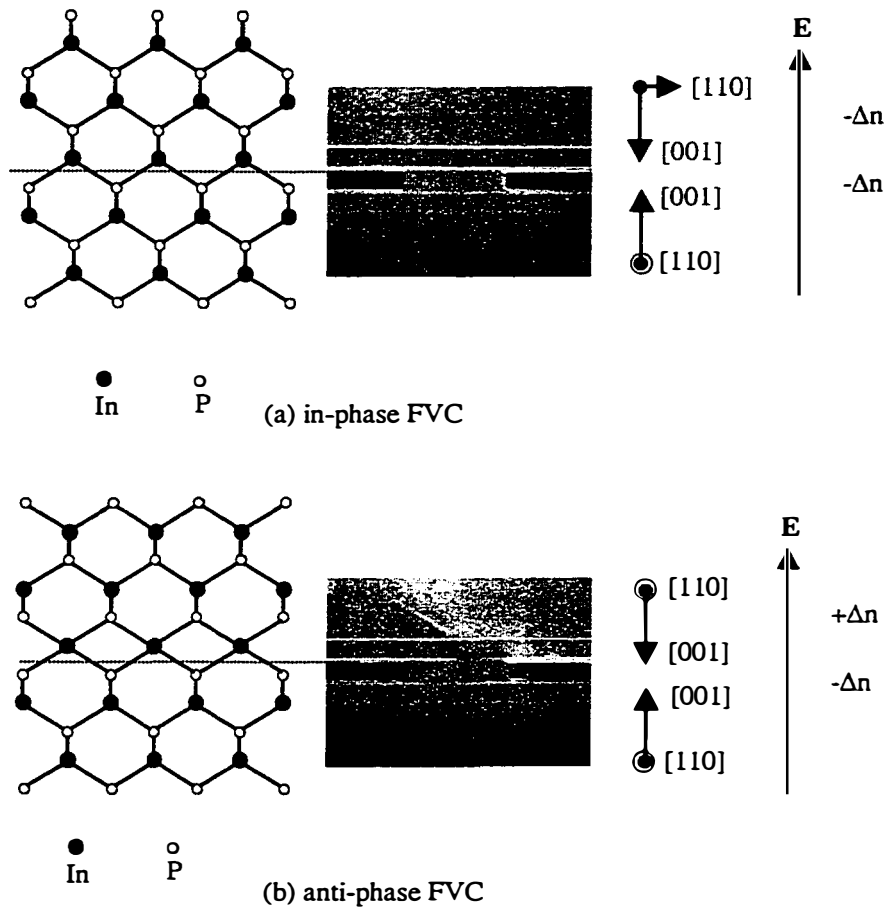


Figure 4.25. SEM pictures and the crystal orientations of (a) in-phase FVC and (b) anti-phase FVC.

waveguides and application of positive and negative biases to the upper and lower waveguides. Since the electrooptic effect is anisotropic, if one of the waveguides in the vertical couplers is along the $[110]$ orientation and the other one along the $[\bar{1}\bar{1}0]$ orientation (see Figure 4.25 (b)), then under an applied bias, the index changes in two waveguides have different signs. This simplifies the electrode fabrication and only requires one electrode for push-pull operation. However, it is impossible to grow the whole vertical coupler structure with two different oriented guiding layers on one substrate, since the crystal structure follows the substrate in epitaxial growth. The only way is to artificially integrate two wafers with various crystallographic orientations. This is a unique feature of wafer fusion.

For (001) InP and GaAs wafers, there are two ways to orient the samples before fusion. One is in-phase fusion [27], which is shown in Figure 4.25 (a), where the $[110]$ axis of the top wafer is perpendicular to the $[110]$ axis of the bottom wafer. This structure is equivalent to that grown by heteroepitaxy. The other one is anti-phase fusion, which is shown in Figure 4.25 (b), where the $[110]$ axes of two wafers are parallel. This structure cannot be realized using epitaxial growth techniques. Macroscopically, the lattice structure of anti-phase fused material has inversion symmetry at the fusion interface. It is obvious that the push-pull vertical coupler switch requires anti-phase fusion so that the applied vertical electrical field induces opposite index change in the two waveguides. Since some of the electrical and optical properties of crystals, as well as their processing characteristics depend on the crystal orientation, wafer fusion gives an extra degree of freedom to fabricate new types of devices. For example, S. Yoo [28] has used wafer fusion to change the crystal orientation periodically to realize quasi phase-matched second-harmonic generation.

For the purpose of comparison, we studied two kinds of FVCs fabricated using in-phase and anti-phase fusion. The schematic structure of the devices is

shown in Figure 4.25. Two wafers were grown using metalorganic chemical vapor deposition (MOCVD). For the first wafer, on a n+ (001) InP substrate, a 0.5 μm InGaAsP ($\lambda_g=1.3 \mu\text{m}$) guiding layer, followed by a 0.1 μm InP cladding layer, a 20 nm InGaAsP ($\lambda_g =1.15 \mu\text{m}$) etch stop layer and a 0.4 μm InP coupling layer were grown. All layers were undoped. The second wafer was grown on a p+ (001) InP substrate. It consists of a 0.2 μm p+ InGaAs layer, followed by a 2 μm p ($5\times 10^{17}/\text{cm}^3$) InP layer and the same intrinsic InGaAsP and InP layers as the first wafer. The last 190nm of the bottom 2 μm InP layer was undoped to avoid Zn diffusion to the quaternary layer during the end of the growth and wafer fusion. The 0.2 μm p+ InGaAs layer was used as an etch stop layer to remove the substrate.

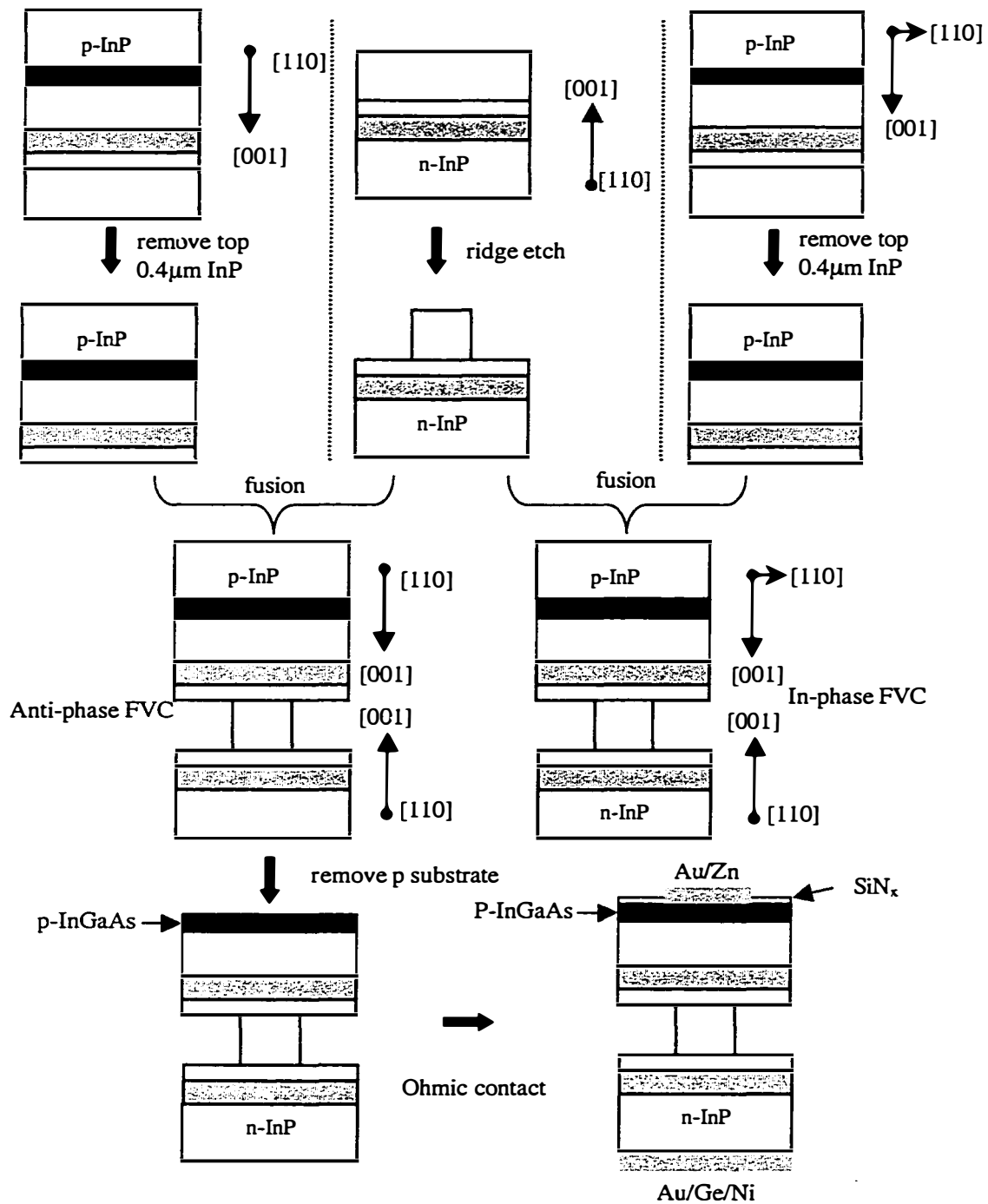


Figure 4.26. The fabrication of in-phase and anti-phase FVCs

The device fabrication starts by cleaving two approximately $8 \times 12 \text{ mm}^2$

samples from each of the grown wafers. The top 0.4 μm InP layer of the p+ samples is removed. On n+ samples, a ridge waveguide structure with 2-3 μm width along the [110] direction is formed using standard photolithography and selective wet etching techniques. The [110] direction was chosen since HCl etchant produces straight side walls in this direction. The n+ and p+ samples are then fused together at a temperature of 630°C in a hydrogen atmosphere for 50 minutes. In one case (fused sample A), the p+ sample was oriented so that its [110] direction was parallel to the waveguides on n+ substrate (i.e., anti-phase fusion). For fused sample B, the orientation of the p+ sample was chosen to get the in-phase fusion. After fusion, p+ InP substrates for both samples are removed using HCl etching. To reduce the leakage current, we first deposit 200 nm thick SiN_x insulation layer on P side, and then open a 3 μm wide window on the exact ridge area with the help of infrared lithography. After that, a 5 μm wide electrode is formed by depositing Au/Zn and lift-off technique. Standard n-type ohmic contacts (Au/Ge/Ni) were formed on the n-InP substrate. The fabrication flow is shown in Figure 4.26. Figure 4.25 shows the stain etched scanning electron microscope (SEM) pictures for both anti-phase (A) and in-phase (B) FVCs.

Figure 4.27 shows the I-V curves of the samples A and B. The device size is about $7\text{mm}\times 3\mu\text{m}$. There is a small forward voltage drop of 1V at the fusion interface. The leakage current of sample A at reverse biases is a little higher than that of sample B. Under forward bias, the luminescence images of anti- and in-phase fused devices are found to be similar as it can be seen in Figure 4.27.

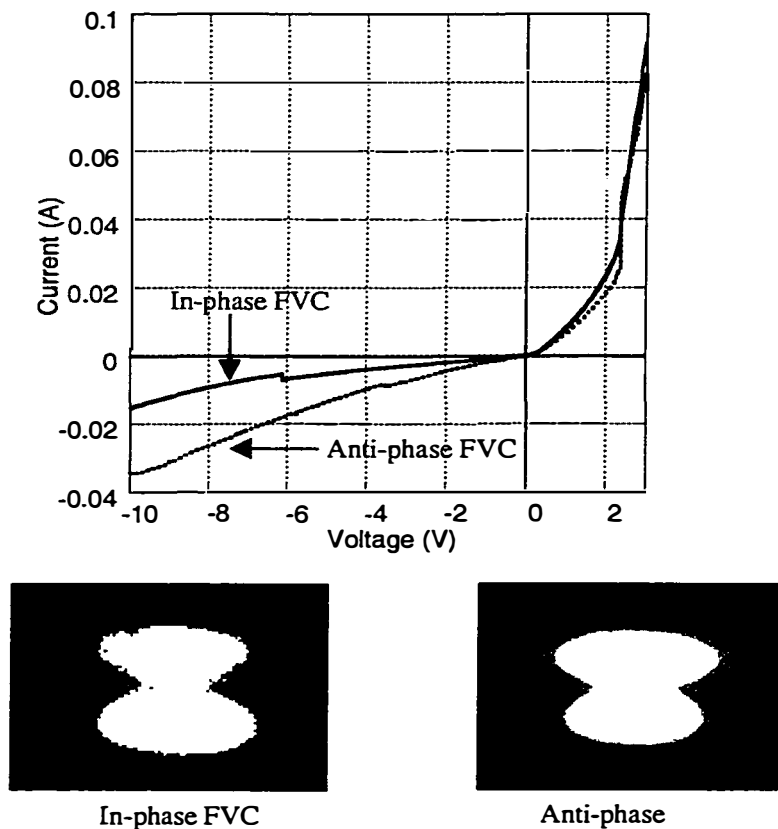


Figure 4.27. I-V curves of in-phase and anti-phase FVC's and the electroluminescence images under 80 mA forward current.

To characterize FVCs, a tunable laser source is used to input TE-polarized light through a lensed single mode fiber. The image at the output of coupler facet is recorded with an IR camera with an $80\times$ objective. The samples are mounted to a temperature stabilized stage. First, the passive switching of the two FVC

structures was characterized by changing the input wavelength as before. In response the effective coupling length changes and the output light switches between the upper and lower waveguides (Figure 4.28). The oscillation period is a function of the coupling strength between two waveguides and the total length of the couplers. The difference in the measured oscillation period of sample A

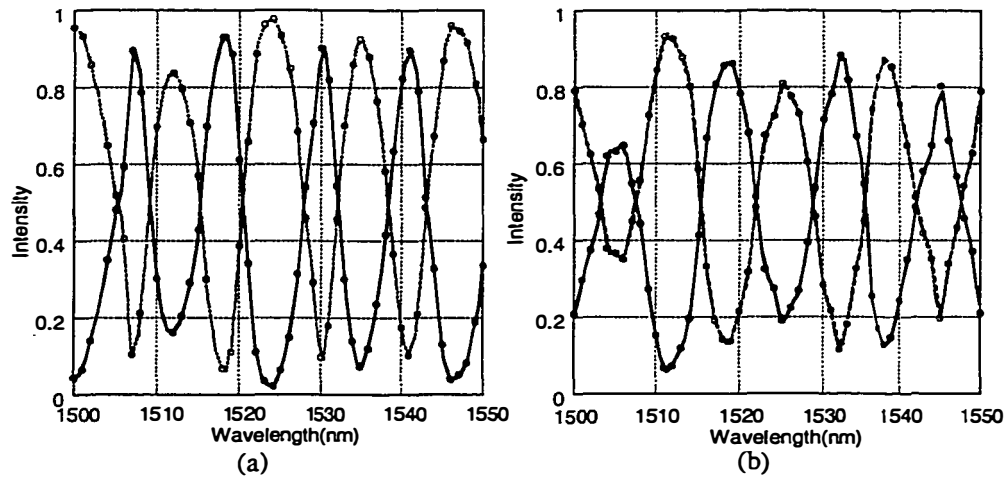


Figure 4.28. The light intensity at the output of upper (solid line) and lower (dash line) waveguides of (a) anti-phase, (b) in-phase FVC's as a function of wavelength.

(11nm) and sample B (13nm) matches very well with the different length of the couplers (sample A: 6.9mm long, sample B: 5.9mm long). This shows that samples A and B have the same coupling length. Then a reverse bias is applied to both samples. The normalized intensities at the output of upper and lower waveguides as a function of bias voltage are shown in Figure 4.29 (a) (sample A) and (b) (sample B). The anti-phase FVC switches at a bias of 12V while no switching is observed for in-phase fused sample B.

It is known that the mechanisms of index change in p-i-n structures include linear electrooptic (LEO) effect, quadratic electrooptic (QEO) effect and free-carrier effect due to the modulation of the depletion layer. In the current

structure, because of a thick $1.6\mu\text{m}$ intrinsic layer and because the operation wavelength is far away from the bandgap, the QEO and free-carrier effects are very weak. Furthermore, QEO and free-carrier effects should be the same for both samples, because they are independent of the crystal orientation. Therefore, the LEO effect dominates in current FVC structures. The switching in sample A is because of the push-pull configuration which comes from the inverted crystal

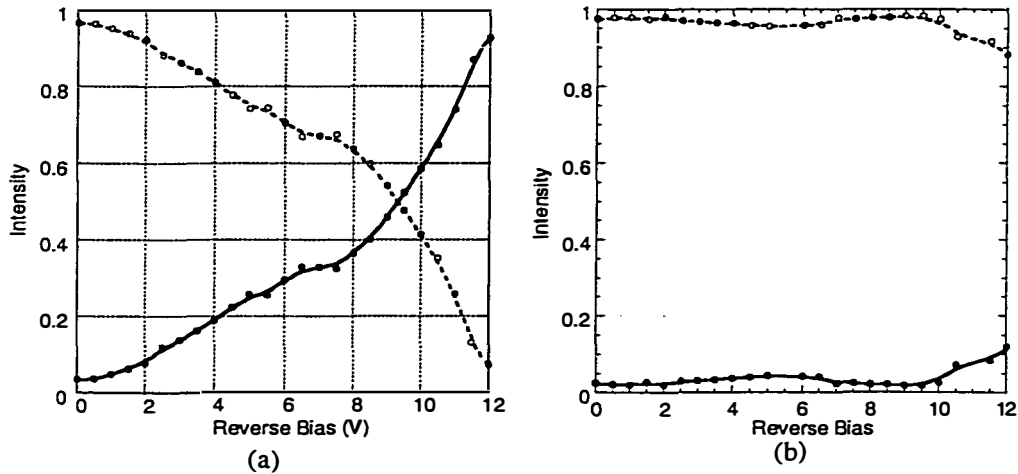


Figure 4.29. The light intensity at the output of upper (solid line) and lower (dash line) waveguides of (a) anti-phase, (b) in-phase FVCs as a function of reverse bias voltage.

orientation. In sample B, the index change in the top and bottom waveguides is the same, so the switching requires a much higher voltage.

4.5 Vertical coupler with separated inputs and outputs

The major obstacle of conventional vertical couplers is how to launch light into two closed waveguides and couple light out to two fibers. Wafer fusion can provide the possibility of separating two input waveguides and output waveguides laterally. Figure 4.30 shows the structure of fused vertical coupler with separated inputs and outputs. For fabrication, first, a set of ridge waveguides on an InP wafer is defined using the usual wet and dry etching techniques. Subsequently, a

wafer is bonded on top of the waveguides. The fusion process is same as before. After removing the substrate of this top wafer using selective etching, a second set of waveguides is fabricated. These top waveguides are coupled vertically to the waveguides beneath them in areas where the two structures are connected by wafer fusion. The issue of alignment in the coupling regions is facilitated using

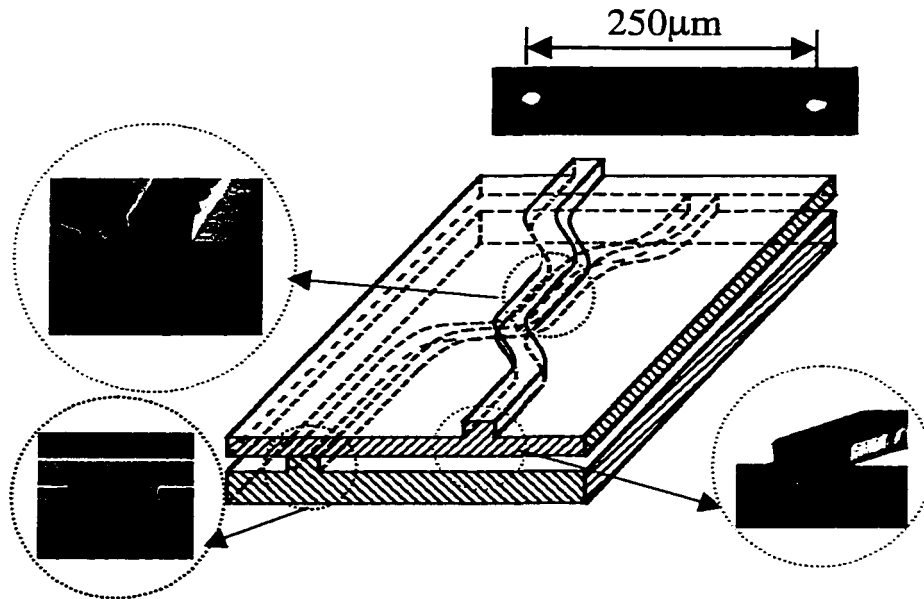


Fig. 4.30 SEM pictures of the separated top and bottom waveguides for an asymmetric fused vertical coupler. The bottom picture is a photograph of the near field pattern at the output of the coupler where the two waveguides are separated by 250 μm.

infrared photolithography. Fig. 4.30 displays the SEM cross section of the bottom and top waveguides along with the near field infrared image at the output of an InGaAsP asymmetric coupler where the two waveguides are separated laterally by 250 μm. By repeating the fusion process, one can obtain multiple layers of waveguide interconnects and realize 3D multilevel photonic integrated circuits.

4.6 Summary of the chapter

In this chapter, we have successfully fabricated wafer fused vertical couplers with a very short coupling length of 62 μm . By inverting the crystal symmetry macroscopically, a push-pull anti-phase fused vertical coupler switch with a 12 V reverse bias switching voltage has been demonstrated. As a comparison, no switching is observed for in-phase FVCs. Finally, the two input waveguides and output waveguides are separated laterally with the help of wafer fusion.

References

- [1] A. N. Miliou, R. Srivastava, and R. V. Ramaswamy, "A 1.3 μm directional coupler polarization splitter by ion exchange," *Journal of Lightwave Technology*, vol. 11, pp. 220-5, 1993.
- [2] R. C. Alferness, L. L. Buhl, U. Koren, B. I. Miller, M. G. Young, T. L. Koch, C. A. Burrus, and G. Raybon, "Broadly tunable InGaAsP/InP buried rib waveguide vertical coupler filter," *Applied Physics Letters*, vol. 60, pp. 980-2, 1992.
- [3] I. Kim, R. C. Alferness, L. L. Buhl, U. Koren, B. I. Miller, M. G. Young, M. A. Newkirk, M. D. Chien, T. L. Koch, G. Raybon, and C. A. Burrus, "InGaAs/InGaAsP MQW optical amplifier integrated with grating-assisted vertical-coupler noise filter," *IEEE Photonics Technology Letters*, vol. 5, pp. 1319-21, 1993.
- [4] C. Wu, C. Rolland, F. Shepherd, C. Larocque, N. Puetz, K. D. Chik, and J. M. Xu, "InGaAsP/InP vertical directional coupler filter with optimally designed wavelength tunability," *IEEE Photonics Technology Letters*, vol. 5, pp. 457-9, 1993.
- [5] H. C. Cheng and R. V. Ramaswamy, "A dual wavelength (1.32-1.56 μm) directional coupler demultiplexer by ion exchange in glass," *IEEE Photonics Technology Letters*, vol. 2, pp. 637-639, 1990.
- [6] H. C. Cheng and R. V. Ramaswamy, "Symmetrical directional coupler as a wavelength multiplexer-demultiplexer: theory and experiment," *IEEE Journal of Quantum Electronics*, vol. 27, pp. 567-74, 1991.
- [7] I. Januar and A. R. Mickelson, "Dual-wavelength ($\lambda = 1300-1650$ nm) directional coupler multiplexer-demultiplexer by the annealed-proton-exchange process in LiNbO₃," *Optics Letters*, vol. 18, pp. 417-19, 1993.

- [8] R. Klein, D. Jestel, H. J. Lilienhof, F. Rottman, E. Voges, Eur. Phys. Soc., Eur. Federation for Appl. Opt., and SPIE, "Integrated-optic wavelength multiplexer in glass fabricated by a charge controlled ion exchange," *Proceedings of the SPIE*, vol. 1011, pp. 46-9, 1989.
- [9] J. P. Lin, R. Hsiao, and S. Thaniyavarn, "Four-channel wavelength division multiplexer on Ti:LiNbO₃," *Electronics Letters*, vol. 25, pp. 1608-9, 1989.
- [10] F. Rottmann, A. Neyer, W. Mevenkamp, and E. Voges, "Integrated-optic wavelength multiplexers on lithium niobate based on two-mode interference," *Journal of Lightwave Technology*, vol. 6, pp. 946-52, 1988.
- [11] T. Aizawa, K. G. Ravikumar, Y. Nagasawa, T. Sekiguchi, and T. Watanabe, "InGaAsP/InP MQW directional coupler switch with small and low-loss bends for fiber-array coupling," *IEEE Photonics Technology Letters*, vol. 6, pp. 709-11, 1994.
- [12] H. Hayashi and K. Tada, "GaAs traveling-wave directional coupler optical modulator/switch," *Applied Physics Letters*, vol. 57, pp. 227-8, 1990.
- [13] M. N. Khan, W. Yang, and A. Gopinath, "Directional coupler electro-optic modulator in AlGaAs/GaAs with low voltage-length product," *Applied Physics Letters*, vol. 62, pp. 2033-5, 1993.
- [14] F. Dollinger, M. V. Borcke, G. Bohm, G. Trankle, and G. Weimann, "Ultrashort low-loss optical multiquantum-well GaAs/GaAlAs vertical directional coupler switch," *Electronics Letters*, vol. 32, pp. 1509-10, 1996.
- [15] K. Tada, K. Hirose, and Japan Soc. Applied Phys, "A new light modulator using perturbation of synchronism between two coupled guides," presented at 6th Conference on Solid State Devices, Tokyo, 1974.
- [16] M. Cada, B. P. Keyworth, J. M. Glinski, C. Rolland, A. J. Spring Thorpe, K. O. Hill, and R. A. Soref, "Electro-optical switching in a GaAs multiple

- quantum well directional coupler,” *Applied Physics Letters*, vol. 54, pp. 2509-11, 1989.
- [17] J. A. Cavailles, M. Erman, and K. Woodbridge, “Experimental study of switching in a p-i(MQW)-n vertical coupler,” *IEEE Photonics Technology Letters*, vol. 1, pp. 373-5, 1989.
- [18] M. Kohtoku, S. Baba, S. Arai, and Y. Suematsu, “Switching operation in a GaInAs-InP MQW integrated-twin-guide (ITG) optical switch,” *IEEE Photonics Technol. Lett.*, vol. 3, pp. 225-6, 1991.
- [19] B. Boche, R. Muller, G. Bohm, G. Trankle, and G. Weimann, “Monolithic integration of GaAs-AlGaAs quantum-well lasers with directional couplers using vertical coupling of light,” *IEEE Photonics Technology Letters*, vol. 8, pp. 1591-3, 1996.
- [20] L. Bin, A. Shakouri, P. Abraham, K. Boo-Gyoun, A. W. Jackson, and J. E. Bowers, “Fused vertical couplers,” *Applied Physics Letters*, vol. 72, pp. 2637-8, 1998.
- [21] Ş. Ikuta, S. Kubota, W. Pan, S. T. Chu, and Y. Kokubun, “Stacked ARROW vertical coupler with large tolerance and short coupling length for three-dimensional interconnects,” *Electronics Letters*, vol. 34, pp. 1851-2, 1998.
- [22] H. Kogelnik and R. V. Schmidt, “Switched directional couplers with alternating Delta beta,” *IEEE Journal of Quantum Electronics*, vol. 12, pp. 396-401, 1976.
- [23] M. K. Chin, “Design considerations for vertical delta k directional coupler,” *Journal of Lightwave Technology*, vol. 11, pp. 1331-6, 1993.
- [24] B. Liu, A. Shakouri, P. Abraham, and J. E. Bowers, “Push-pull fused vertical coupler switch,” *IEEE Photonics Technology Letters*, vol. 11, pp. 662-4, 1999.

- [25] H. G. Bach, J. Krauser, H. P. Nolting, R. A. Logan, and F. K. Reinhart, "Electro-optical light modulation in InGaAsP/InP double heterostructure diodes," *Applied Physics Letters*, vol. 42, pp. 692-4, 1983.
- [26] A. Yariv, *Quantum Electronics*, Second Edition ed.
- [27] Y. Okuno, K. Uomi, M. Aoki, T. Taniwatari, M. Suzuki, and M. Kondow, "Anti-phase direct bonding and its application to the fabrication of InP-based 1.55 μm wavelength lasers on GaAs substrates," *Applied Physics Letters*, vol. 66, pp. 451-3, 1995.
- [28] S. J. B. Yoo, R. Bhat, C. Caneau, and M. A. Koza, "Quasi-phase-matched second-harmonic generation in AlGaAs waveguides with periodic domain inversion achieved by wafer-bonding," *Applied Physics Letters*, vol. 66, pp. 3410-12, 1995.

Chapter 5

Vertical Coupler based Wavelength multiplexers

5.1 Introduction

In WDM transmission systems, wavelength multiplexers and demultiplexers (MUX/DEMUX) are the essential components employed to combine and separate a number of optical streams at distinct wavelengths carrying different information. The realization of MUX/DEMUX's has been accomplished by using wavelength dispersive elements like optical interference filters, optical diffraction gratings, and wavelength selective coupling between two adjacent waveguides. Four competing approaches are now commercially available: Dichroic Interference Filters (DIF)[1], Fiber Bragg Gratings (FBG)[2], Array Waveguide Filters (AWG) [3, 4] and Cascaded Mach-Zehnder (M-Z) interferometers [5, 6].

DIF, sometimes referred to as thin-film quarter-wavelength filters, represent a mature technology. DIF technology uses layers of dielectric thin films coated on a glass substrate to combine or separate specific wavelengths in a WDM system. By controlling the deposition layers on the substrate, different types of interference effects can be created to produce narrowband, wideband and gain-flattening filters.

Fiber Bragg gratings are all-fiber components that are capable of performing as wavelength selective filters [7-9]. Fabrication of these devices is based on the inherent photosensitivity of conventional germanium-doped silica fibers. By using a pair of ultraviolet beams or a phase mask, a permanent periodic variation in the refractive index is created in the fiber. When light with a wavelength satisfying the Bragg condition is launched to the fiber grating, the

energy is reflected and all others wavelengths pass through the grating with negligible insertion loss and no change in signal. A fiber Bragg grating is used in a DWDM device because it is compact, easy to couple to the fiber and polarization insensitive. However, it is less stable mechanically and, because of the design, it has a high back reflection. Additional costs must be incurred because optical circulators and isolators are needed to fulfill the functions of (de)multiplexing and add/drop.

The planar Array Waveguide Grating (AWG) [4, 10, 11] is a highly versatile passive WDM device, which can function as a multiplexer, a demultiplexer, an add/drop element, or a wavelength router. It consists of two passive star couplers connected by grating array waveguides. The lengths of adjacent waveguides in the central region differ by a constant value. Because of the phase difference, the signals with different wavelengths will constructively recombine at different output ports. The fabrication of AWG is in much the same way that electronics are integrated on to ICs, or chips. The manufacturing volume/cost benefits that accrue to the AWGs make these devices very cost-effective when the channel-counts are over 40.

A fused cascaded fiber (FCF) hybrid filter combines unbalanced Mach-Zehnder interferometer structures in the front end and fused biconic taper couplers for the back end. An in-line narrow-band filter is used to clean up the signal at the end of the cascade. The technology can be used to multiplex wavelengths on optical fibers and is especially well suited for the metro and access markets. The unbalanced M-Z approach uses cascaded couplers to increase channel and port counts. This method achieves dense channel spacing by increasing the difference of geometrical lengths of the interferometer arms while maintaining identical propagation constants. The optical path difference between the two arms results in a sinusoidal wavelength response with a very small polarization dependence, because the couplers themselves are very short. A single

coupler will multiplex two wavelengths, and several must be combined for greater numbers, resulting in a continuously branching tree structure. At each stage, the wavelength spacing between channels in a given fiber is twice that in the previous stage. The increase in channel spacing makes high isolation easy to achieve.

In this chapter, a new WDM multiplexer/demultiplexer based on cascaded vertical couplers will be proposed and demonstrated. Although multiplexers based on directional couplers have been studied for a long time, they are applicable only to the case where the channel spacing is quite large (e.g. 980nm and 1550nm or 1300nm and 1550nm) [12]. This is because of the weak wavelength dependence of the coupling coefficient in horizontally arranged directional couplers. Otherwise a very long device length is required. Compared to horizontal couplers, vertical couplers offer much stronger coupling since the thickness of the guiding layer and the space between two waveguides can be very small and precisely determined by the epitaxial growth [13, 14]. The multi-channel multiplexers with narrow channel spacing can be achieved by cascading several strongly coupled vertical couplers. However, separating the two input and output waveguides in conventional vertically coupled twin waveguide structures is difficult. This limits practical applications and makes the cascading of several vertical couplers impossible. In this work, this problem is solved using double-sided epitaxial layer processing by wafer bonding.

We start this chapter by using coupled mode theory and normal mode theory to analyze and design the MUX/DEMUX in Section 2. Double-sided wafer processing will be described in Section 3. The experimental results of two-, four- and eight-channel wavelength multiplexers will be given in Section 4. In Section 5, we will discuss the wavelength selective switch.

5.2 Design of vertical coupler multiplexer

5.2.1 Operation principle of coupler based MUX/DEMUX

The schematic drawing in Figure 5.1 shows a 2-channel multiplexer, which consists of a symmetric directional coupler formed by two identical waveguides. Each waveguide is single mode and the center coupler supports two

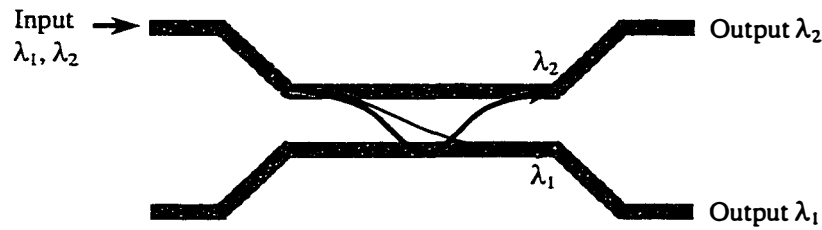


Figure 5.1. Configuration of two-channel wavelength multiplexer based on symmetrical directional coupler

normal modes (supermodes): symmetric (even) and anti-symmetric (odd) modes. Assuming that the single mode input and output waveguides are coupled adiabatically to the center coupling region, and both input and output guides are well separated, the symmetric and anti-symmetric excitation amplitudes will be nearly identical ($\eta_e = \eta_o = \frac{1}{\sqrt{2}}$). Based on normal mode theory (see 2.4.2 and

2.6.2), the output of bar and cross states are given by Equations (2.17) and (2.18):

$$P_{//}(z) = \cos^2\left(\frac{\phi}{2}\right) \quad (5.1)$$

$$P_{\times}(z) = \sin^2\left(\frac{\phi}{2}\right) \quad (5.2)$$

Where ϕ is the total accumulated relative propagation phase difference between two normal modes and the input power is 1. Generally, the phase difference is wavelength dependent. If $\phi(\lambda_1) - \phi(\lambda_2) = \pi$, then the two wavelengths can be

separated to different outputs. Therefore the basic principle of the coupler based MUX/DEMUX is two mode interference.

For a straight coupler, the phase difference ϕ between two supermodes can be expressed as

$$\phi = \frac{2\pi}{\lambda} \Delta n \cdot L \quad (5.3)$$

where $\Delta n = n_e - n_o$ is the effective index difference between even and odd supermodes; L is the coupler length. As we will see in Figure 5.2, the wavelength dependence of the effective index difference Δn can be approximated by

$$\Delta n = -a + b\lambda \quad (5.4)$$

where a and b are constants depending on the coupler structure.

By substituting Equation (5.4) into Equations (5.1) and (5.2), we will find the outputs are periodic functions of wavelength. The wavelength period $\Delta\lambda_p$ can be easily found:

$$\Delta\lambda_p = \frac{\lambda^2}{aL} \quad (5.5)$$

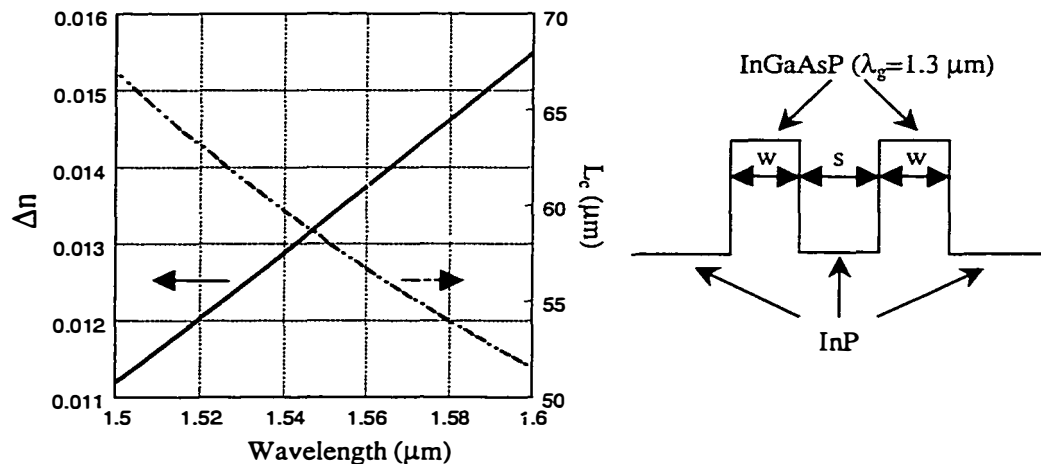


Figure 5.2. The effective index difference Δn and the coupling length as a function of wavelength. $s=0.6 \mu\text{m}$.

and the channel spacing $\Delta\lambda_s$ is half of the period.

$$\Delta\lambda_s = \frac{\lambda^2}{2aL} \quad (5.6)$$

Therefore the period is determined by the coupler length and the parameter **a**, which reflects the wavelength dependence of the coupling strength.

5.2.2 Wavelength dependence of vertical coupler

We first study the wavelength dependence of different directional couplers. We saw in Figure 5.2 the calculated effective index difference Δn between even and odd supermodes of a 2D vertical coupler as a function of wavelength, which can be expressed as a linear relationship of λ : $\Delta n = -a + b\lambda$. The parameter **a** depends on the coupler structure.

To get a small channel spacing and reduce the coupler length, a large **a** is needed. Contrary to our intuition, parameter **a** doesn't always increase with the decrease of the coupling length when the coupling length becomes very short. Figure 5.3 shows the calculated **a**, **b** and the coupling length of a 2D vertical coupler as a function of the separation *s*. There is a maximum **a**, and the corresponding coupling length is about 19 μm . As the coupling length further decreases, the parameter **a** at one point can equal zero, which means that there is no wavelength dependence at this point. This phenomenon is confirmed by beam propagation simulation. The index and the thickness of guiding layers will also affect the wavelength dependence. Figure 5.4 and 5.5 are the calculated curves of **a** as functions of the index change and the thickness of the guiding layers. There is always a maximum value of **a**. Therefore we should carefully choose the coupler structure to optimize the wavelength dependence for the applications of wavelength multiplexers.

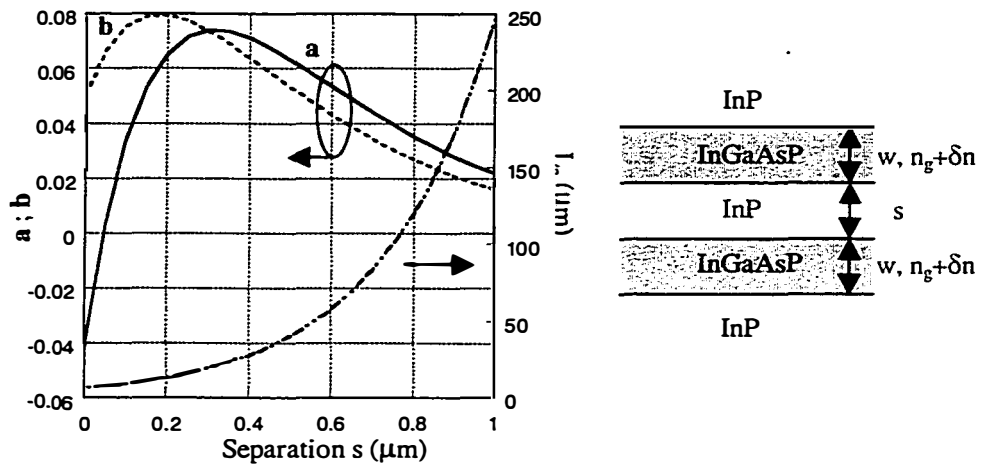


Figure 5.3. The parameters **a**, **b** and the coupling length L_c as a function of the separation s between two guiding layers.

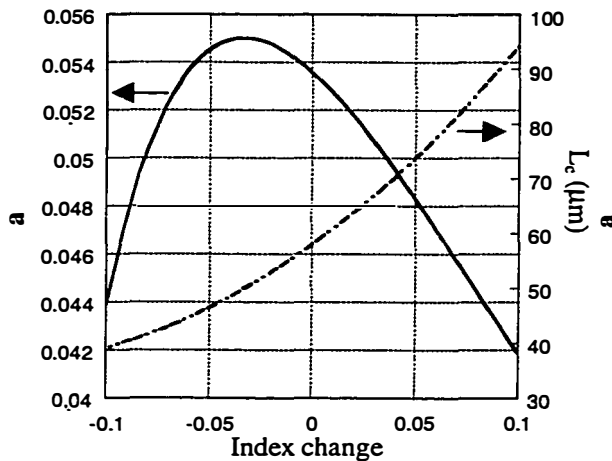


Figure 5.4. The parameter **a** and the coupling length L_c as a function of the index change δn of the guiding layers.

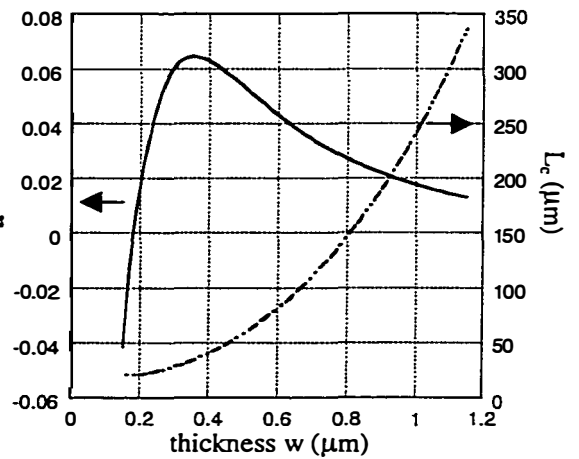


Figure 5.5. The parameter **a** and the coupling length L_c as a function of the thickness w of the guiding layers.

To see how strong the wavelength dependence of the vertical couplers is, we calculated the parameter **a** of a horizontal coupler. Figure 5.6 shows **a** and the coupling length as a function of the separation s between two waveguides in a horizontal coupler (see the right of Figure 5.6). Compared to Figure 5.3, the

wavelength dependence of horizontal couplers is much smaller than that of vertical couplers. Figure 5.7 shows the parameter a as a function of the width of the waveguides for separation $s=0$. The maximum a is only 0.02 when $w=1.2 \mu\text{m}$

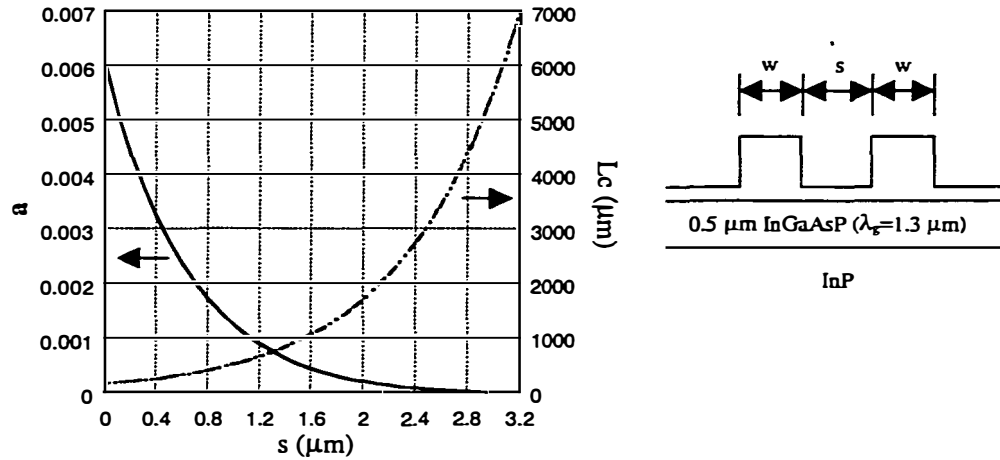


Figure 5.6. The parameter a and the coupling length L_c as a function of the separation s of two waveguides.

(when $w < 1.2 \mu\text{m}$, there is only one mode in this coupler) and the coupling length is about $67 \mu\text{m}$. The vertical coupler with the same coupling length has an $a > 0.5$. To achieve the same channel spacing, the vertical coupler based wavelength multiplexers will be much shorter than the horizontal coupler based ones, and it makes the cascading several stages of vertical coupler to realize multiple wavelength multiplexer reasonable.

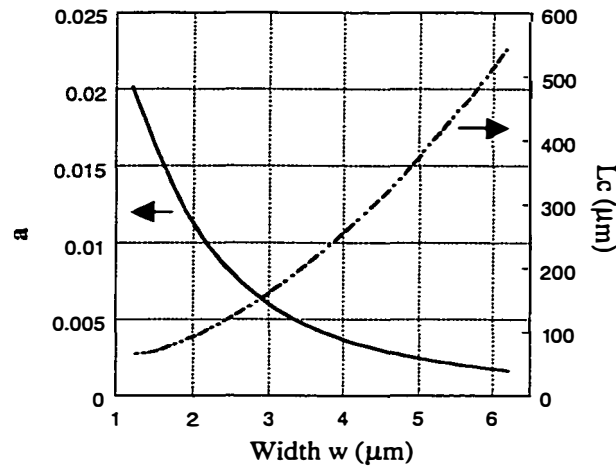


Figure 5.7. The parameter a and the coupling length L_c as a function of the width w of two waveguides.

5.2.3 Multiple channel wavelength multiplexers

A multiple channel multiplexer can be constructed by cascading dual-channel MUX/DEMUX with proper parameters. As an example of multi-channel MUX/DEMUX design, an eight-channel MUX/DEMUX shown in Figure 5.8 is considered. From Equation (5.6) in 5.2.1, the channel spacing is inversely proportional to the coupler length. So the channels separation of the coupler VC21 in stage 2 is twice that of coupler in stage 1, if the stage 1 coupler VC1 is two times longer than that of stage 2 coupler VC21. For proper operation of this structure, the channels of VC21 and VC22 should lie on the successive channel of VC1 as shown in Figure 5.9. So VC3 has nearly the same wavelength period as VC2, but the peaks in the output should be shifted by a quarter period to match the channels. This can be achieved by a small adjustment to the length of VC22. Figure 5.10 shows the simulated transmission spectra of an 8-channel MUX/DEMUX with and without the phase shift, where the structure of the vertical coupler is the same as the one discussed in the last section, and the length of first stage is 5 mm. To match the channel, the lengths of each vertical coupler

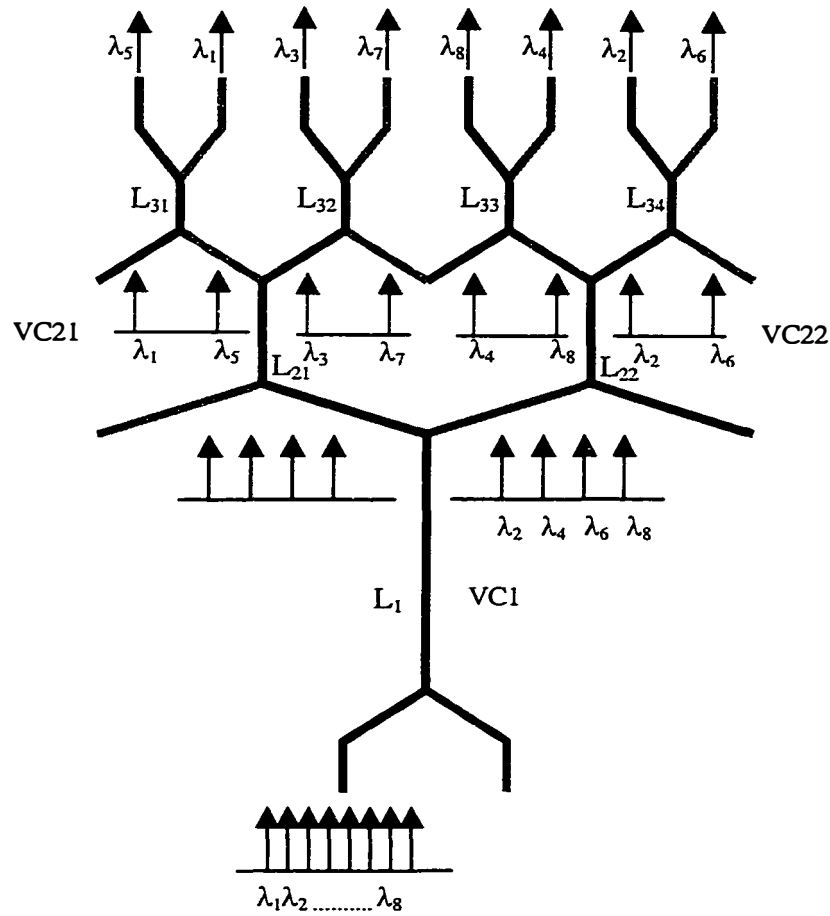


Figure 5.8. Configuration of 8-channel MUX/DEMUX.

are chosen: $L_{21} = \frac{L_1}{2} = L_{22} + \frac{L_c}{2}$ and $L_{32} = \frac{L_{21}}{2} = L_{31} - \frac{L_c}{2} = L_{33} + \frac{L_c}{4} = L_{34} - \frac{L_c}{4}$.

L_c is the coupling length at $1.55 \mu\text{m}$. Since the coupler length is wavelength dependent, this choice will introduce a certain crosstalk at other wavelengths. Figure 5.11 shows the calculated extinction ratio of the output at the second stage as a function of the coupler length difference between two couplers. When $L_{21} - L_{22}$ corresponds to odd multiples of a quarter of π phase shift, we have the highest extinction ratio. In an ideal coupler, we have a relatively large window of about

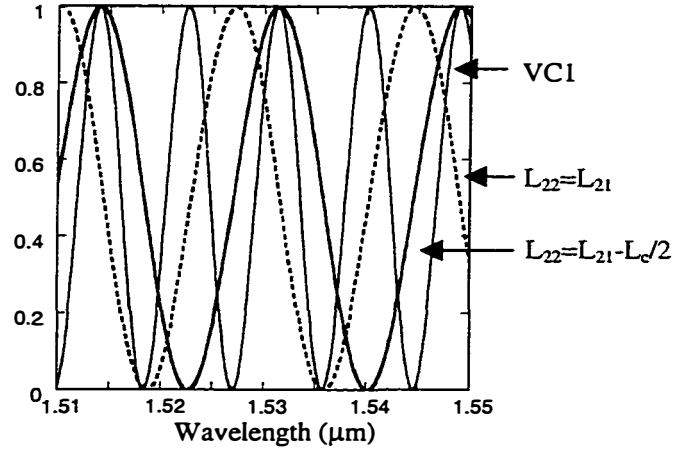


Figure 5.9. The transmission characteristic of VC22 must be shifted a quarter period to match the channels.

10 μm to get crosstalk $< 30\text{dB}$. We also note that as the phase shift increases, the two channels will be switched. Therefore a wavelength selective switch can also be realized. We will discuss this more in Section 5.5.

The overall length of coupler based 2^N channel MUX/DEMUX can be expressed as

$$L_t = \sum_{n=0}^{N-1} \frac{L_s}{2^n} + \sum_{n=0}^{N-1} \frac{L_0}{2^n} + L_e \quad (5.7)$$

where L_s is the length of s-bend for input and output separation in the first stage coupler, L_0 is the length of the first stage coupler, and L_e is the extra length for phase shifting. When $N \rightarrow \infty$,

$$L_t = 2L_s + 2L_0 + L_e \quad (5.8)$$

We can see the total length will be limited by the s-bends as the number of channel increases, because $L_s \gg L_0$ when N is a large number.

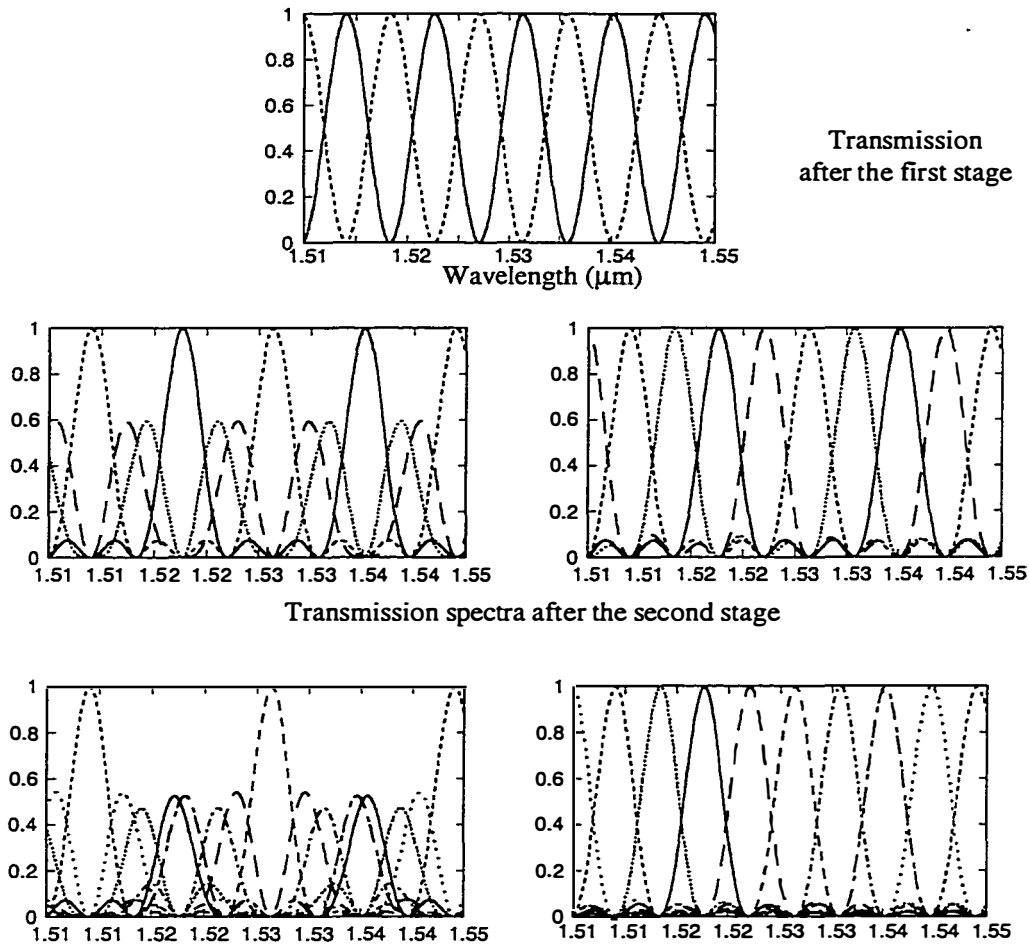


Figure 5.10. Transmission spectra of an 8-channel MUX/DEMUX. after the third stage. Left: without phase shift. Right: with phase shift.

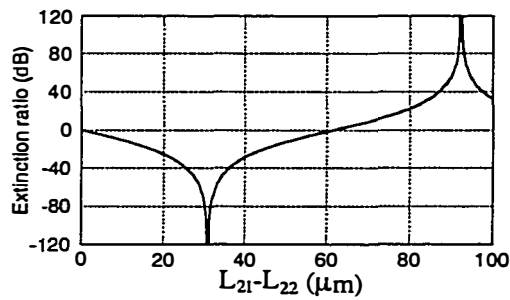


Figure 5.11. Extinction ratio as a function of the coupler length difference between VC21 and VC23.

5.3 Double-sided wafer processing

In this section, we will briefly introduce a technology which enables us to fabricate vertical coupler based wavelength multiplexers. We called it double-sided wafer processing: both frontside and backside processing of the *same* substrate. Using wafer bonding, a conventionally processed epitaxial layer structure (Figure 5.12 (a)) is inverted and bonded to a new host substrate (Figure

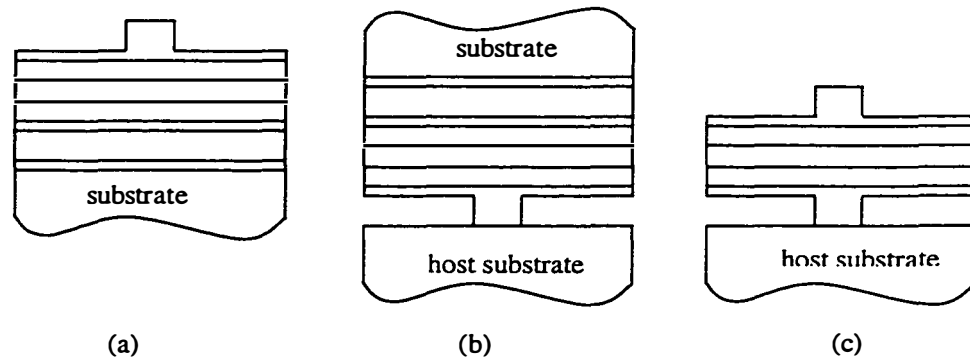


Figure 5.12. (a) The conventional processed epitaxial layer structure.
 (b) The epitaxial structure has been inverted and bonded to another host substrate.
 (c) After removing the original substrate, another side of the epitaxial structure can be processed

5.12. (b)). After removing the top substrate and leaving only the thin epitaxial film bonded to the host material, the exposed backside of the epitaxial structure can then be processed as well (Figure 5.12. (c)). This technique enables fabrication of 3D photonic integrated circuits.

In optoelectronic circuits, increasing integration density is a key factor to reduce cost and improve performance. In conventional wafer processing, only one side of epi-films is used to fabricate photonic integrated circuits. If both sides of the epitaxial layers can be processed as discussed above, three-dimensional structures can be fabricated and the integration density can be considerably increased. Since epitaxial layers by themselves are too thin to handle and process

directly, they must be transferred and bonded to other host substrates. For optoelectronic device applications, the bonded interface must be both electronically and optically transparent to make multi-level electrical and optical interconnects possible. The requirement for optical transparency means that conventional bonding techniques such as flip-chip solder bonding are not suitable for photonic integration. Wafer bonding, on the other hand, provides an interface with low electrical and optical loss and is suitable for this application. Wafer bonding based double-sided processing is the key enabling technique for the fabrication of wavelength multiplexers and optical add/drop multiplexers in this and next chapter.

In the fused vertical couplers discussed in Chapter 4, the fused interface was between the two guiding layers. This introduced an excess optical loss due to imperfection at non-epitaxial interface. In order to separate the input and output waveguides, it was necessary to align the two wafers with submicron resolution during the wafer bonding process. In our current work, **the fused interface is not important since it is far away from the guiding layer. Also no alignment is necessary during the bonding process.**

It is worthy to notice that processing both sides through the wafer bonding technique needs only one epi-wafer and the other host wafer can be any materials, such as Si, glass, etc. This will reduce the cost and give us more flexibility for the fabrication of 3D photonic integrated circuits.

5.4 Multi-channel wavelength multiplexers

5.4.1 Fabrication of 3D vertical couplers

The schematic drawing in Figure 5.13 shows a vertical coupler with separated inputs and outputs, where the two waveguides are coupled vertically and separated horizontally in different planes. The epitaxial structure is grown using

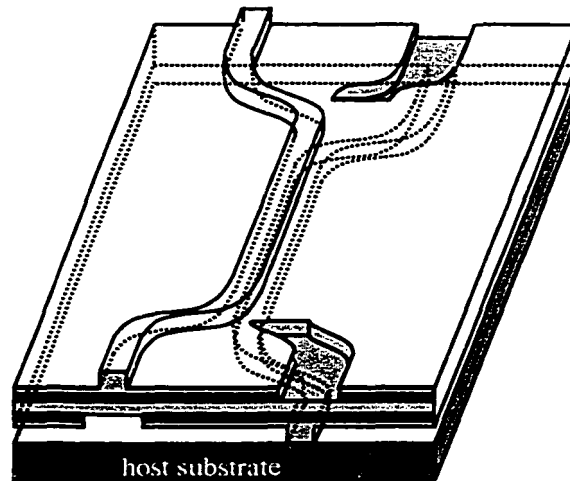


Figure 5.13. The schematic drawing of a vertical coupler with separated inputs and outputs.

metal organic chemical vapor deposition (MOCVD). It includes a $0.8\mu\text{m}$ InP frontside ridge layer, a 15nm InGaAsP (bandgap $1.1\mu\text{m}$) etch stop layer, a $0.2\mu\text{m}$ InP cap layer for the first generation devices and a $0.1\mu\text{m}$ InP layer for the second generation MUX/DEMUX, a $0.5\mu\text{m}$ InGaAsP (bandgap $1.3\mu\text{m}$) frontside guiding layer, a $0.6\mu\text{m}$ InP coupling layer, the same backside guiding, cap, etch stop and ridge layers, and finally a $0.2\mu\text{m}$ InGaAs layer used to remove the InP substrate.

The fabrication sequence is shown in Figure 5.14. (1) First, the $3\mu\text{m}$ width frontside ridge waveguides are formed by MHA ($\text{CH}_4/\text{H}_2/\text{Ar}$) reactive ion etching (RIE) and chemical wet etching. (2) The frontside guiding layer above the backside waveguides in non-coupling areas is removed by another step of photolithography and wet etching. (3) The waveguide sample is inverted and bonded to a bare InP host substrate under pressure for 50 minutes at 630°C in H_2

atmosphere. (4) The original InP substrate and InGaAs etch stop layer are removed by selective etching. (5) The other side waveguides are fabricated. To

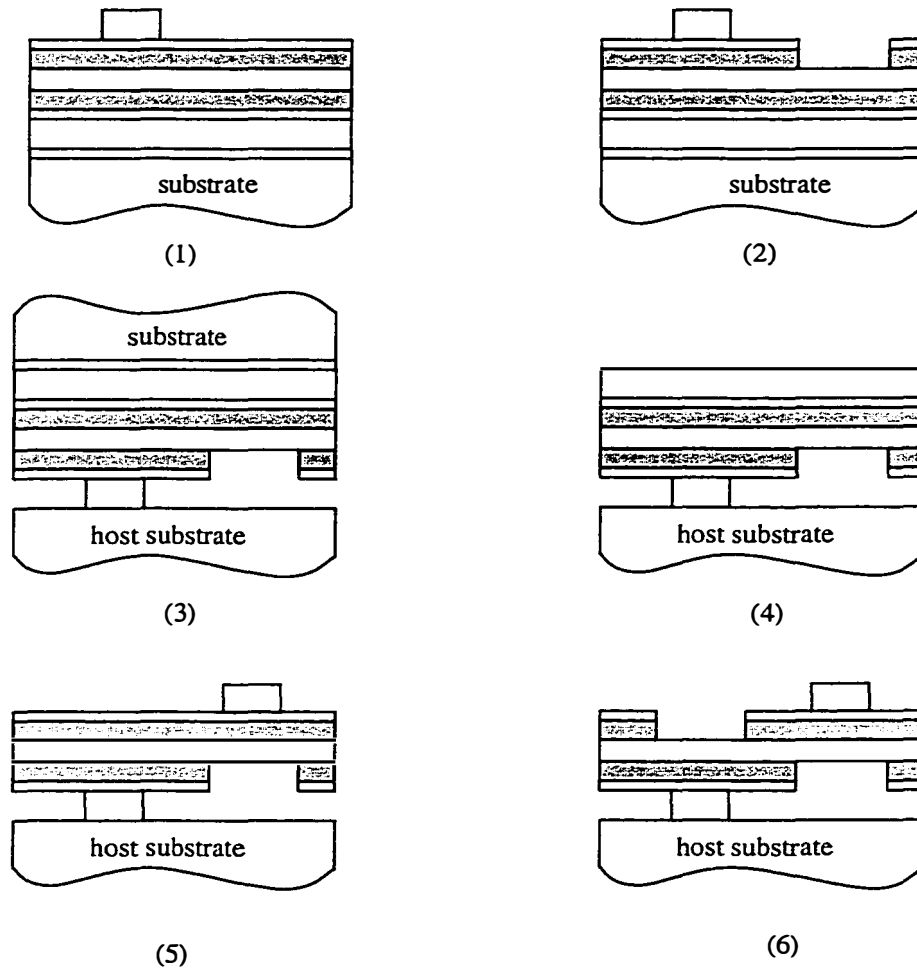


Figure 5.14. The fabrication sequence of 3D vertical couplers.

align the upper layer waveguides with the lower layer ones, infrared photolithography is needed. But there is a certain alignment error. A better approach is to first open a window to expose the alignment marks with the help of infrared aligner, then aligning two layer waveguides as usual. (6) Finally the unneeded guiding layers are removed as before. The transferred and bonded thin

epitaxial film is robust and it is processed using the same techniques as other planar photonic integrated circuits.

5.4.2 Wavelength multiplexers without phase shift

The first generation of vertical coupler based wavelength multiplexers didn't

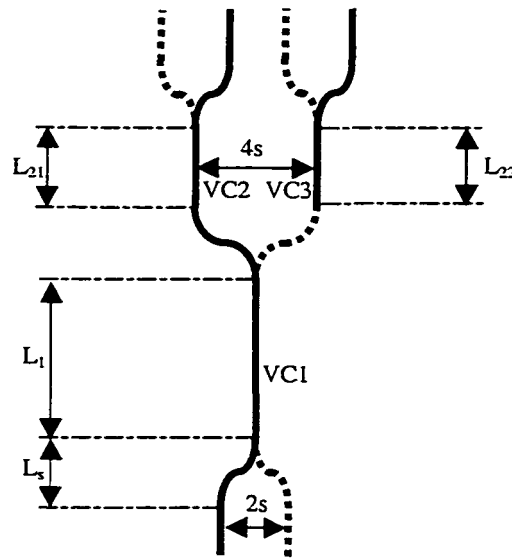


Figure 5.15. The schematic drawing of a 4-channel multiplexer, where $L_{21}=L_{22}$ and no two dummy s-bends in the second stage, which introduce a certain asymmetry.

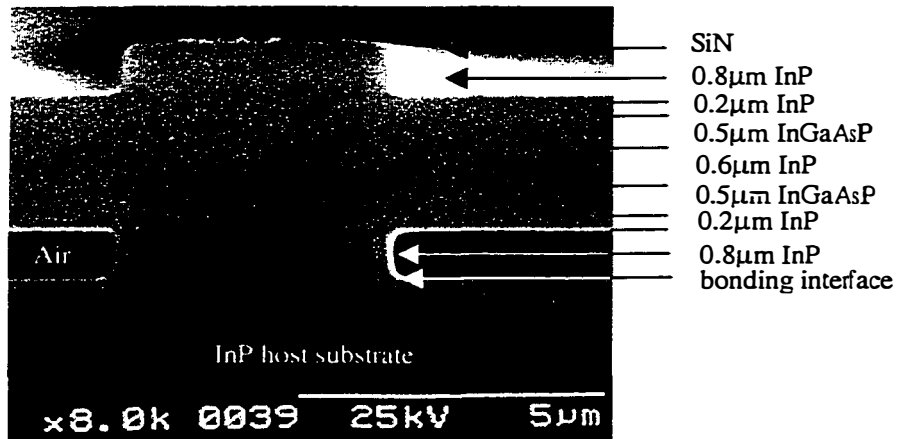


Figure 5.16. SEM picture of a vertical coupler fused to an InP substrate.

incorporate the phase shift region to match the channel peaks and the dummy s-bends. Figure 5.15 shows a 4-channel MUX/DEMUX, where $L_{21}=L_{22}$. The absence of two sbends in the second stage will introduce asymmetry in the coupler and reduce the extinction ratio.

Figure 5.16 shows The SEM picture in the coupling region. In order to characterize the device performance, light from a tunable laser was coupled to an input waveguide by a single mode fiber. The light at the output was collected by another single mode fiber, which was connected to a detector. The near field images were recorded by an IR camera with a 20× lens. Figure 5.17 shows the measured output light intensity as a function of wavelength for a dual-channel MUX/DEMUX. The total device length is 8mm, the coupler length is 4mm and the separation between two waveguides is 20 μm . As we expected, the output intensity is a periodic function of wavelength and the oscillation period is about

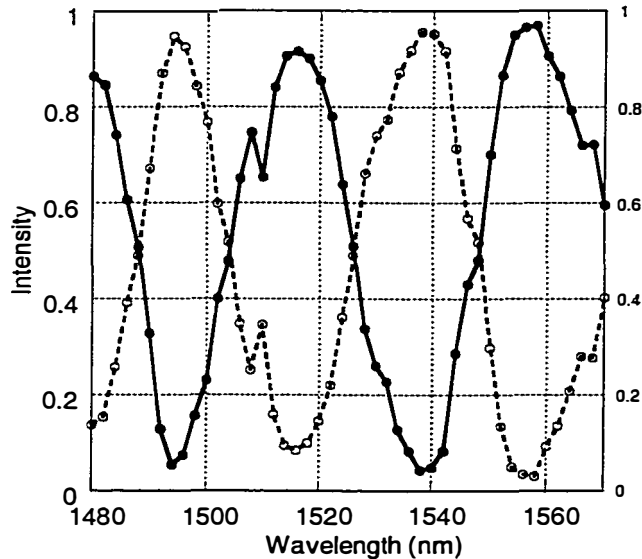


Figure 5.17. The normalized output of two waveguides as a function of wavelength.

40nm. This means that the device can be used as a wavelength multiplexer/demultiplexer for 20nm wavelength spacing. This small wavelength

spacing is very difficult to achieve in conventional horizontally arranged coupler because of the weak wavelength dependence of the coupling coefficient.

We also fabricated 4 and 8-channel MUX/DEMUX on the same chip. Figure 5.18 shows SEM pictures of the output facets of 4 and 8-channel multiplexers and the near field images. The length of the first stage coupler is 6

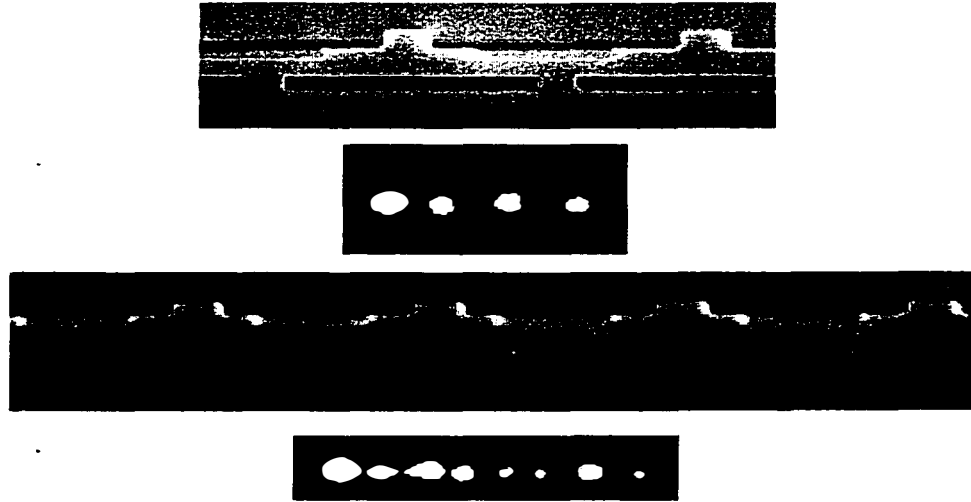


Figure 5.18. SEM pictures and near field images of 4 and 8-channel MUX/DEMUXs.

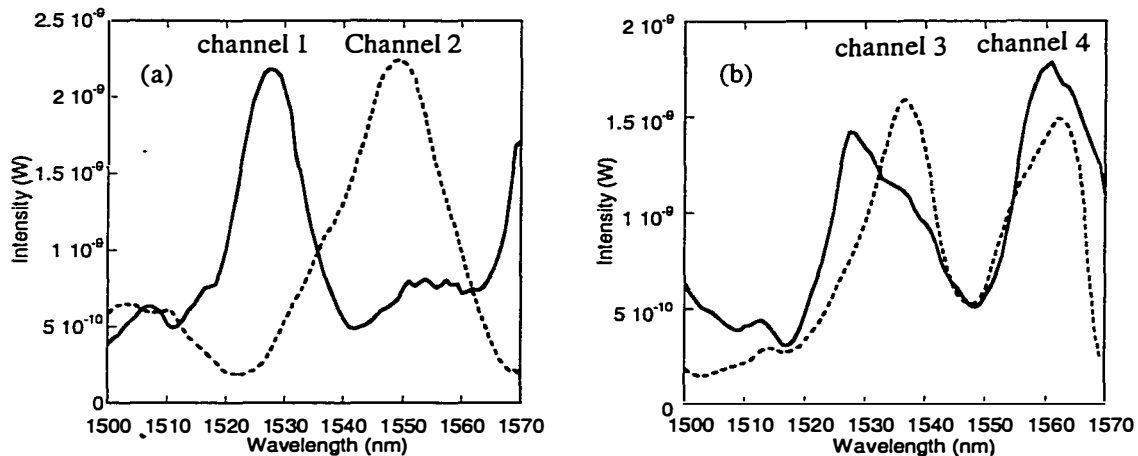


Figure 5.19. Transmission spectra of a 4-channel MUX/DEMUX.

(a) Channel 1 and 2; (b) Channel 3 and 4.

mm, and the separation between two waveguides is 10 μm . The transmission performance of 4-channel multiplexer is shown in Figure 5.19 (a) and (b).

Because of no phase shift in one of the second stage couplers VC22, and the absence of two dummy s-bends, the channels are not interleaved properly and the extinction ratio is not good. In the first generation coupler-based MUX/DEMUX, the waveguide alignment is facilitated using infrared photolithography.

5.4.3 Wavelength multiplexers with phase shift

To improve the performance of coupled based wavelength multiplexers, we incorporate the phase shift and add all dummy s-bends to the second and the third stage couplers to get a symmetric structure. Figure 5.20 is the schematic drawing of the second generation of 4-channel MUX/DEMUX. In this design, the separation between two adjacent output waveguides was increased to 20 μm .

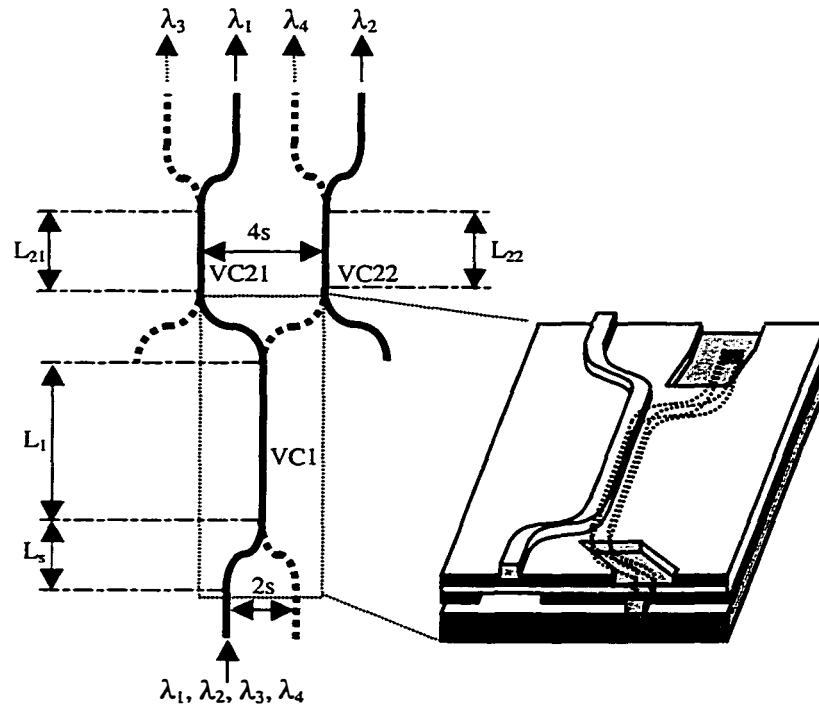


Figure 5.20. Schematic drawing of 4-channel multiplexer, where $L_{21}=L_{22}+L_c/2$, and two dummy s-bends are incorporated for the purpose of symmetry.

Since the s-bends will introduce an extra coupling near the joints, the choice of coupler length must consider the coupling from s-bends. We used a 3D beam propagation analysis to calculate the extra coupling. For example, if $L_1=5$ mm, The parameters are chosen: $L_{21}=2.397$ mm, $L_{22}=2.37$ mm for the vertical couplers and $s=10\mu\text{m}$, $L_s=500\mu\text{m}$ for s-bends.

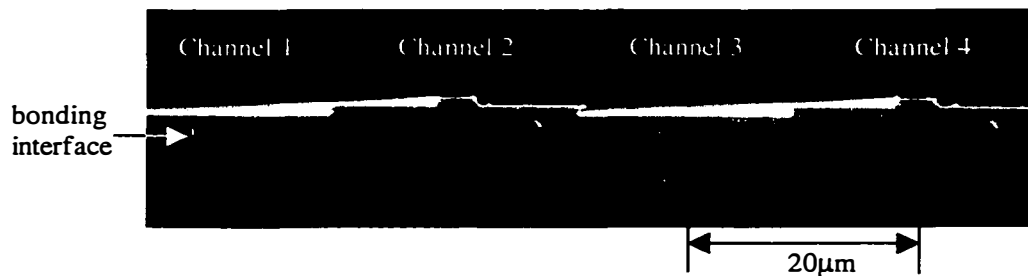


Figure 5.21. The SEM picture of the output facet of a 4-channel MUX/DEMUX.

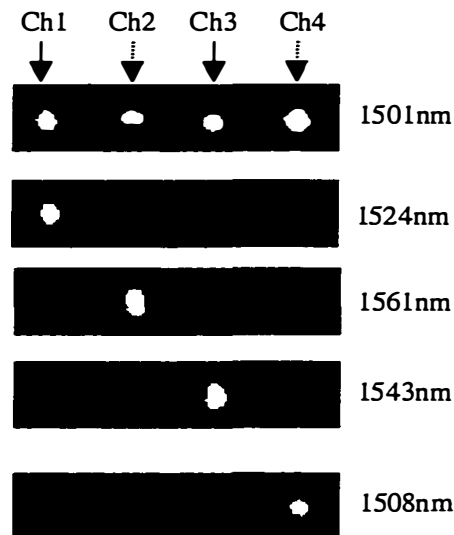


Figure 5.22. The near field images of a 4-channel multiplexer at different wavelengths.

The epitaxial structure is grown using metal organic chemical vapor deposition (MOCVD). The epitaxial structure is the same as the first generation

except a $0.1 \mu\text{m}$ InP cap layer replaces $0.2 \mu\text{m}$ thick one in the first generation. During fabrication, to get a good alignment between upper and lower waveguides, we first open the alignment windows using infrared photolithography and then expose alignment marks using wet etching.

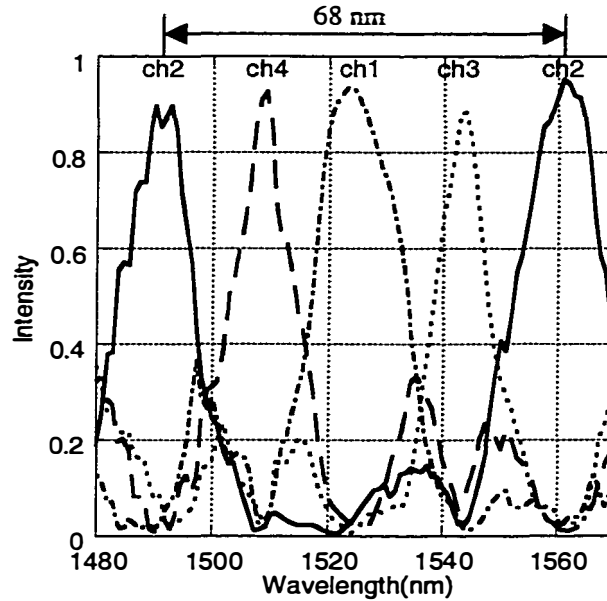


Figure 5.23. 4-channel multiplexer transmission spectra.

- 4-channel multiplexers

We fabricated two multiplexers with different coupler lengths. The first stage coupler length is $L_1=5 \text{ mm}$. Figure 5.21 shows the scanning electron microscope (SEM) picture of the output facet of a 4-channel device. The total device length is about 1.4cm after cleaving both facets. Figure 5.22 shows the near field images at different wavelengths: 1508nm, 1524nm, 1543nm and 1561nm, which are the peak responses of the four channels. The corresponding output light intensity of the TE mode as a function of wavelength for the 4 channels is shown in Figure 5.23. The free spectral range is about 68nm, as can be

seen in the response of channel 2. The channel spacing is 17nm for a 4-channel MUX/DEMUX. The measured adjacent channel crosstalk ranges from -13dB to -20dB. This can be further improved by fine tuning the second stage of vertical couplers to overcome fabrication imperfections or by incorporation of in-line filters.

The second wavelength multiplexer has $L_1=6$ mm, $L_{21}=2.897$ mm and $L_{22}=2.8704$ mm. The transmission spectra from 4 channels are shown in Figure 5.24. Each spectrum has one or two main transmission peaks and several nulls.

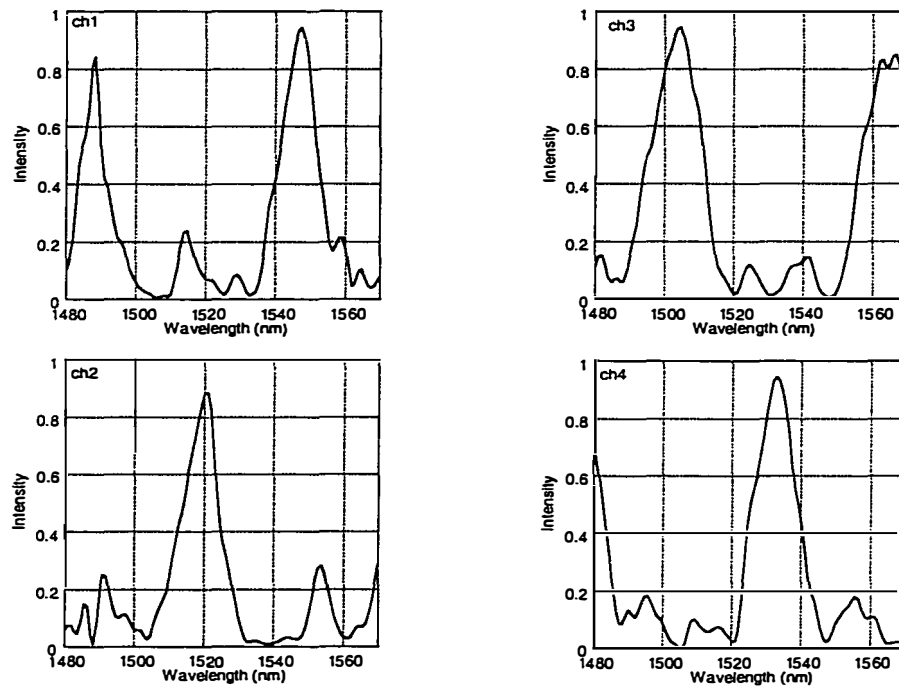


Figure 5.24. 4-channel multiplexer transmission spectra. $L_1=6$ mm.

Ideally, the main peak will line up to the null on all other ports. From channels 1 and 3, we can see the free spectral range is about 59 nm, which corresponds to 15 nm channel spacing. Because the device was not AR-coated, the Fabry-Perot resonance between end facets can be observed in the transmission.

- 8-channel multiplexer

By adding another stage of 4 vertical couplers to the 4 channel multiplexer, we fabricated 8-channel wavelength multiplexers. Figure 5.25 shows SEM picture and the near field images at the output facets of 8-channels

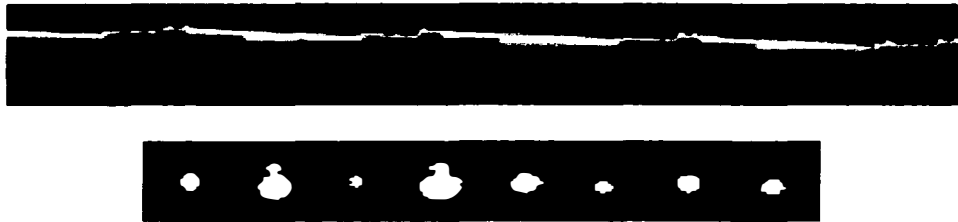


Figure 5.25. SEM picture and near field image of an 8-channel wavelength multiplexer

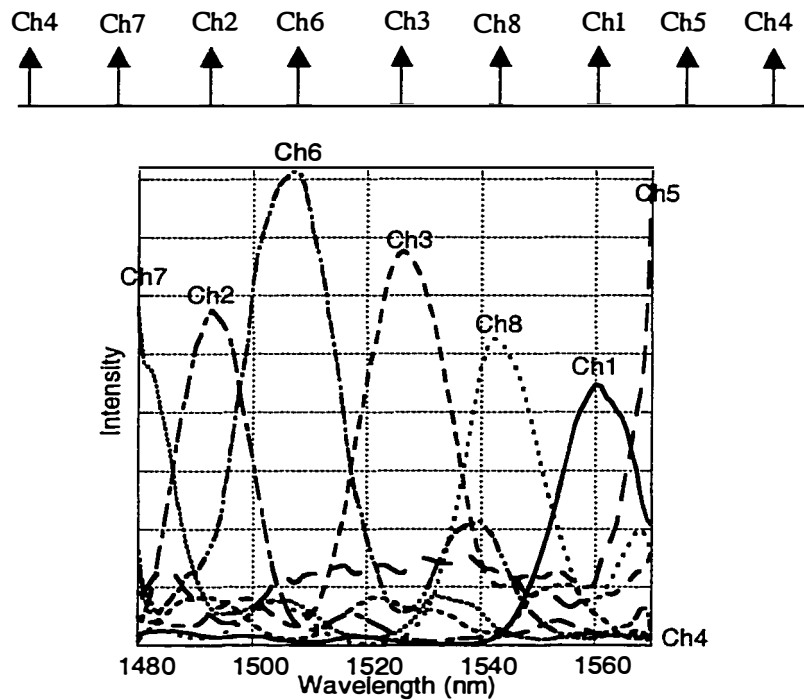


Figure 5.26. Transmission spectra of an 8-channel MUX/DEMUX.

multiplexer. The parameters of 8-channel MUX/DEMUX are $L_1=5$ mm, $L_{21}=2.397$ mm, $L_{22}=2.3704$ mm, $L_{31}=1.123$ mm, $L_{32}=1.096$ mm, $L_{33}=1.0826$ mm, $L_{34}=1.1096$ mm. Since the length of the first stage coupler is the same as the first 4-channel device, the channel spacing is also 17 nm, which is shown in Figure 5.26. Here, we can only observe 7 channels. This is because the peak wavelength of the channel 4 is about 1458 nm or 1594 nm, which is outside the wavelength range of our tunable laser.

The channel spacing can be reduced by increasing the device length or the wavelength dependence of the coupling coefficient. Figure 5.27 shows the transmission spectrum of a two-channel MUX/DEMUX with an 8mm interaction

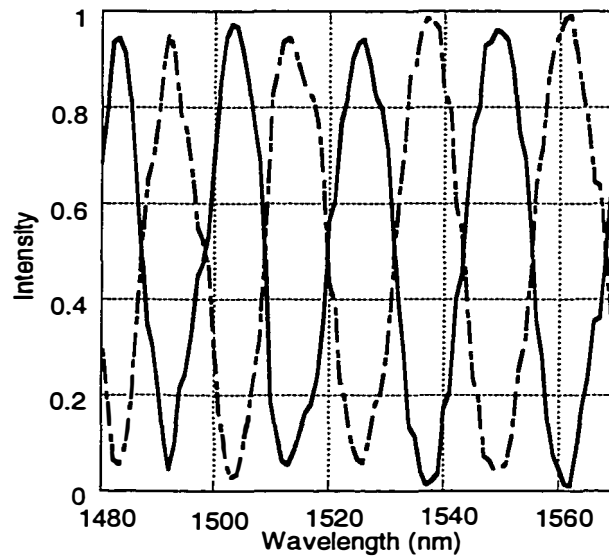


Figure 5.27. The transmission spectrum for a two-channel MUX/DEMUX with 8mm interaction length.

length. The channel spacing is about 11 nm.

5.5 Wavelength selective switch

A multichannel optical wavelength selective switch, which can switch signals at arbitrary wavelengths between multichannels is a key component in WDM

systems. Several versions of this component have been reported including arrayed waveguide gratings (AWG) combined with space switches or phase shifters [15] [16, 17]. Compared to these complicated configurations, vertical coupler based multiplexers may be a simple method to realize wavelength selective switch. We take a 4-channel MUX/DEMUX as an example (see Figure 5.20). If we apply biases to all couplers individually, then we can control the different wavelength to different channels. For example, if we apply a bias to VC21, λ_1 and λ_3 will be switched when the phase shift between λ_1 and λ_3 equals to π . If we want to switch λ_2 from channel 4 to channel 2, then we just apply biases to VC1 and VC21.

Based on our multiplexers, we investigated a 2-channel wavelength selective switch by changing the temperature. Figure 5.28 (a) and (b) show the wavelength can be switched from one channel to another channel when the

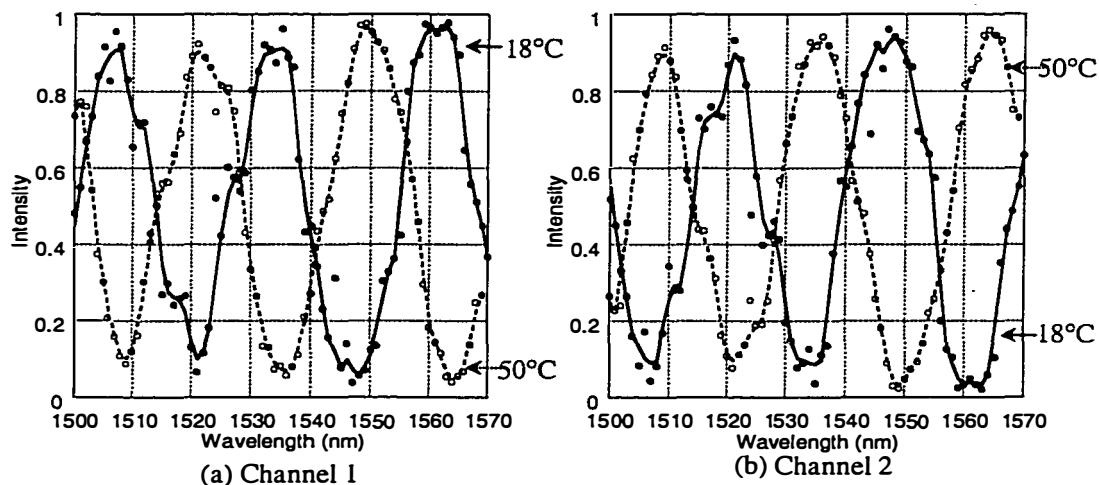


Figure 5.28. The transmission spectra of 2-channel MUX/DEMUX at different temperature. The wavelengths can be switched from one channel to another channel.

temperature was changed from 18°C to 50°C. The device length is 8 mm. The future work should utilize P-i-N structure and the electrooptic effect or carrier injection effect to modulate the index change to realize a fast wavelength selective switch.

The drawback of coupler based wavelength selective switch is that once one wavelength is switched to a channel, other wavelengths cannot be arbitrarily arranged in the remaining channels. For example, in a 4-channel multiplexer (see Figure 5.19), if we switch λ_3 from channel 1 to channel 3, then λ_1 must also be switched from channel 2 to channel 4 and λ_4 (and λ_1) must be switched to channel 1 or 3.

5.6 Summary and discussion

In this chapter, we demonstrated successful implementation of multiple channel wavelength multiplexers using cascaded 3D vertical couplers. 14.5 nm channel spacing and 15 dB channel crosstalk for 4-channel multiplexers with a 6 mm long first stage coupler were achieved. By cascading additional stages of vertical couplers, multi-channel MUX/DEMUXs can be realized. These coupler based wavelength multiplexers may be a low cost choice for coarse WDM (CWDM) applications. Whereas DWDM is based on the ITU 0.8 nm grid, CWDM can use a substantially wider spacing of 20 nm or greater. Because such wide spacing is used between the wavelengths the requirements for laser stability and narrow passband filters are not stringent as that normally required for DWDM systems.

The further improvement of vertical coupler based multiplexers should mainly focus on reducing the crosstalk. A solution is to bias and tune each vertical coupler, which not only can reduce the crosstalk, but can realize wavelength selective switches. Another issue is that the current multiplexers are polarization dependent, which comes from the birefringence of waveguides. This problem can be solved by a proper waveguide design.

References

- [1] J. Minowa and Y. Fujii, "Dielectric multilayer thin-film filters for WDM transmission systems," *J. Lightwave Technol.*, vol. 1, pp. 116-21, 1983.
- [2] J. J. Pan and Y. Shi, "0.4-nm channel spacing dense WDM multiplexer and demultiplexer using FBGs and bandpass filters," , 1998.
- [3] C. Dragone, C. A. Edwards, and R. C. Kistler, "Integrated optics N*N multiplexer on silicon," *IEEE Photonics Technol. Lett.*, vol. 3, pp. 896-9, 1991.
- [4] C. Dragone, "An N*N optical multiplexer using a planar arrangement of two star couplers," *IEEE Photonics Technol. Lett.*, vol. 3, pp. 812-15, 1991.
- [5] W. J. Wang, S. Honkanen, S. I. Najafi, and A. Tervonen, "Four-port guided-wave nonsymmetric Mach-Zehnder interferometer," *Appl. Phys. Lett.*, vol. 61, pp. 150-2, 1992.
- [6] N. Takato, T. Kominato, A. Sugita, K. Jinguji, H. Toba, and M. Kawachi, "Silica-based integrated optic Mach-Zehnder multi/demultiplexer family with channel spacing of 0.01-250 nm," *IEEE J. Sel. Areas Commun.*, vol. 8, pp. 1120-7, 1990.
- [7] I. Bennion, J. A. R. Williams, L. Zhang, K. Sugden, and N. J. Doran, "UV-written in-fibre Bragg gratings," *Optical and Quantum Electronics*, vol. 28, pp. 93-135, 1996.
- [8] F. Bilodeau, D. C. Johnson, S. Theriault, B. Malo, J. Albert, and K. O. Hill, "An all-fiber dense wavelength-division multiplexer/demultiplexer using photoimprinted Bragg gratings," *IEEE Photonics Technology Letters*, vol. 7, pp. 388-90, 1995.

- [9] P. Y. Fonjallaz, H. G. Limberger, and R. P. Salathe, "Bragg gratings with efficient and wavelength-selective fiber out-coupling," *Journal of Lightwave Technology*, vol. 15, pp. 371-6, 1997.
- [10] L. H. Spiekman, M. R. Amersfoort, A. H. De Vreede, F. P. G. M. van Ham, A. Kuntze, J. W. Pedersen, P. Demeester, and M. K. Smit, "Design and realization of polarization independent phased array wavelength demultiplexers using different array orders for TE and TM," *Journal of Lightwave Technology*, vol. 14, pp. 991-5, 1996.
- [11] M. K. Smit and C. Van Dam, "PHASAR-based WDM-devices: Principles, design and applications," *IEEE Journal of Selected Topics in Quantum Electronics*, vol. 2, pp. 236-50, 1996.
- [12] H. C. Cheng and R. V. Ramaswamy, "A dual wavelength (1.32-1.56 μm) directional coupler demultiplexer by ion exchange in glass," *IEEE Photonics Technology Letters*, vol. 2, pp. 637-639, 1990.
- [13] L. Bin, A. Shakouri, P. Abraham, K. Boo-Gyoun, A. W. Jackson, and J. E. Bowers, "Fused vertical couplers," *Applied Physics Letters*, vol. 72, pp. 2637-8, 1998.
- [14] F. Dollinger, M. V. Borcke, G. Bohm, G. Trankle, and G. Weimann, "Ultrashort low-loss optical multiquantum-well GaAs/GaAlAs vertical directional coupler switch," *Electronics Letters*, vol. 32, pp. 1509-10, 1996.
- [15] S. Suzuki, A. Himeno, Y. Tachikawa, and Y. Yamada, "Multichannel optical wavelength selective switch with arrayed-waveguide grating multiplexer," *Electron. Lett.*, vol. 30, pp. 1091-2, 1994.
- [16] O. Ishida, H. Takahashi, S. Suzuki, and Y. Inoue, "Multichannel frequency-selective switch employing an arrayed-waveguide grating multiplexer with fold-back optical paths," *IEEE Photonics Technol. Lett.*, vol. 6, pp. 1219-21, 1994.

- [17] C. R. Doerr, C. H. Joyner, L. W. Stulz, and R. Monnard, "Wavelength-division multiplexing cross connect in InP," *IEEE Photonics Technology Letters*, vol. 10, pp. 117-19, 1998.

Chapter 6

X-crossing Vertical Coupler Add/drop Filter

6.1 Overview of optical filters

One of the key components for the practical realization of wavelength division multiplexing transmission systems is optical add and drop filters or multiplexers (OADMs) [1] that have simultaneous functions of wavelength selection and routing of the selected channels. Many different types of filters and multiplexers have been reported. Based on the operation mechanisms, wavelength filters can be categorized into three types.

- Filters that are based on the wavelength dependence of interferometric phenomena. These include Fabry-Perot interferometer filters [2-4]; Mach-Zehnder interferometric filters [5-7]; Arrayed waveguide grating multiplexers [8, 9] and ring resonators.
- Filters that are based on the wavelength dependence of coupling between optical modes in waveguides. These include acousto-optic [10-12], electro-optic [13, 14] and magneto-optic [15] filters.
- Filters that are based on resonant amplification of the optical signal in semiconductor laser diode devices. These devices [16] provide gain in addition to wavelength selectivity.

The most promising approaches include cascaded Mach-Zehnder interferometric filters, acousto-optic filters, grating and arrayed waveguide based multiplexers. Although the characteristics of these structures can satisfy the requirement of WDM systems, their complexity and cost will be the main challenges to their deployment. InGaAsP/InP vertical coupler filters [17-22] as

OADM's are of particular interest, because of simple configuration, large wavelength tunability and their inherent potential for monolithic integration with other optoelectronic devices (such as lasers, amplifiers, switches, detectors, etc). These advantages are attributed to the easy control of waveguide parameters (thickness and indices) and well-developed fabrication technique. There are two kinds of vertical coupler filters. One is grating-assisted co-directional [18] or contra-directional [23, 24] coupler filter. Because of the existence of a grating, generally, regrowth is needed to embed the grating in the waveguides, which complicates the fabrication. In this chapter, we will study another type of vertical coupler filters that directly stack two strong asymmetric waveguides vertically together without the assistance of a grating. Since there is no grating, the fabrication and design are much simpler than the grating-assisted vertical coupler filters.

Although vertical coupler filters have already been proposed and demonstrated for a long time, their application has been limited by some inherent disadvantages. A limitation in vertical couplers has been coupling to conventional fibers. Direct coupling is impossible since in traditional vertical coupler filters the spacing between the two waveguides is only about $1\mu\text{m}$. Etching and regrowth can be used to separate the two waveguides [23] [24], but regrowth and lateral propagation over nonplanar surfaces is problematic. Another problem is a high sidelobe (-9 dB) existing in conventional vertical coupler filters due to the uniform coupling along the length of two parallel waveguides. To reduce the sidelobe the two waveguides should be gradually coupled. This is quite difficult to realize using conventional techniques. In this chapter, with the help of wafer bonding technique, a simple OADM based on X-crossing InP/InGaAsP vertical coupler filter is proposed and demonstrated. With an X-crossing configuration, the two input and output waveguides can be laterally separated for direct coupling to fibers, and the side-lobe level is reduced to -26dB.

We will start by describing the operation principle and design of X-crossing InP/InGaAsP vertical coupler filters in Section 6.2. The fabrication will be described in Section 6.3. The experimental results will be given in Section 6.4. Several methods to realize polarization insensitive vertical coupler add/drop filters will be discussed in Section 6.5.

6.2 Design of X-crossing vertical coupler filters

6.2.1 Basic operation principle of parallel coupler filters

The conventional straight vertical coupler filters comprise two strongly

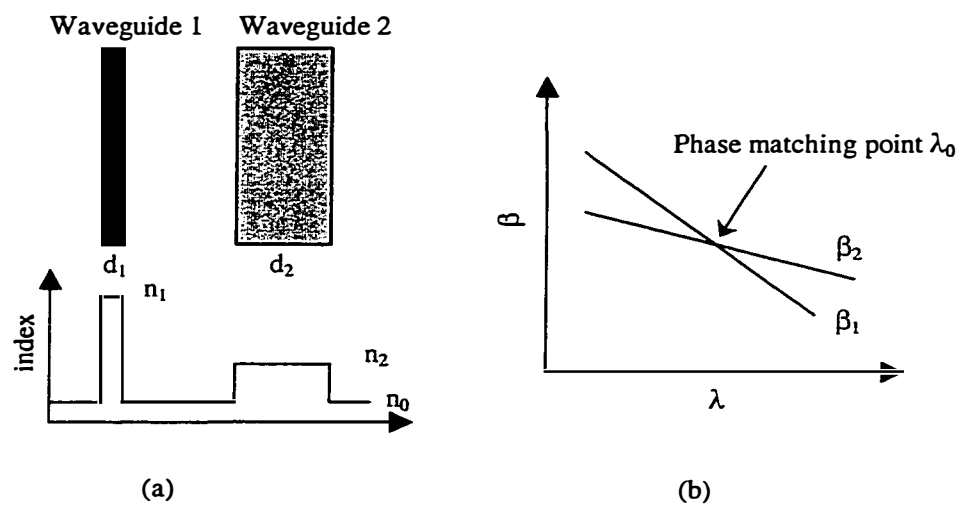


Figure 6.1. The operation principle of an asymmetric coupler filter.

(a) index profile of two waveguides.

(b) dispersion curves of two waveguides.

asymmetric waveguides, as shown in Figure 6.1 (a). A graphical explanation of the operation principle is plotted in Figure 6.1 (b). The waveguides have propagation constants $\beta_1 = \frac{2\pi}{\lambda}n_1$ and $\beta_2 = \frac{2\pi}{\lambda}n_2$, where λ is the free space wavelength and n_1 and n_2 are the effective indices.). The waveguide 1 has a very

large index difference between the core and the cladding, and a small core size, and the waveguide 2 has a small index difference and a large core size ($d_2 \gg d_1$). Therefore they have different dispersion characteristics. At a particular wavelength (phase-matching point), those two dissimilar waveguides have the identical propagation constants and only light at this wavelength can be completely transferred from one to another waveguide after the coupling length. At other wavelengths, due to phase mismatching, the coupling is very weak and filtering results. This is the basic operational principle of a coupler filter.

6.2.2 Coupled mode analysis

Coupled mode theory is widely used to synthesize the performance of coupler filters. Since the coupling is very weak for a narrow band coupler filter, we can ignore the self-coupling terms and the cross mode overlap terms (see Chapter 3). From Equation (3.5), the coupling efficiency to the other waveguide with unit input to one guide is given by

$$F = \frac{\sin^2(L\sqrt{\kappa^2 + \delta^2})}{1 + \frac{\delta^2}{\kappa^2}} \quad (6.1)$$

where κ is the coupling coefficient and $\delta = \frac{\beta_2 - \beta_1}{2}$ is the wavelength dependent phase mismatch. When $\delta=0$ and

$$\kappa L = \frac{m\pi}{2} \quad (6.2)$$

m is an odd integer, 100% transmission occurs. From Equation (6.1), the full-width half maximum (FWHM) $\Delta\lambda$ can be obtained by

$$\Delta\lambda = \frac{0.8\lambda_0}{L\left(\frac{dn_1}{d\lambda} - \frac{dn_2}{d\lambda}\right)_{\lambda=\lambda_0}} \quad (6.3)$$

where λ_0 is the phase matching point. To get a narrow band filter, one can increase the device length and the differential dispersion. But in practice, the device length is limited due to the absorption loss and the desire for small devices. The differential dispersion is therefore the factor that should be maximized.

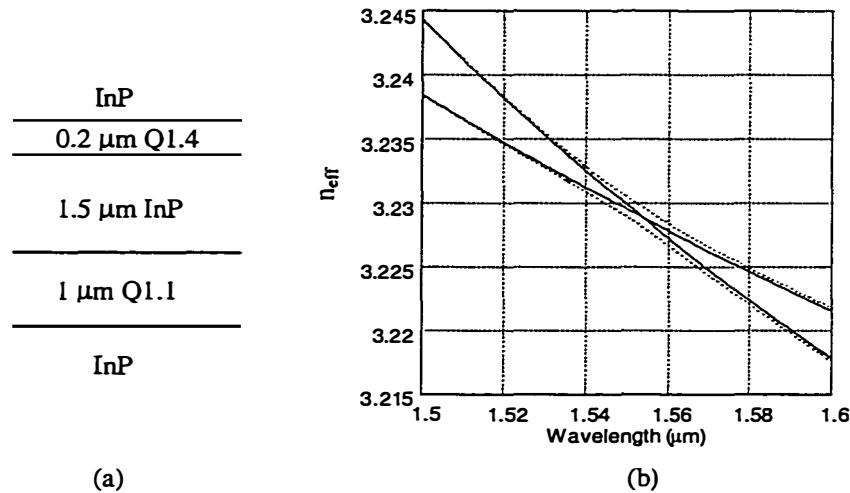


Figure 6.2. (a) the structure of a 2D vertical coupler structure.
(b) The effective indices of uncoupled individual waveguide modes (solid line) and coupled supermodes (dash line) as a function of wavelengths.

For simplicity, we take a 2D vertical coupler filter as an example to show how to analyze a coupler filter. Figure 6.2 (a) shows the schematic drawing of this filter, which consists of two vertically stacked waveguides with different core regions. The lower guiding layer is 1 μm thick InGaAsP that has a bandgap at 1.1 μm and the upper guiding layer is 0.2 μm thick InGaAsP with bandgap at 1.4 μm. The separation between two waveguides will decide the coupling length. The general calculation involves three steps. First, the dispersion curves of two uncoupled waveguides must be calculated to know the phase matching wavelength. Figure 6.2 (b) shows the effective indices of two waveguides as a function of wavelength. Second, the coupling coefficient κ is calculated to

determine the coupling length (see Chapter 3). This step is tedious and time consuming in all calculations. For 2D coupler filters, the simplest way is to

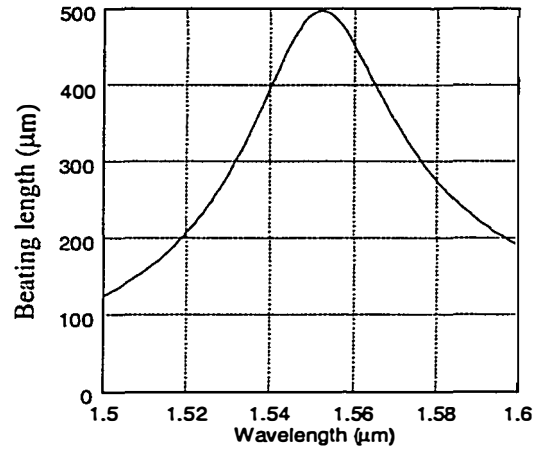


Figure 6.3. The beating length between even and odd supermodes as a function of wavelength.

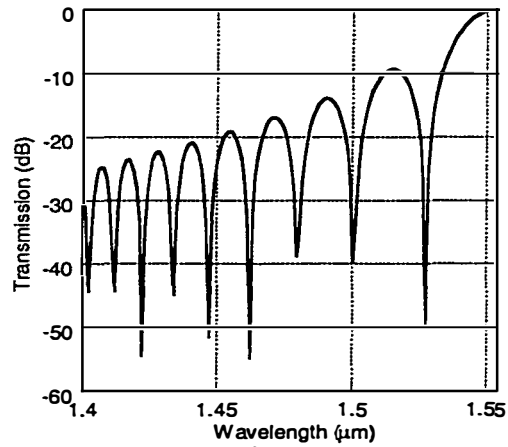


Figure 6.4. The transmission of a vertical coupler with uniform coupling.

calculate the effective indices of two supermodes (even and odd modes) as shown in Figure 6.2 (b). The coupling length L_c can be obtained from

$$L_c = \frac{\lambda}{2(n_e - n_o)} \quad (6.4)$$

at the phase matching wavelength, where n_e and n_o are the effective indices of even and odd supermodes. Figure 6.3 shows the calculated beating length from Equation (6.4) as a function of wavelength. Then we can easily find the coupling coefficients using Equation (3.9). From Figure 6.3, we also can get the phase matching wavelength, which corresponds to the maximum of the beating length. This value is more precise than that arrived at from the individual waveguide calculations. Finally, coupled mode theory is used to simulate the filter transmission. Figure 6.4 shows the filter response, where only the lower half of relevant wavelengths are plotted.

5.2.3 Side lobe suppression by X-crossing coupling

From Figure 6.4, we can observe there is a very high side lobe (-9dB) in uniform coupled filters (κ is independent of the light propagation position z). For many applications, such a high side lobe is unacceptable, because it will introduce crosstalk between adjacent channels. Therefore, suppressing the side lobe levels of vertical coupler filters becomes very important for their applications.

Approximately, there is a roughly Fourier transform relationship [25] between $\kappa(z)$ and the filter response $F(\lambda)$. For a uniform coupling, $\kappa(z)$ is a window function, and the corresponding Fourier transform is a Sinc function (see Equation (6.1)). From the Fourier transform point of view, any abrupt change in the coupling distribution raises the sidelobe level, and transform-sidelobes of a function are low if the function gradually rolls-off at the ends of the interval. Hence, the side lobe will be drastically suppressed if we can achieve a taper function of $\kappa(z)$. The coupling interaction can be controlled by adjusting the waveguide separation or by applying a weighting function on the applied electrodes of the electrooptic or acusto-optic filters. Many weighting functions have been extensively studied, such as truncated Gaussian [26], Hamming, Raised

Cosine, Blackman, Kaiser [25]. Theoretically, an optimum taper can always be found to get arbitrary sidelobe suppression down to -125dB [27].

From the fabrication point of view, a simple tapered function is preferred

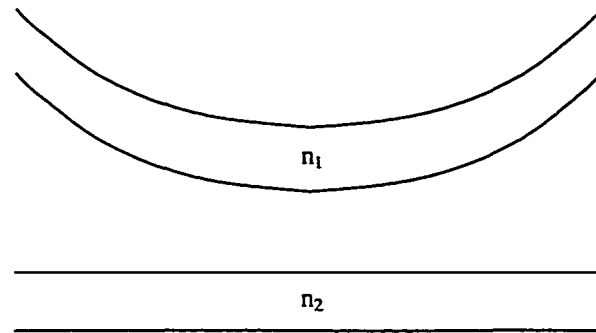


Figure 6.5. Schematic diagram of a coupler filter with tapered coupling strength by changing the waveguide separation.

because it simplifies the design and processing. The simplest tapering can be achieved by varying the separation between the two waveguides along the length of the coupler filter, as shown in Figure 6.5. This structure is suitable for applications to horizontal coupler filters where the two waveguides are placed laterally apart in the same plane [28]. However it is very difficult to achieve this in conventional vertical coupler filters where the two waveguides are not in the same plane.

As we discussed in last chapter, the wafer bonding technique provides us an extra freedom to fabricate 3D photonic devices. It makes tapering the coupling strength by arranging two X-crossing waveguides of vertical coupler filters in different planes possible. A schematic diagram of an X-crossing vertical coupler filter is shown in Figure 6.6. The fabrication will be discussed in detail in the next section. The filter consists of two vertically stacked waveguides with different quaternary compositions. The lower guiding layer is a thin InGaAsP that has a bandgap at 1.4 μm and the upper guiding layer is a thick InGaAsP with bandgap

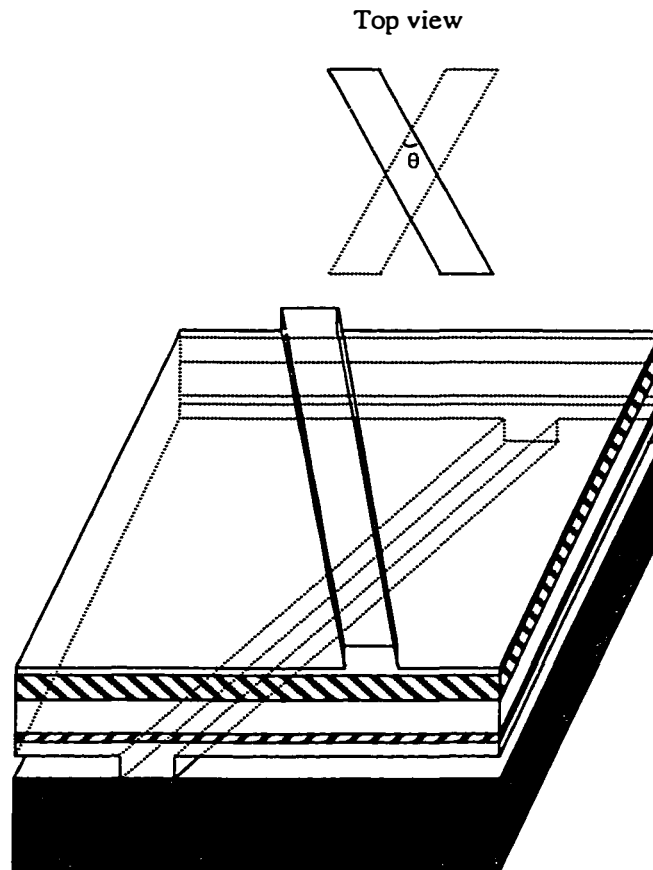


Figure 6.6. Schematic drawing of an X-crossing vertical coupler filter

at $1.1 \mu\text{m}$, and the width of two waveguides is $3 \mu\text{m}$. The detailed structure is shown in Figure 6.7.

In the design of the filter, we first use the effective index method to calculate the effective indices and the mode field profiles of the uncoupled upper and lower waveguides. Then coupled mode theory is used to evaluate the coupling coefficient and wavelength response.

To maximize the differential dispersion, we should choose one InGaAsP layer with the smaller bandgap wavelength as thick as possible, but the single mode condition must be kept. $1 \mu\text{m}$ thickness is the maximum thickness we can

have when the bandgap is $1.1 \mu\text{m}$. The parameters of the other waveguide with a longer bandgap wavelength can be decided by matching the propagation constants of the two waveguides at the desired λ_0 . Figure 6.8 shows the calculated effective indices of two waveguides for TE modes. The phase matching point is about $1.556 \mu\text{m}$.

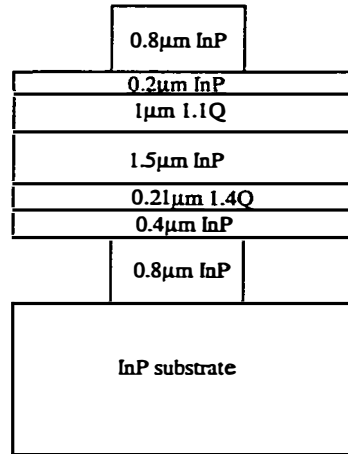


Figure 6.7. The detailed structure of vertical coupler filter.

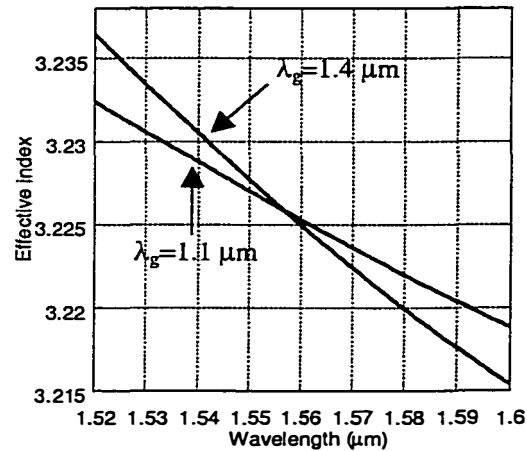


Figure 6.8. The calculated effective indices as a function of wavelength.

To determine the coupling coefficient $\kappa(z)$ of the crossed over waveguides, step-like approximation is introduced [29]. First, the X-crossing

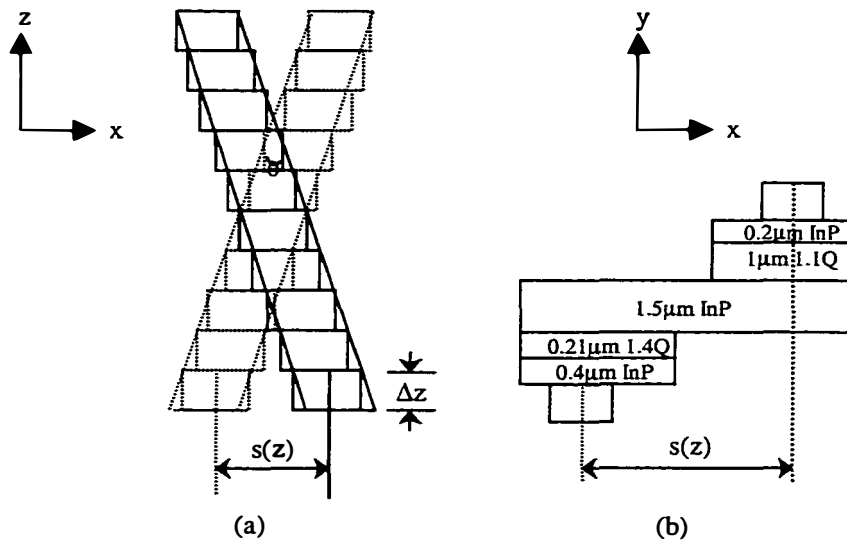


Figure 6.9. Step-like approximation for X-crossing coupler.

waveguides are divided into many short sections (see Figure 6.9 (a)). Each of the segments has a very short length (Δz), and is separated $s(z)$ (see Figure 6.9 (b)). Based on the calculated mode profile, $\kappa(z)$ is determined by numerical integration. Once $\kappa(z)$ is evaluated, a transfer matrix method based on CMT procedure can be used to calculate the filter response at different crossing angles. This approximation is an efficient way for the purpose of design. Certainly, this method will not be accurate for a large crossing angle.

Figure 6.10 shows the calculated coupling coefficient $\kappa(z)$ at different angles. The resulting z -dependent interaction strength will suppress the side lobes to a very low level. Figure 6.11 is the simulated filter response with a crossing angle of 0.25° , where the side lobe level has been suppressed to below -40 dB. The equivalent coupling region will change with the crossing angle. When the equivalent interaction length equals an odd multiple of the coupling length, the complete power transfer happens. When the equivalent interaction length is an

even multiple of the coupling length, no power is transferred at the peak wavelength. The relationship between the coupling efficiency and the crossing angle is shown in Figure 6.12.

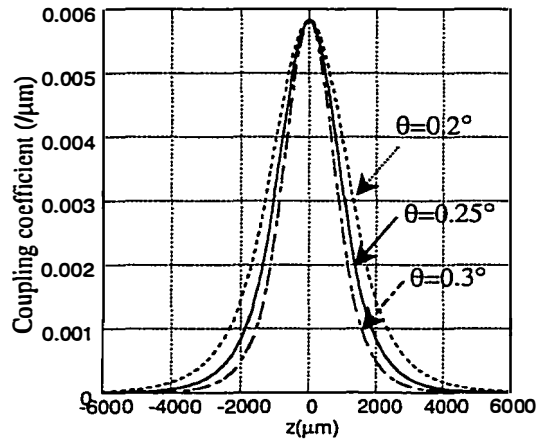


Figure 6.10. The coupling coefficient as a function of z for different crossing angles.

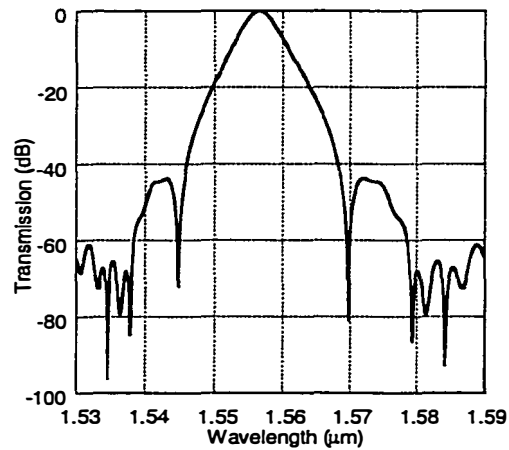


Figure 6.11. The simulated x-crossing vertical coupler filter response with an angle of 0.25° .

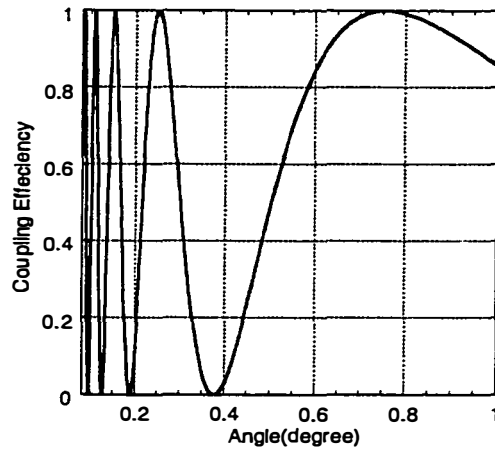


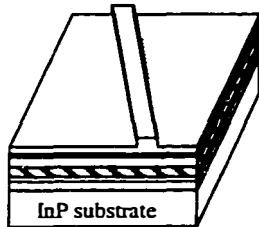
Figure 6.12. The calculated coupling efficiency as a function of crossing angle.

6.3 Device Fabrication

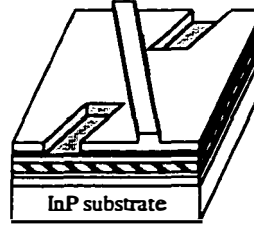
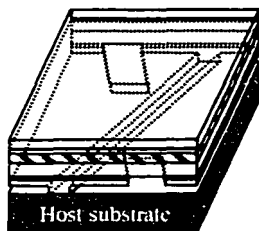
The device structure was grown using metal organic chemical vapor deposition (MOCVD) on an InP substrate as usual. The detailed structure is shown in figure 6.7. The fabrication process of X-crossing vertical coupler filters is shown in Figure 6.13. Similar to the fabrication of vertical coupler based wavelength multiplexers, wafer bonding and double-sided process are the keys to realize X-crossing structures. The main steps are:

- a. The lower InGaAsP ($\lambda_g=1.4\mu\text{m}$) ridge waveguides are formed by MHA ($\text{CH}_4/\text{H}_2/\text{Ar}$) reactive ion etching or chemical wet etching, where the ridge height is $0.8\mu\text{m}$ and its width is $3\mu\text{m}$ (Figure 6.13 (a)).
- b. The $1.4\mu\text{m}$ quaternary layer below the top $1.1\mu\text{m}$ InGaAsP waveguides at two ends of the sample is removed by another chemical etching step (Figure 6.13 (b)) to get rid of the unneeded coupling.

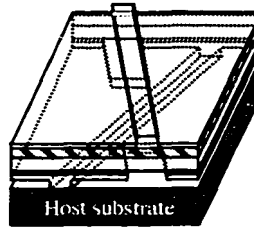
- c. The sample is inverted and fused to a second InP substrate under pressure and in H_2 atmosphere. Then the original substrate and the etching stop layer (Figure 6.13 (c)) are removed by wet etching.
- d. The upper $1.1\mu\text{m}$ quaternary waveguides are fabricated (Figure 6.13 (d)).



(a) form the upper waveguide.

(b) remove InGaAsP ($\lambda_g=1.4\mu\text{m}$) layer.

(c) invert sample and bond to a host substrate, remove original substrate and etch stop layer.



(d) fabricate another waveguide.

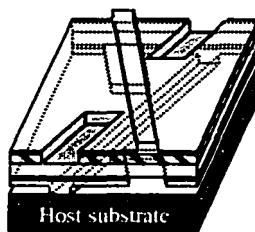
(e) remove InGaAsP ($\lambda_g=1.1\mu\text{m}$) layer.

Figure 6.13. The fabrication process of X-crossing vertical coupler filter.

e. The 1.1 μm InGaAsP layer above the lower 1.4 μm InGaAsP waveguide region is removed as before (Figure 6.13 (e)).

The alignment is facilitated using infrared photolithography or by opening the alignment windows. Compared to wavelength multiplexers, the alignment here is less critical.

6.4 Results

6.4.1 The initial filters

The waveguides in the first generation of filters were fabricated by wet etching. We fabricated two samples: the upper waveguide is along [110] and [1 $\bar{1}$ 0] direction respectively. Figure 6.14 is the SEM picture of the output facet of an X-crossing vertical coupler filter. A tunable semiconductor laser with a polarization controller was used as a light source to measure the performance of the X-crossing vertical coupler filter. The device was mounted on a temperature-controlled stage and single mode fibers were butt-coupled to the input and output waveguides. Figure 6.15 shows the TE mode transmission spectrum of an X-crossing vertical coupler filter with the crossing angle 0.35°. The light is launched in the upper waveguide ($\lambda_g=1.1\ \mu\text{m}$). The 3dB bandwidth is about 4.5nm and the peak wavelength is 1555 nm for the TE mode at 22°C. The peak wavelength of these filters is very sensitive to the dimensions and the refractive indices of the waveguides. Because the anisotropic wet etch produces different profiles along [110] and [1 $\bar{1}$ 0], when the upper waveguide is along [1 $\bar{1}$ 0] direction, the width of the upper 1.1 μm quaternary waveguides is much wider than that of the lower waveguide (see Figure 6.14). It moves the filter peak wavelength to 1516nm, and the corresponding 3dB bandwidth becomes 3nm. The narrow bandwidth is due to the strong material dispersion of 1.4 μm quaternary at short wavelengths.



Figure 6.14. The SEM picture of the output facet of the initial filter.

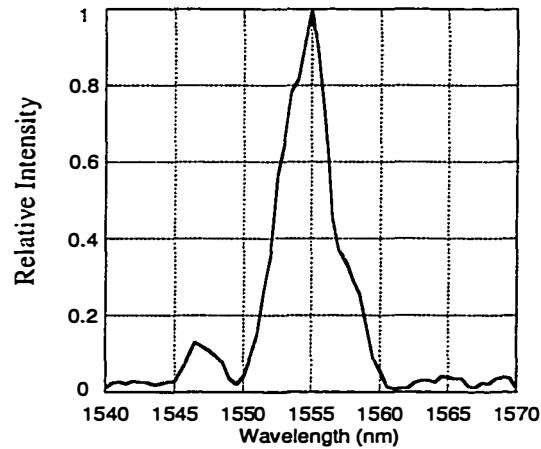


Figure 6.15. TE mode transmission spectrum of an X-crossing filter, where the upper waveguide ($\lambda_g=1.1 \mu\text{m}$) is along $[110]$ direction.

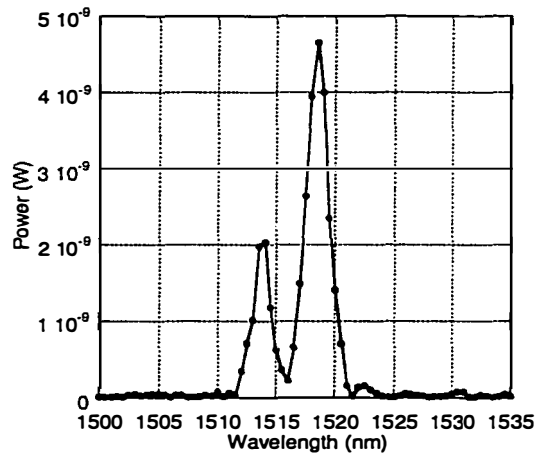


Figure 6.16. The transmission spectrum of an X-crossing filter, where the upper waveguide is along $[1\bar{1}0]$ direction (Figure 6.14).

Since $1.1\mu\text{m}$ and $1.4\mu\text{m}$ quaternary materials have different thermo-optic

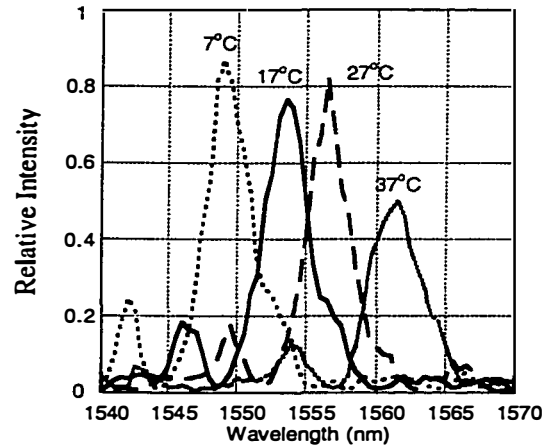


Figure 6.17. Transmission spectra at different temperatures.

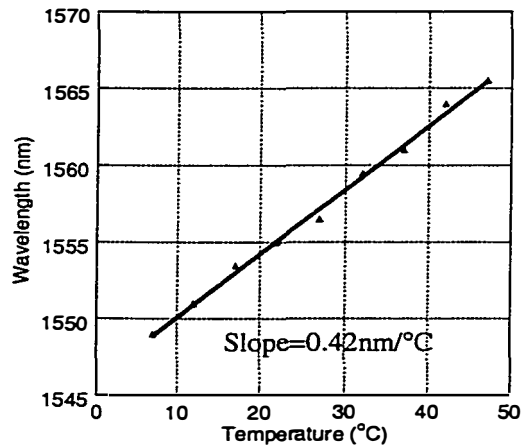


Figure 6.18. Peak wavelength as a function of temperature.

coefficients, the peak wavelength of the InGaAsP/InP vertical coupler filters can be tuned by changing the stage temperature. Figure 6.17 shows the transmission spectra at different wavelengths. The dependence of the peak wavelength on the temperature is shown in Figure 6.18. There is a large tuning rate of $0.42\text{nm}/^\circ\text{C}$. Furthermore one can achieve a wider tuning range that covers all WDM channels in $1.5\ \mu\text{m}$ commercial long haul links by using carrier injection effect [19, 20].

The response of the above X-crossing vertical coupler filter has a small side peak on the short wavelength side when light is launched in the upper waveguide. This is caused by the coupling between the upper 1.1 μm quaternary ridge waveguide and the lower 1.4 μm quaternary slab guiding layer before two waveguides overlap together (see Figure 6.19). This can be removed by changing

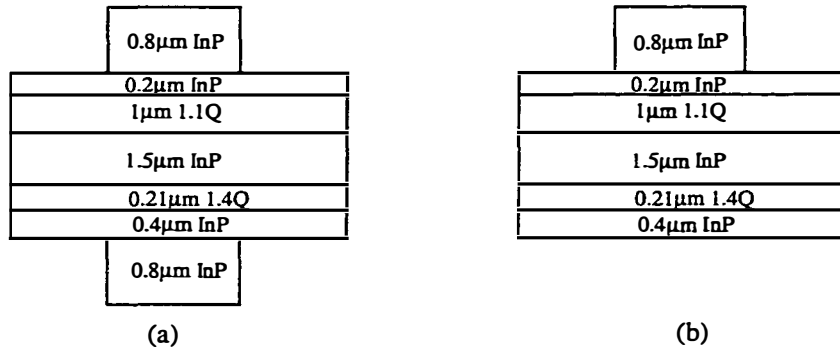


Figure 6.19. (a) The coupling between the upper and lower waveguides creates the main peak. (b) The coupling between the upper waveguide and the lower slab waveguide causes the small side peak. Notice that this is the structure of the conventional vertical coupler filter and the lower waveguide is very weakly guided.

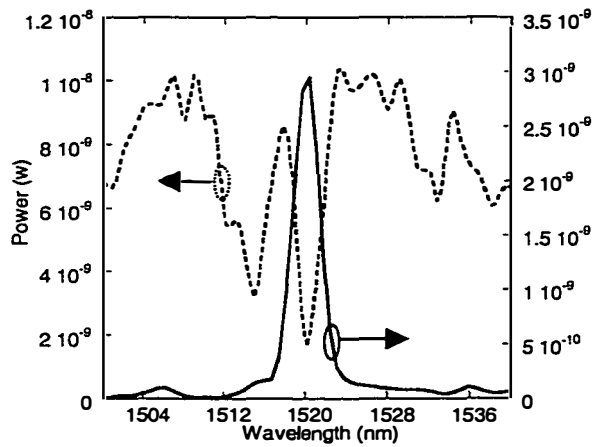


Figure 6.20. Transmission spectra of an X-crossing filter with 0.15° angle. The light is launched from the upper waveguide. Solid line is the output from the lower waveguide ($\lambda_g=1.4 \mu\text{m}$) and dash line is the output from the upper waveguide ($\lambda_g=1.1 \mu\text{m}$).

the waveguide structures as shown in the revised filters later. At some special angles, the light coupled to the slab waveguide can couple back to the input waveguide, and the side peak will not exist in this case. Figure 6.20 shows the output from the upper and lower waveguides in an X-crossing filter with 0.15° crossing angle. The light is launched in the upper waveguide and the upper waveguide is along the $[1\bar{1}0]$ direction. We can see that the side peak disappears in the output of the lower waveguide, but there are two dips in the output of upper waveguide. This is because there is a very high loss in the lower waveguide ($\lambda_g=1.4 \mu\text{m}$). Any light that goes to the lower waveguide will be absorbed, and this absorption causes the dips. When we check the transmission of the upper to upper waveguide (input and output are both in upper waveguide) in the filters with the $[110]$ direction upper waveguides, we find the same situation, as shown in Figure 6.21. The lower to lower waveguide shows there is a very high loss when $\lambda < 1540 \text{ nm}$. If we ignore the small peak, the side lobe level is smaller than -14dB , which will be further improved by changing the waveguide design.

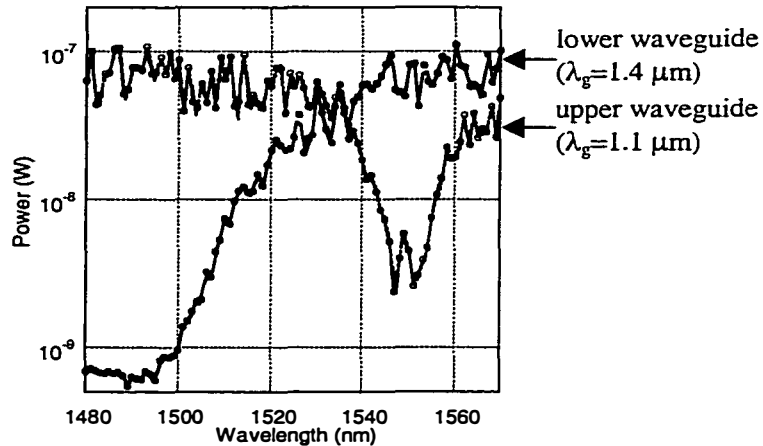


Figure 6.21. Transmission of upper to upper and lower to lower waveguides.

6.3.2 The revised optical add/drop filters

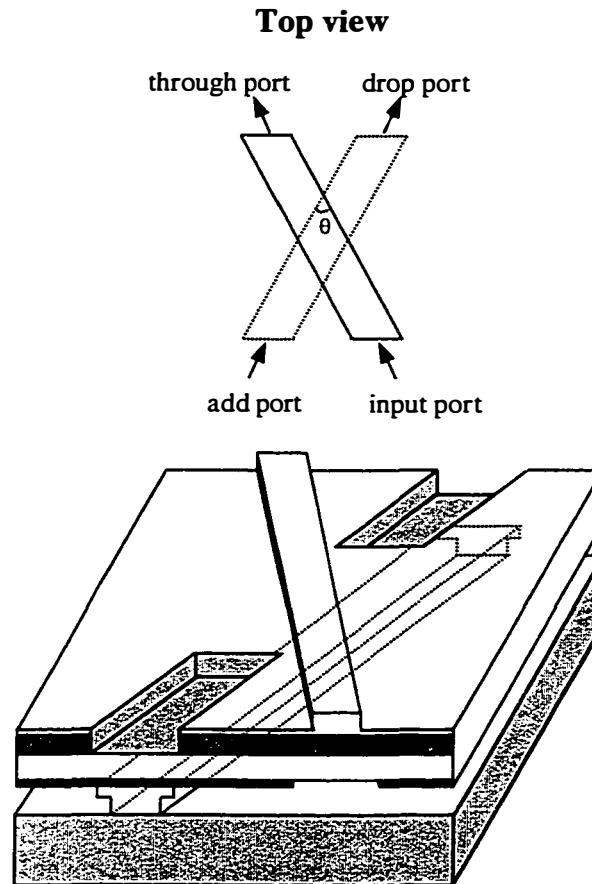


Figure 6.22. Schematic drawing of vertical coupler based optical add/drop filter.

To remove the side peak in the initial filters, we modified the X-crossing structure in the second round. Figure 6.22 shows the schematic diagram of the revised optical add/drop filters. Compared to the initial filter, we remove the lower $0.4 \mu\text{m}$ InP cladding layer (see Figure 6.23). This will move the phase matching point between the upper waveguide and the lower slab waveguide to a very short wavelength. Figure 6.24 shows the calculated effective indices of the upper waveguide and the lower slab waveguide with and without $0.4 \mu\text{m}$ InP

cladding. With $0.4 \mu\text{m}$ InP cladding, the phase matching point is about $1.53 \mu\text{m}$, which near the peak wavelength $1.55 \mu\text{m}$ of this X-crossing filter. Without $0.4 \mu\text{m}$ cladding, the two curves don't cross over in this plot. The phase matching point is

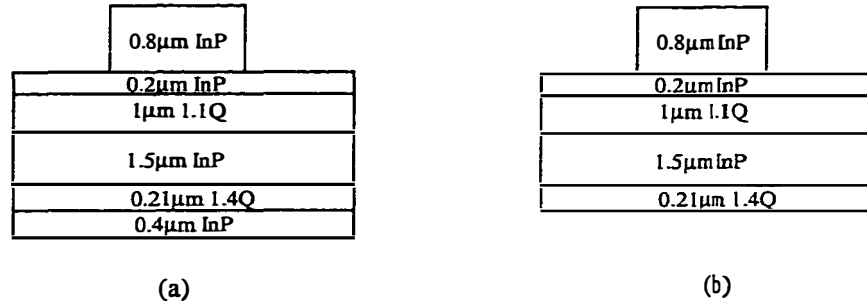


Figure 6.23. (a) The phase matching point between the upper waveguide and the lower slab guiding is near the peak wavelength of the filter. (b) By removing the lower $0.4 \mu\text{m}$ InP cladding layer, the phase matching point will be moved far away from the peak wavelength of the filter.

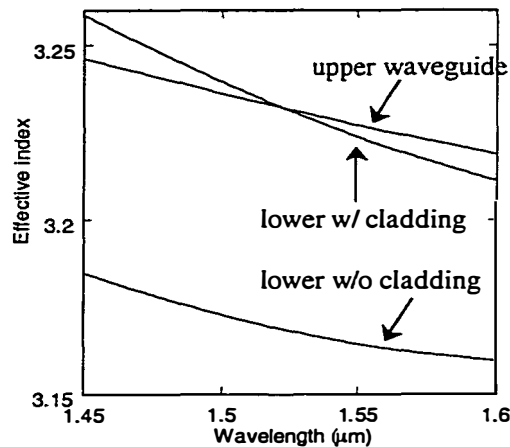


Figure 6.24. The calculated effective indices of the upper waveguide and the lower slab waveguide with and without $0.4 \mu\text{m}$ InP cladding layer.

smaller than $1.2 \mu\text{m}$, which is even shorter than the material bandgap wavelength. Therefore, the side peak existing in the initial X-crossing filters will be removed in this structure.

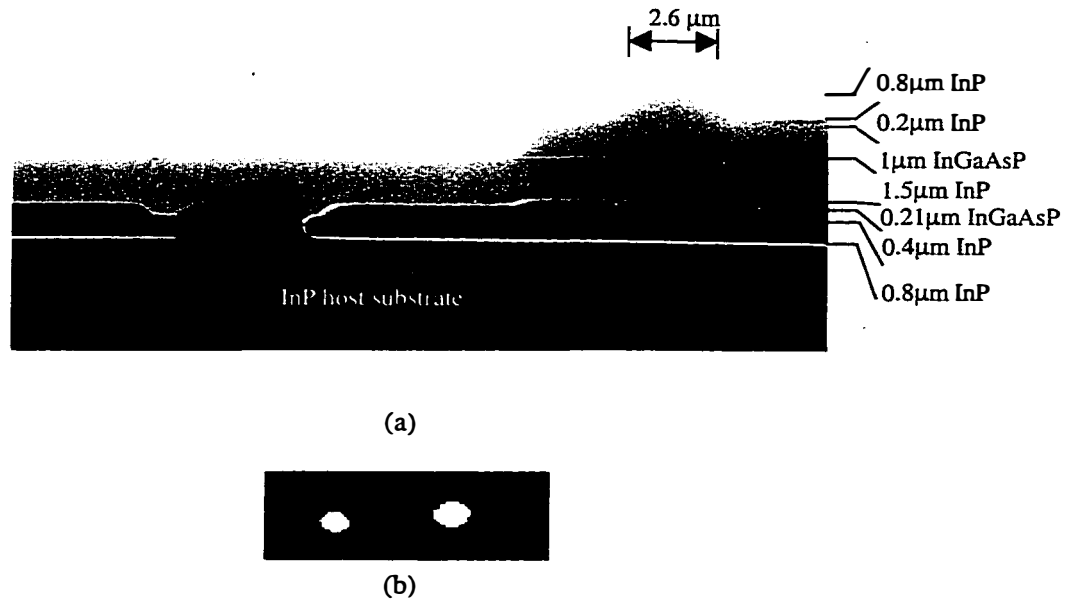


Figure 6.25. (a) The SEM picture of the output facet.
 (b) The near field pattern at the output facet.

We use the same grown wafer to fabricate the second round X-crossing filters. The fabrication is similar to the initial devices. The difference is that RIE dry etching is first used to etch the lower 0.8 μm ridge, then 0.4 μm cladding layer is removed by wet etching. Since the lower InGaAsP ($\lambda_g=1.4 \mu\text{m}$) layer has a very high loss when $\lambda < 1540 \text{ nm}$, we overexpose the upper waveguide and shrink the guiding width to move the filter peak to a long wavelength. Figure 6.25 (a) shows the SEM picture of the output facet of an X-crossing OADM with a crossing angle of $\theta=0.1^\circ$. The near field pattern at the output facet is shown in Figure 6.25 (b).

The transmission spectra of the TE mode from input port to the drop and through ports of an OADM with the crossing angle of 0.25° are shown in Figure 6.26, where the data have been normalized to the total output power from through and drop ports. The 3dB bandwidth is 6nm. The sidelobe level has been suppressed to below -25 dB in this device. The fiber to fiber loss is about -21 dB.

By improving the fiber coupling efficiency and the lower waveguide material quality, this loss can be reduced to about -10 dB. The transmission spectra from

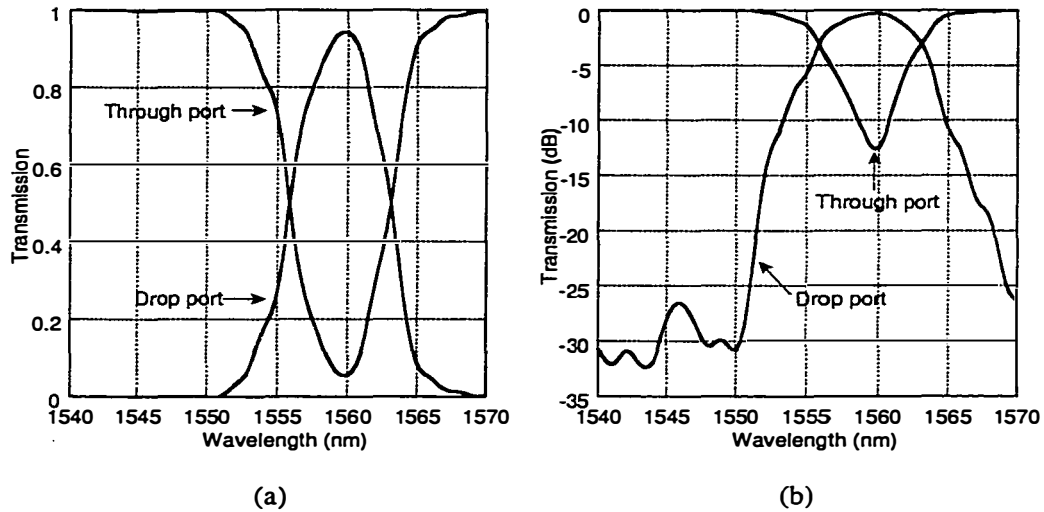


Figure 6.26. The TE mode transmission spectra from input port to drop and through ports of an OADM with X-crossing angle of 0.25° . (a) Linear scale, (b) Log scale.

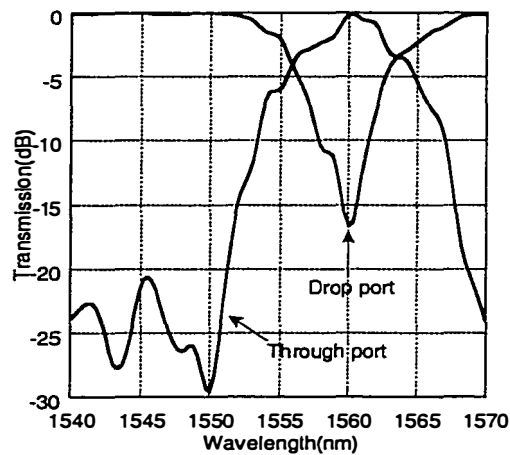


Figure 6.27. The TE mode transmission spectra from add port to through and drop ports of an OADM with X-crossing angle of 0.25° .

add port to through and drop ports are also shown in Figure 6.27. The corresponding fiber to fiber loss is about -25 dB, which is higher than the loss

when light is launched in the top waveguide. This is because the $1.4\ \mu\text{m}$ InGaAsP waveguide has a much higher absorption than the $1.1\ \mu\text{m}$ InGaAsP waveguide at $1.55\ \mu\text{m}$. The coupling efficiency from add port to through port is above 97%, which strongly depends on the crossing angle. Figure 6.28 shows the measured coupling efficiency as a function of crossing angle. We note that the side lobe in Figure 6.27 is about -21 dB and there is a difference between Figure 6.26 and 6.27. One reason is because the lower $1.4\ \mu\text{m}$ InGaAsP waveguide is a multimode waveguide. Multimode interference has occurred when the light is launched from this waveguide.

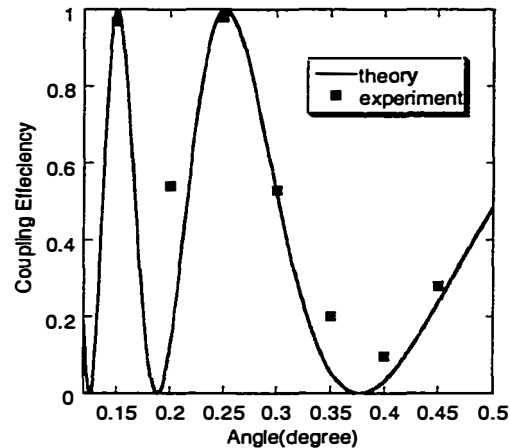


Figure 6.28. The coupling efficiency as a function of crossing angle.

6.5 Future work

6.5.1 Polarization insensitive vertical coupler filters

Based on X-crossing vertical coupler filters, we achieved optical add/drop multiplexers with a very low side lobe. However there is one obstacle to the widespread use of this devices: strong polarization dependence, which comes from the polarization dependent effective index of the two asymmetric waveguides. In a conventional vertical coupler filter, one of the waveguides has a

very small index difference between the core and the cladding, and a large core size, while the other one has a large index difference and a small core size. The difference in effective indices between TE and TM modes for a waveguide with a large index difference and small core is much larger than the TE and TM

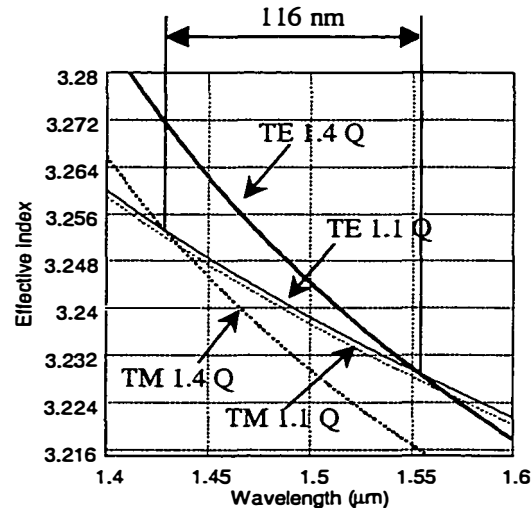


Figure 6.29. The effective indices of a 2D vertical coupler filter (see Figure 6.2) for TE and TM modes. There is 116 nm wavelength shift between the peak wavelengths of TE and TM modes.

difference of another waveguide with small index difference and large core size. Consequently, these devices have a strong polarization dependence. Figure 6.29 shows the calculated effective indices of a 2D vertical coupler filter (see Figure 6.2) for both TE and TM modes. Here, the polarization dependent wavelength shift is about 116 nm. This is a disadvantage in fiber optic communication systems. Several methods can be used to solve this problem. The direct way is to eliminate the birefringence of two waveguides. It is easy to realize it in the waveguide with a small index contrast and a large core size. But for the other waveguide with a very small core size ($<0.3 \mu\text{m}$) and a large index contrast, eliminating the birefringence and satisfying the phase matching condition at the same time will be very difficult. A birefringence compensation technique [30]

was introduced to solve this problem. But this needs a complicated structure design and a critical material growth. In grating assisted vertical coupler filters, one can fabricate the polarization independent devices by using double stage gratings [31].

In this section, we will propose two polarization insensitive optical add/drop multiplexers. One combines two different material systems: AlGaAs/GaAs with a low material dispersion at $1.55\mu\text{m}$ and InGaAsP with a very high material dispersion. Another uses double X-crossings.

A. InP/GaAs polarization insensitive vertical coupler filters

Since the polarization dependence comes from the strong asymmetry of two

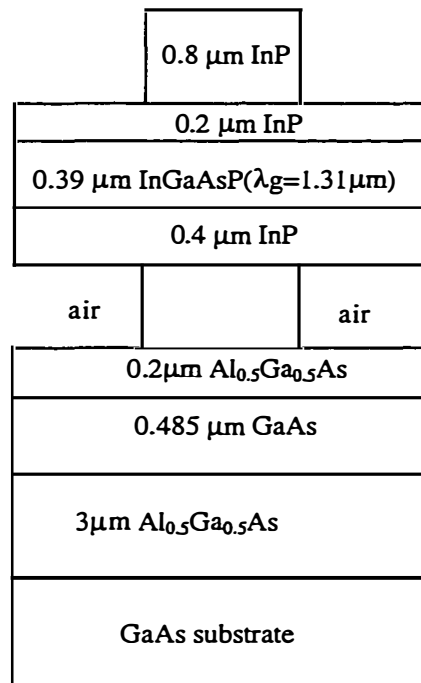


Figure 6.30. The structure of polarization insensitive InP/GaAs vertical coupler filter.

waveguide geometries, the problem can be solved if the two waveguides have

similar structure. For these waveguides with almost identical waveguide dispersions, a large material dispersion difference between two waveguides is needed to realize a narrowband polarization independent filter. It is known that a material has strong dispersion when the operation wavelength is near the bandgap. So InGaAsP/InP material can have much higher dispersion than AlGaAs/GaAs material around $1.55\mu\text{m}$ and $1.3\mu\text{m}$.

The detailed structure of the proposed fused vertical coupler filter is illustrated in Figure 6.30. The upper InGaAsP/InP waveguide consists of a $0.39\mu\text{m}$ InGaAsP ($\lambda_g=1.31\mu\text{m}$) guiding layer and an InP cladding layer. The lower AlGaAs/GaAs waveguide includes a $0.485\mu\text{m}$ GaAs core and a $0.2\mu\text{m}$

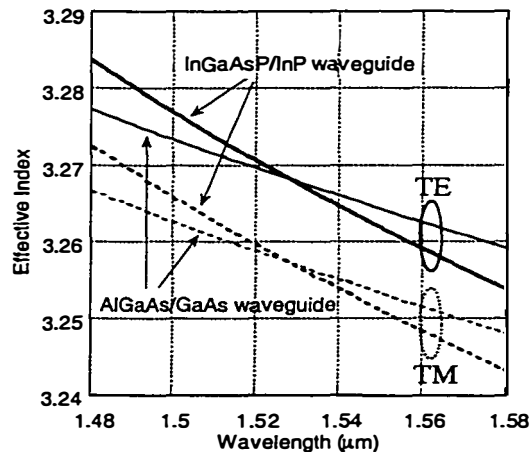


Figure 6.31. The calculated effective indices for TE and TM modes. They have the same peak wavelength.

$\text{Al}_{0.5}\text{Ga}_{0.5}\text{As}$ cladding layer. Those two waveguides are phase matched at $1.528\mu\text{m}$. Figure 6.31 shows the calculated effective indices of $3\mu\text{m}$ wide upper InGaAsP/InP and lower AlGaAs/GaAs waveguides. The waveguide dispersions of the two waveguides are very small and almost identical, so the material dispersion dominates in this vertical coupler filter. Because of similar waveguide structures, TE and TM modes have the same peak wavelength in this vertical

coupler filter. Since the material dispersion of $1.31 \mu\text{m}$ quaternary is lower than that of $1.4 \mu\text{m}$ quaternary, a certain bandwidth will be sacrificed in wavelength dependent filters. To fabricate this device, wafer bonding will be needed to integrate lattice mismatched InP and GaAs based waveguides together.

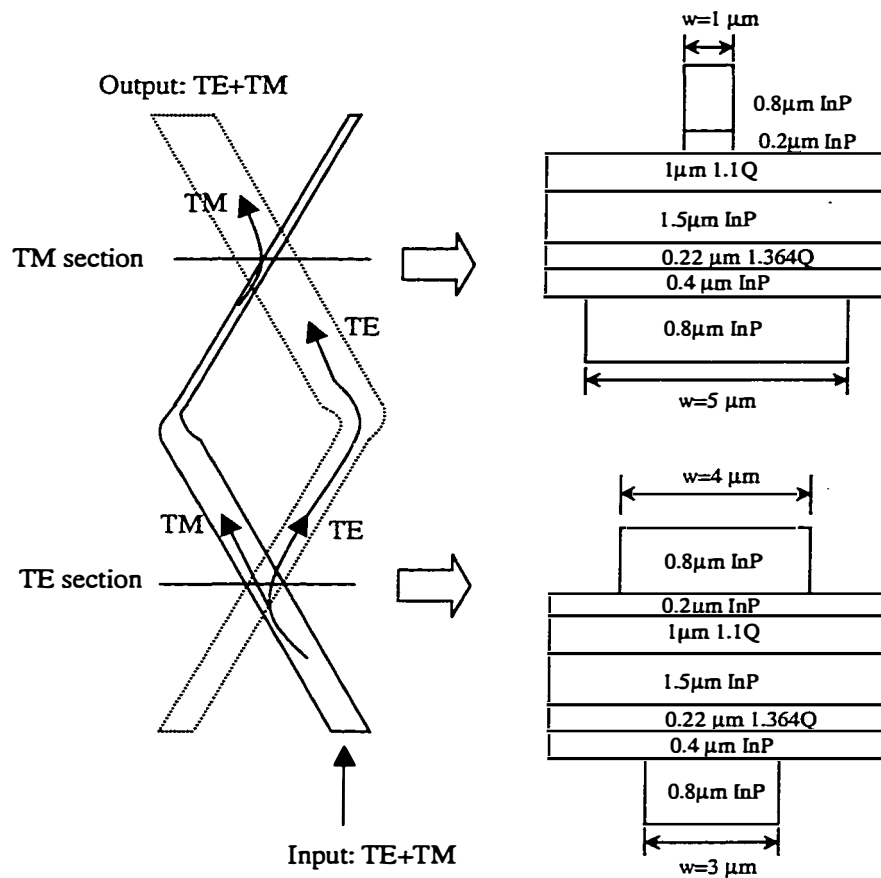


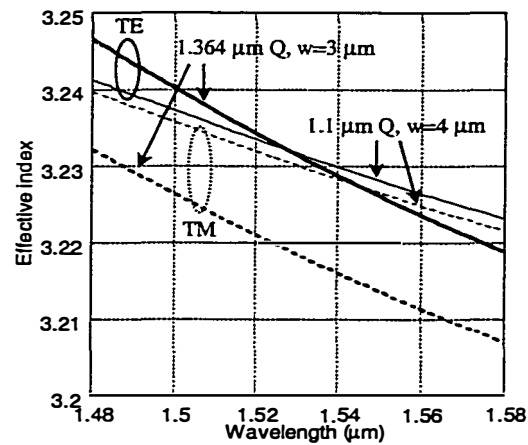
Figure 6.32. Schematic drawing of a double X-crossing structure for polarization independent add/drop filters and the detailed material structure in two X-crossing sections.

B. Double X-crossing polarization independent add/drop filters

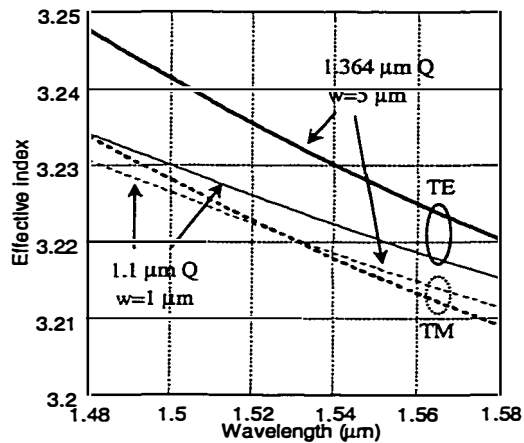
Since wafer bonding gives us an extra freedom to design and fabricate 3D devices, we can cascade two X-crossing vertical coupler filters together and adjust

the phase matching wavelength at each section to match both TE and TM modes. Figure 6.32 is the schematic drawing of a polarization independent add/drop multiplexer, which includes double X-crossing structures. If the input is to the upper waveguide (solid line), the TE wave whose wavelength matches the peak (λ_{TE}) of the first X-crossing filter will be coupled down to the lower waveguide (dash line) by the first X-crossing section (TE section). Because the peak wavelength (λ_{TM}) of TM mode is shorter than that of TE mode ($\lambda_{TE} - \lambda_{TM} > 80$ nm) (see Figure 6.32 (a)), the TM part will go straight through the TE section and is kept in the upper waveguide. In the second X-crossing section (TM section), if the TM mode peak wavelength is aligned to match the TE peak wavelength of the first X-crossing filter (see Figure 6.32 (b)), the TM wave will be coupled down to the lower waveguide. Since the TE wave has already coupled down to the lower waveguide and the TE peak of the TM section is at a very long wavelength (>1600 nm), it still stays in the lower waveguide. Therefore, a polarization independent add/drop filter can be realized.

To match the peak wavelength of both TE and TM modes, we should carefully design the waveguide structures at different sections. Figure 6.32 shows one example of the detailed structures at two sections. The difference between two lower waveguides, where the guiding layer is InGaAsP with bandgap at $1.364 \mu\text{m}$ is only the width: $3 \mu\text{m}$ for the TE mode and $5 \mu\text{m}$ for the TM mode. In the upper waveguide, where the material bandgap is $1.1 \mu\text{m}$, the width is $4 \mu\text{m}$ for the TE mode and $1 \mu\text{m}$ for the TM mode. Besides the width difference, the $0.2 \mu\text{m}$ InP cladding layer in the TM section is removed to assure the matching between TE and TM peak wavelengths.



(a) TE section



(b) TM section

Figure 6.33. The calculated effective indices for double X-crossing filter.

(a) TE section.

(b) TM section

The fabrication procedures of double X-crossing add/drop filters are very similar to that of the single X-crossing ones, except an extra etching needed to remove the $0.2 \mu\text{m}$ InP cladding layer after the fabrication of the upper waveguide.

6.5.2 Multichannel OADMs and wavelength selective cross-connect

In optical networking, multi-channel OADMs will be needed to add and drop

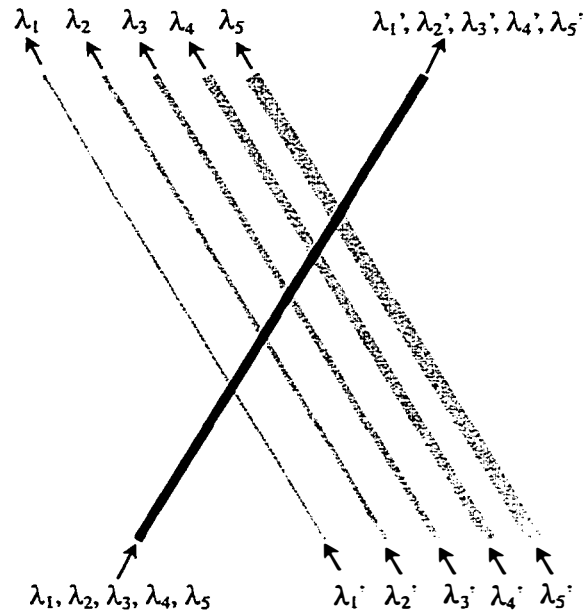


Figure 6.34. Schematic drawing of 5 channel optical add/drop multiplexer.

several wavelengths at a single node. Based on X-crossing vertical coupler filters, it is easy to fabricate multichannel optical add/drop multiplexers. Figure 6.34 is the schematic diagram of a 5 channel OADM. Instead of one lower waveguide, five waveguides with different widths cross over one upper waveguide in an X-shape. Since the phase matching point strongly depends on the waveguide parameters, the waveguides with different widths will have the different peak wavelengths. Figure 6.35 shows the calculated effective indices for different waveguides (the waveguide structure is the same as that in Figure 6.32). For lower waveguides with 1, 2, 3, 4 and 5 μm widths, the corresponding peak wavelengths are 1.509 μm , 1.522 μm , 1.534 μm , 1.542 μm and 1.549 μm respectively, which covers 40 nm wavelength range. Figure 6.36 is the

relationship between the peak wavelength and the lower waveguide width. By adding more waveguides with slight waveguide difference, we can achieve more

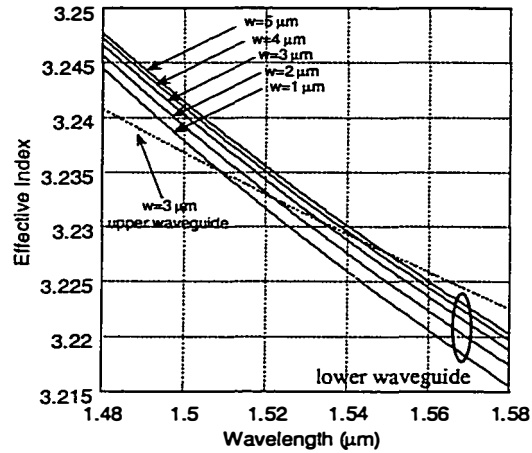


Figure 6.35. The calculated effective indices for different wide waveguides.

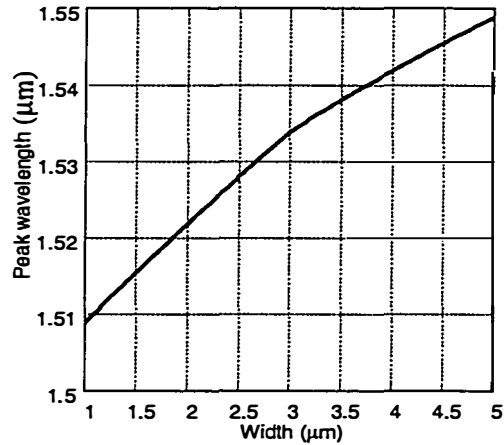


Figure 6.36. The peak wavelength as a function of waveguide width.

channels with narrow channel spacing.

Later generations of OADMs in optical networking will provide more dynamic capabilities: dynamic selection of which wavelengths are to be added or dropped at a node. In X-crossing vertical coupler filter based OADMs, we can bias each waveguide and change the waveguide index through the electrooptic

effect or carrier injection effect. Then the peak wavelength can be tuned in a wide wavelength range [19] [32]. Based on this tunable X-crossing filter, A simple

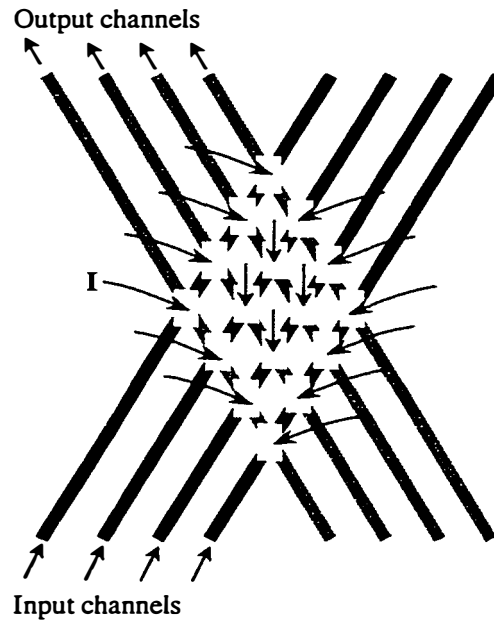


Figure 6.37. Schematic drawing of a crossbar wavelength selective cross connect.

reconfigurable dynamic OADM can be realized.

Furthermore, a full dynamic matrix switch, also referred to as a wavelength selective cross-connect, can be realized using X-crossing vertical coupler filters. Figure 6.37 is the schematic drawing of a proposed wavelength selective cross connect. In this device, two arrays of asymmetric waveguides are arranged to different planes in a crossbar configuration. Each crossing point is a dynamic OADM. Arbitrary input wavelengths can go to arbitrary output channels by the biases applied to each crossing point. This is a quite simple, fast and compact wavelength selective cross-connect.

6.6 Summary

In this chapter, a very simple OADM based on X-crossing InGaAsP/InP vertical coupler filters with laterally separated input and output waveguides has been successfully demonstrated. The sidelobe level has been reduced to -26 dB and the coupling efficiency is above 97%. To our knowledge, these are the best reported results so far for vertical coupler filters. Compared to other OADM structures, X-crossing vertical coupler filters can avoid complicated material regrowth and grating fabrication, making these filters attractive and low cost candidates for OADM in WDM networks. Some approaches to solve the problem of the polarization dependence were discussed and more applications of X-crossing vertical coupler filters were also described. Simple dynamic reconfigurable OADMs and wavelength selective cross-connect can be realized using this kind of X-crossing vertical coupler filters.

References

- [1] C. R. Giles and M. Spector, "The wavelength add/drop multiplexer for lightwave communication networks," *Bell Labs Technical Journal*, vol. 4, pp. 207-29, 1999.
- [2] M. Born, E. Wolf, *Principles of Optics*. New York: Macmillan, 1959.
- [3] T. Numai, "1.5 μ m optical filter using a two-section Fabry-Perot laser diode with wide tuning range and high constant gain," *IEEE Photonics Technol. Lett.*, vol. 2, pp. 401-3, 1990.
- [4] T. Numai, "1.5 μ m two-section Fabry-Perot wavelength tunable optical filter," *J. Lightwave Technol.*, vol. 10, pp. 1590-6, 1992.
- [5] N. Takato, T. Kominato, A. Sugita, K. Jinguji, H. Toba, and M. Kawachi, "Silica-based integrated optic Mach-Zehnder multi/demultiplexer family with channel spacing of 0.01-250 nm," *IEEE J. Sel. Areas Commun.*, vol. 8, pp. 1120-7, 1990.
- [6] J. Albert, F. Bilodeau, D. C. Johnson, K. O. Hill, K. Hattori, T. Kitagawa, Y. Hibino, and M. Abe, "Low-loss planar lightwave circuit OADM with high isolation and no polarization dependence," *IEEE Photonics Technology Letters*, vol. 11, pp. 346-8, 1999.
- [7] B. J. Offrein, G. L. Bona, F. Horst, W. M. Salemink, R. Beyeler, and R. Germann, "Wavelength tunable optical add-after-drop filter with flat passband for WDM networks," *IEEE Photonics Technology Letters*, vol. 11, pp. 239-41, 1999.
- [8] M. Zirngibl, C. H. Joyner, and B. Glance, "Digitally tunable channel dropping filter/equalizer based on waveguide grating router and optical amplifier integration," *IEEE Photonics Technol. Lett.*, vol. 6, pp. 513-15, 1994.

- [9] C. R. Doerr, L. W. Stulz, J. Gates, M. Cappuzzo, E. Laskowski, L. Gomez, A. Paunescu, A. White, and C. Narayanan, "Arrayed waveguide lens wavelength add-drop in silica," *IEEE Photonics Technology Letters*, vol. 11, pp. 557-9, 1999.
- [10] S. E. Harris and R. W. Wallace, "Acousto-optic tunable filter," *J. Opt. Soc. Am.*, vol. 59, pp. 744-7, 1969.
- [11] I. C. Chang, "Noncollinear acousto-optic filter with large angular aperture," *Appl. Phys. Lett.*, vol. 25, pp. 370-2, 1974.
- [12] B. L. Heffner, D. A. Smith, J. E. Baran, A. Yi-yan, and K. W. Cheung, "Integrated-optic acoustically tunable infra-red optical filter," *Electron. Lett.*, vol. 24, pp. 1562-3, 1988.
- [13] D. A. Pinnow, R. L. Abrams, J. F. Lotspeich, D. M. Henderson, T. K. Plant, R. R. Stephens, and C. M. Walker, "An electro-optic tunable filter," *Appl. Phys. Lett.*, vol. 34, pp. 391-3, 1979.
- [14] R. C. Alferness and R. V. Schmidt, "Tunable optical waveguide directional coupler filter," *Appl. Phys. Lett.*, vol. 32, pp. 161-3, 1978.
- [15] A. Shibukawa and M. Kobayashi, "Optical TE-TM mode conversion in double epitaxial garnet waveguide," *Appl. Opt.*, vol. 20, pp. 2444-50, 1981.
- [16] H. Kawaguchi, K. Magari, K. Oe, Y. Noguchi, Y. Nakano, and G. Motosugi, "Optical frequency-selective amplification in a distributed feedback type semiconductor laser amplifier," *Appl. Phys. Lett.*, vol. 50, pp. 66-7, 1987.
- [17] B. Broberg, B. S. Lindgren, M. G. Oberg, and H. Jiang, "A novel integrated optics wavelength filter in InGaAsP-InP," *J. Lightwave Technol.*, vol. 4, pp. 196-203, 1986.

- [18] R. C. Alferness, T. L. Koch, L. L. Buhl, F. Storz, F. Heismann, and M. J. R. Martyak, "Grating-assisted InGaAsP/InP vertical codirectional coupler filter," *Appl. Phys. Lett.*, vol. 55, pp. 2011-13, 1989.
- [19] R. C. Alferness, L. L. Buhl, U. Koren, B. I. Miller, M. G. Young, T. L. Koch, C. A. Burrus, and G. Raybon, "Broadly tunable InGaAsP/InP buried rib waveguide vertical coupler filter," *Applied Physics Letters*, vol. 60, pp. 980-2, 1992.
- [20] C. Wu, C. Rolland, F. Shepherd, C. Larocque, N. Puetz, K. D. Chik, and J. M. Xu, "InGaAsP/InP vertical directional coupler filter with optimally designed wavelength tunability," *IEEE Photonics Technology Letters*, vol. 5, pp. 457-9, 1993.
- [21] I. Kim, R. C. Alferness, L. L. Buhl, U. Koren, B. I. Miller, M. G. Young, M. A. Newkirk, M. D. Chien, T. L. Koch, G. Raybon, and C. A. Burrus, "InGaAs/InGaAsP MQW optical amplifier integrated with grating-assisted vertical-coupler noise filter," *IEEE Photonics Technol. Lett.*, vol. 5, pp. 1319-21, 1993.
- [22] L. L. Buhl, R. C. Alferness, U. Koren, B. I. Miller, M. G. Young, T. L. Koch, C. A. Burrus, and G. Raybon, "Grating assisted vertical coupler/filter for extended tuning range," *Electron. Lett.*, vol. 29, pp. 81-2, 1993.
- [23] M. Horita, S. Tanaka, H. Furuya, and Y. Matsushima, "A tunable and narrow-band optical add and drop multiplexer utilizing coupled semiconductor waveguides and a striped thin-film heater," , 1997.
- [24] M. Horita, S. Tanaka, and Y. Matsushima, "Wavelength tunable optical add and drop multiplexer utilizing coupled semiconductor waveguides and a striped thin-film heater," *Electronics Letters*, vol. 34, pp. 2240-1, 1998.

- [25] R. C. Alferness and P. S. Cross, "Filter characteristics of co-directionally coupled waveguides with weighted coupling," *IEEE J. Quantum Electron.*, vol. 14, pp. 843-7, 1978.
- [26] H. Sakata, "Sidelobe suppression in grating-assisted wavelength-selective couplers," *Opt. Lett.*, vol. 17, pp. 463-5, 1992.
- [27] B. E. Little, W. Chi, and H. Wei-Ping, "Synthesis of codirectional couplers with ultralow sidelobes and minimum bandwidth," *Optics Letters*, vol. 20, pp. 1259-61, 1995.
- [28] R. C. Alferness, "Optical directional couplers with weighted coupling," *Appl. Phys. Lett.*, vol. 35, pp. 260-2, 1979.
- [29] K. Matsumura and Y. Tomabechi, "Coupling characteristics of two rectangular dielectric waveguides laid in different layers," *IEEE J. Quantum Electron.*, vol. 22, pp. 959-63, 1986.
- [30] R. J. Deri, M. A. Emanuel, F. G. Patterson, S. P. Dijaili, and L. T. Nguyen, "Polarization-insensitive wavelength filters by birefringence compensation of vertical couplers," *Applied Physics Letters*, vol. 68, pp. 1037-9, 1996.
- [31] F. Heismann, L. L. Buhl, B. I. Miller, M. Newkirk, U. Koren, M. G. Young, and R. C. Alferness, "Polarization-independent wavelength filter using a grating-assisted vertical directional coupler in InP," *Appl. Phys. Lett.*, vol. 64, pp. 2335-7, 1994.
- [32] M. Oberg, S. Nilsson, K. Streubel, J. Wallin, L. Backbom, and T. Klinga, "74 nm wavelength tuning range of an InGaAsP/InP vertical grating assisted codirectional coupler laser with rear sampled grating reflector," *IEEE Photonics Technol. Lett.*, vol. 5, pp. 735-7, 1993.

Chapter 7

Summary

High performance and cost-effective photonic devices and circuits are the key enabling elements for optical access to traffic at each node in future optical transport networking. Compared to the development of EICs, the current PICs fall short of our expectation due to the nature of photonics and the technology limitations. The final success of PICs can be expected when the technology is mature for 3D multilevel photonic devices and circuits with an increased functionality and a large-scale integration. Although 3D optical interconnection is still in its infancy, wafer bonding is a good candidate for this purpose, because the bonded interface is both optically and electrically transparent. The goal of this dissertation is to explore the possible applications of wafer bonding to 3D photonic devices. We successfully demonstrated several novel 3D multilevel photonic devices and circuits. The main results reported in Chapter 2 through 6 are summarized in the following.

The history and applications of wafer bonding was briefly reviewed in Chapter 2. Optical propagation loss introduced by the bonded interface in optical waveguides was investigated. We found that there is about 1dB/cm excess loss in fused waveguides.

For the design and optimization of optical waveguide devices, effective and simple numerical techniques were given in Chapter 3, including the transfer matrix method, the effective index method, coupled mode theory, normal mode theory, and beam propagation method. Based on these methods, we studied the extinction ratio in a coupler with a very short coupling length. The extinction ratio is independent of the coupling length if the two input waveguides and output

waveguides of a coupler are well separated. The symmetry between two waveguides is the key factor to get a high extinction ratio.

Vertical couplers are the hearts of all devices and circuits we investigated in this dissertation. In Chapter 4, we first theoretically calculated the coupling length and extinction ratio for different vertical couplers. Then we fabricated fused vertical couplers with a short coupling length of $62\ \mu\text{m}$ at $1.55\ \mu\text{m}$. Finally a push-pull anti-phase fused vertical coupler switch with 12 V reverse bias switching voltage has been demonstrated by inverting the crystal symmetry macroscopically. As a comparison, no switching is observed for in-phase FVCs.

In Chapter 5, we demonstrated a simple 3D photonic circuit: multiple channel wavelength multiplexers using cascaded 3D vertical couplers. 14.5 nm channel spacing and 15 dB channel crosstalk for 4-channel multiplexers with a 6 mm long first stage coupler and 14mm total length was achieved. An 8-channel MUX/DEMUX was also fabricated. These coupler based wavelength multiplexers may be a low cost choice for coarse WDM applications.

In Chapter 6, simple optical add/drop multiplexers based on X-crossing vertical couplers with laterally separated input and output waveguides were proposed and fabricated. The sidelobe level has been reduced to -26 dB and the coupling efficiency is above 97%. These are the best reported results so far for vertical coupler filters. We also suggested some approaches to solve the problem of the polarization dependence, including integration of InP/InGaAsP and AlGaAs/GaAs waveguides together and cascading two X-crossing filters. More sophisticated photonic devices based on X-crossing vertical coupler filters for WDM network applications were also described. These include simple dynamic reconfigurable OADMs and wavelength selective cross-connect.

Since wafer bonding gives us an extra degree of freedom for the integration of different materials and structures, it is a potentially powerful tool for future novel and complex 3D photonic devices and circuits, as shown in this

dissertation. Our study is just the beginning, and more efforts are needed to address two aspects.

The first one is wafer bonding itself, including bonding equipment with very precise (submicron) alignment during bonding processes and low temperature bonding. In this dissertation, we used double-sided process to avoid alignment during the bonding. The alignment was done by infrared-lithography or a conventional aligner after opening the alignment mark windows. For high density and multilayer integration, this method has many limitations. The potential of wafer bonding will depend on the development of sophisticated bonding equipment. This dissertation focused on InP/InP bonding and all bonding was done around 630 °C. There is no thermal expansion problem. But once we want to bond different materials (such as Si, Glass, Polymer and III-V semiconductors) together, the different thermal properties will be a big issue for a high quality and large area bonding. To avoid this problem, low temperature or even room temperature bonding is a solution. Although there are several reports on low temperature bonding [1] [2] [3], the new feasible techniques are still a challenge.

In this dissertation, vertical couplers were used to route the optical signals between different waveguides and different layers. This requires that the two waveguides must be phase matched at least at the operation wavelength. Otherwise, gratings are needed to compensate the phase mismatching. This will limit the complexity and functionality of photonic circuits. If we can incorporate conventional optical elements, such as micro-mirrors, splitters, polarizers, and others, into the current semiconductor PICs, the routing of optical paths will be simple and the performance and functionality of PICs will be enhanced greatly. This is the second area in which future work is needed, especially the integration of micro electro-mechanical systems (MEMS) [4] [5] with semiconductor photonic devices. The integration of different material systems and the 3D

fabrications will be the key enabling steps to the realization of MOEMS (Micro-Opto-Electro-Mechanical Systems). Definitely, wafer bonding [3] and other monolithic or hybrid integration techniques will grow in importance as MOEMS gain more applications, such as large scale optical switching, and optical cross connects.

References

- [1] Q. Y. Tong, U. Gosele, T. Martini, and M. Reiche, "Ultrathin single-crystalline silicon on quartz (SOQ) by 150 degrees C wafer bonding," *Sensors and Actuators A (Physical)*, vol. A48, pp. 117-23, 1995.
- [2] H. Takagi, R. Maeda, N. Hosoda, and T. Suga, "Room-temperature bonding of lithium niobate and silicon wafers by argon-beam surface activation," *Applied Physics Letters*, vol. 74, pp. 2387-9, 1999.
- [3] U. Gosele, Q. Y. Tong, A. Schumacher, G. Krauter, M. Reiche, A. Plossl, P. Kopperschmidt, T. H. Lee, and W. J. Kim, "Wafer bonding for microsystems technologies," , 1999.
- [4] S. T. Picraux and P. J. McWhorter, "The broad sweep of integrated microsystems," *IEEE Spectrum*, vol. 35, pp. 24-33, 1998.
- [5] M. C. Wu, L. Fan, and L. Shi-Sheng, "Optical MEMS: huge possibilities for Lilliputian-sized devices," *OPN Optics & Photonics News*, vol. 9, pp. 25-9, 1998.

Appendix A

Waveguide Loss Measurement

The simplest method for evaluating waveguide insertion loss is the measurement of their attenuation using transmission experiments. The ratio of output optical intensities yields the overall insertion loss, which includes both coupling and on-chip propagation losses. The standard approach "cutback method" [1] has been used to measure the loss as a function of guide length. But cutback method is not suitable for waveguides with very low losses. The major difficulty with this technique is input and output coupling reproducibility, especially for semiconductor waveguides where the mode size is smaller than the one in fibers and results in more severe alignment tolerance. Coupling reproducibility thus limits the overall accuracy of this method, particularly when sample length is varied to separate the effects of propagation and coupling losses. A second difficulty is caused by waveguide endfacet reflections, which give rise to resonator effects that significantly complicate the data analysis. Such resonator effects can be avoided by antireflection (AR) coating the endfacets.

In order to circumvent problems with coupling reproducibility, on-chip losses can be measured using Fabry-Perot resonant methods [2] [3]. This technique relies on cleaved waveguide endfacets to form a Fabry-Perot waveguide resonator, the finesse of which is measured by varying the waveguide phase using thermal, wavelength, or electrooptic tuning. The transmission T and reflection R of such a waveguide resonator, consisting of a straight waveguide of uniform propagation loss α and length L are given by:

$$T = \frac{(1 - R)^2 e^{-\alpha L}}{(1 - R e^{-\alpha L})^2 + 4 R e^{-\alpha L} \sin^2\left(\frac{\delta}{2}\right)} \quad (\text{A.1})$$

$$\text{Re} = \frac{R(1 - e^{-\alpha})^2 + 4\text{Re}^{-\alpha} \sin^2\left(\frac{\delta}{2}\right)}{(1 - \text{Re}^{-\alpha})^2 + 4\text{Re}^{-\alpha} \sin^2\left(\frac{\delta}{2}\right)} \quad (\text{A.2})$$

where $R = \sqrt{R_1 R_2}$, R_1 and R_2 are the endfacet reflectivities, $\delta = 2\beta L$ is the phase, β is the propagation constant. By measuring the fringe contrast K :

$$K = \frac{T_{\max}}{T_{\min}} = \left(\frac{1 + \text{Re}^{-\alpha}}{1 - \text{Re}^{-\alpha}}\right)^2 \quad (\text{A.3})$$

$\text{Re}^{-\alpha}$ can be determined. Since (A.3) shows no dependence on the coupling, coupling reproducibility problems are avoided. Using assumed facet reflectivity value R , the propagation loss α can be deduced. Figure A.1 shows the measured

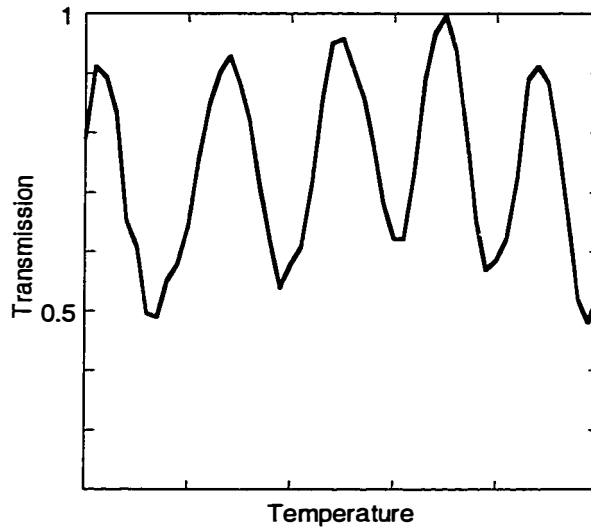


Figure A.1. The transmission of a waveguide F-P resonator.

F-P resonance with temperature change. In general, however, the waveguide reflectivity differs from the simple Fresnel value so that use of estimated R leads to inaccurate α results. An improved version of the F-P method involves multiple

measurements of the fringe constant K for different sample lengths L [4]. From (A.3),

$$\ln\left(\frac{\sqrt{K}-1}{\sqrt{K}+1}\right) = \ln R - \alpha L \quad (\text{A.4})$$

then R and α can be independently determined from a plot of the left-hand side of Equation (A.4) versus L .

Another way to determine both the loss and the reflectivity is to measure the transmission and reflection at the same time [5]. By measuring the fringe contrast of both the transmission K_{trans} and reflection K_{reflec} , one can find:

$$K_{trans} = \frac{T_{max}}{T_{min}} = \left(\frac{1 + Re^{-\alpha}}{1 - Re^{-\alpha}}\right)^2 \quad (\text{A.5})$$

$$K_{reflec} = \frac{Re_{max}}{Re_{min}} = \left(\frac{1 + Re^{-\alpha}}{1 - Re^{-\alpha}}\right)^2 \left(\frac{1 - e^{-\alpha}}{1 + e^{-\alpha}}\right)^2 \quad (\text{A.6})$$

so, one gets:

$$\gamma = \frac{K_{reflec}}{K_{trans}} = \left(\frac{1 - e^{-\alpha}}{1 + e^{-\alpha}}\right)^2 \quad (\text{A.7})$$

Form (A. 7) and (A.5), the loss and reflectivity can be deduced directly:

$$e^{-\alpha} = \frac{1 - \sqrt{\gamma}}{1 + \sqrt{\gamma}} \quad (\text{A.9})$$

$$R = \frac{\sqrt{K_{trans}} - 1}{(\sqrt{K_{trans}} + 1)e^{-\alpha}} \quad (\text{A.10})$$

Compared to the multiple measurements of transmission for different waveguide lengths, this method is simpler and more efficient.

The major advantage of the F-P resonance technique is its inherent reproducibility and insensitivity to coupling misalignment. This permits more accurate measurements of small on chip losses.

References

- [1] S. H. Lin, S. Y. Wang, S. A. Newton, and Y. M. Houn, "Low-loss GaAs/GaAlAs strip-loaded waveguides with high coupling efficiency to single-mode fibres," *Electron. Lett.*, vol. 21, pp. 597-8, 1985.
- [2] R. G. Walker, "Simple and accurate loss measurement technique for semiconductor optical waveguides," *Electron. Lett.*, vol. 21, pp. 581-3, 1985.
- [3] H. Takeuchi and K. Oe, "Low-loss single-mode GaAs/AlGaAs miniature optical waveguides with straight and bending structures," *J. Lightwave Technol.*, vol. 7, pp. 1044-54, 1989.
- [4] E. Kapon and R. Bhat, "Low-loss single-mode GaAs/AlGaAs optical waveguides grown by organometallic vapor phase epitaxy," *Appl. Phys. Lett.*, vol. 50, pp. 1628-30, 1987.
- [5] K. H. Park, M. W. Kim, Y. T. Byun, D. Woo, S. H. Kim, S. S. Choi, Y. Chung, W. R. Cho, S. H. Park, and U. Kim, "Nondestructive propagation loss and facet reflectance measurements of GaAs/AlGaAs strip-loaded waveguides," *Journal of Applied Physics*, vol. 78, pp. 6318-20, 1995.

Appendix B

Characteristic Equations for Different ARROW Structures

B.1 Introduction

Antiresonant reflecting optical waveguides (ARROW)[1] have attracted a great deal of interest during the past several years. Instead of total internal reflection in conventional waveguides, ARROWs use antiresonant reflection as the guiding mechanism. This gives ARROWs some remarkable features that are used in many applications, such as remote couplers [1], filters [2], and polarization splitters [3]. In order to design ARROW devices, the knowledge of the characteristics of ARROW modes is important. An approximate expression for the propagation constant and loss have been given by Baba *et al.* [4, 5]. The equivalent transmission line [6] and the transverse resonance method [7] have also been used to investigate the dispersion and loss. A rigorous numerical method is based on a well known transfer matrix method [8, 9]. Because of the leaky property of ARROW modes, the solutions must be found in the complex plane. The root searching in the complex plane could be time consuming and tedious, especially for optimization of multiple layer structures. In this appendix, we will give a set of simple characteristic equations for ARROW structures [10]. The root searching for the new equations needs to be carried only on the real axis and the error is negligible for low loss ARROW modes of practical interest (i.e. loss smaller than a few dB/cm).

B.2 Characteristic Equations

We consider a planar multilayer waveguide as shown in Fig. B.1. The general solution of the wave equation in each layer is well known (see Chapter 3 section 2):

$$E_{y,j} = A_j \exp(k_j(x-x_j)) + B_j \exp(-k_j(x-x_j)) \quad (\text{B.1})$$

Based on transfer matrix method (see 3.2), we can relate field coefficients in the cover (A_c and B_c) with the coefficients in the substrate (A_s and B_s):

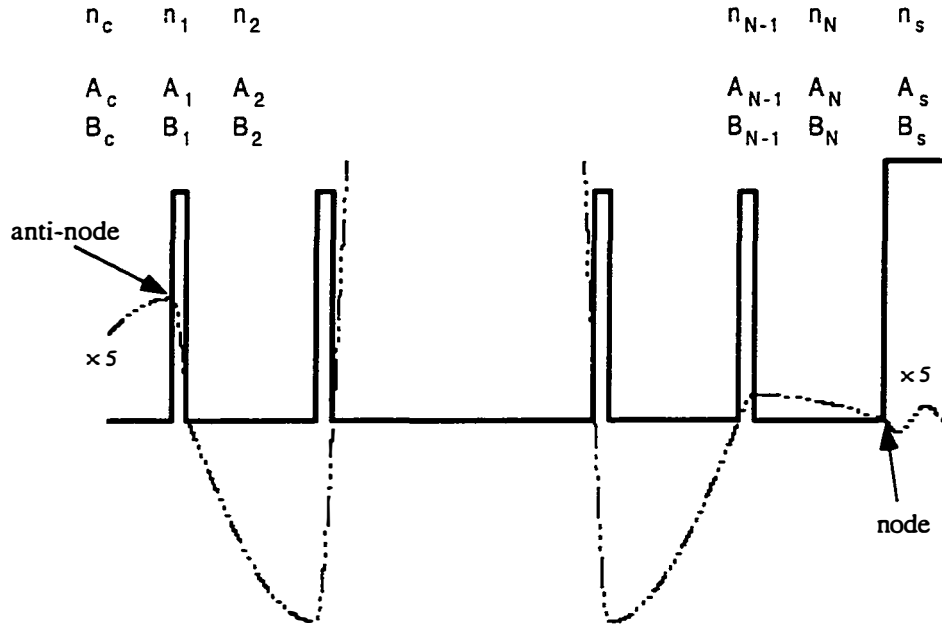


Figure B.1. Schematic diagrams of a planar ARROW structure and the field profile (dash line).

$$\begin{bmatrix} A_s \\ B_s \end{bmatrix} = T \begin{bmatrix} A_c \\ B_c \end{bmatrix} \quad (\text{B.2})$$

$$T = T_N \cdots T_1 T_c = \begin{bmatrix} t_{11} & t_{12} \\ t_{21} & t_{22} \end{bmatrix}$$

For guiding modes, fields should be evanescent in the cap and the substrate layers, so $A_s=0$ and $B_c=0$ that results in the characteristic equation:

$$t_{11}(\beta)=0 \quad (\text{B.3})$$

For ARROW modes, since they are leaky, characteristic equation $t_{11}(\beta)=0$ can be found by assuming outgoing waves in the cover and substrate layers, with correct sign of k_c and k_s chosen [8]. The root β resides in the complex plane, so the root searching for structures with many layers and for optimization purposes could be time consuming and tedious. In the following, based on physical arguments, we will introduce a different characteristic equation for the radiation modes, that gives the ARROW mode effective indices on the real axis.

Radiation modes require both incoming and outgoing components to form standing waves in the substrate layer for one sided radiation modes, or in both cover and substrate layers for two sided radiation modes. Equation (B.1) holds for radiation modes as well. Since the number of unknown variables is larger than the number of boundary conditions, a characteristic equation can not be established. A simple relation between A_s (A_c) and B_s (B_c) will allow us to get a characteristic equation for the case of low loss ARROW modes. When the interference layers in ARROW waveguides satisfy the antiresonant condition, the reflectivity is very close to unity and the phase shift in each layer is 90 degrees. This assures that the field at the outermost interface is a node or an anti-node, i.e., $A_s = \pm B_s$ (or $A_c = \pm B_c$) for one sided radiation modes and $A_s = \pm B_s$, $A_c = \pm B_c$ for two sided radiation modes from equation (B.1). The sign depends on the index of the outermost two layers.

Now, let's look at each case separately:

(a) One sided ARROW modes

In one sided ARROWs, the field in one side (cover) is evanescent $B_c=0$ and in the other side (substrate) is a standing wave (actually the amplitude of the “mode” increases with the distance because of its lossy nature), i.e. $n_{eff}>n_c$ and $n_{eff}<n_s$. When the substrate index is larger than that of the last layer, $n_s>n_N$ (the right side of Fig. B.1), the field in the outmost interface is a node, $A_s=-B_s$. From (B.2) we get the characteristic equation:

$$t_{11}+t_{21}=0 \quad (B.4)$$

When the index of substrate is smaller than that of the last film layer $n_s<n_N$, the field in the outermost interface is a anti-node (the left side of Fig. 1), $A_s=B_s$. So

$$t_{11}-t_{21}=0 \quad (B.5)$$

(b) Two sided ARROW modes

In two sided ARROW, the field in both sides are standing waves, i.e. $n_{eff}<n_c$ and $n_{eff}<n_s$. There are three cases:

- $n_s>n_N$ and $n_c>n_1$. In this case, $A_s=-B_s$ and $A_c=-B_c$, so

$$t_{11}-t_{12}+t_{21}-t_{22}=0 \quad (B.6)$$

- $n_s>n_N$ and $n_c<n_1$ (Fig. 1) or $n_s<n_N$ and $n_c>n_1$, $A_s=-B_s$ and $A_c=B_c$ or $A_s=B_s$ and $A_c=-B_c$, so

$$t_{11}+t_{12}+t_{21}+t_{22}=0 \quad (B.7)$$

- $n_s<n_N$ and $n_c<n_1$, $A_s=B_s$ and $A_c=B_c$, so

$$t_{11}+t_{12}-t_{21}-t_{22}=0 \quad (B.8)$$

The above equations (B.3)-(B.8) are the characteristic equations for all kinds of ARROW structures. For all of these the effective index for guided (Equation (B.3)) and leaky modes (Equations (4)-(8)) for lossless materials can be found on the real axis. After finding the mode's effective index, it is simple to get its profile if we choose the correct A_c and B_c . Based on the first order

perturbation theory, the loss of leaky modes can be found:

$$\alpha = 4.34k_0 \operatorname{Im} \left[\frac{t_{11}(n_{\text{eff}})}{t'_{11}(n_{\text{eff}})} \right] \text{ dB}/\mu\text{m},$$

where Im is the imaginary part, $t'_{11}(n_{\text{eff}})$ is the

differential with respect to n_{eff} .

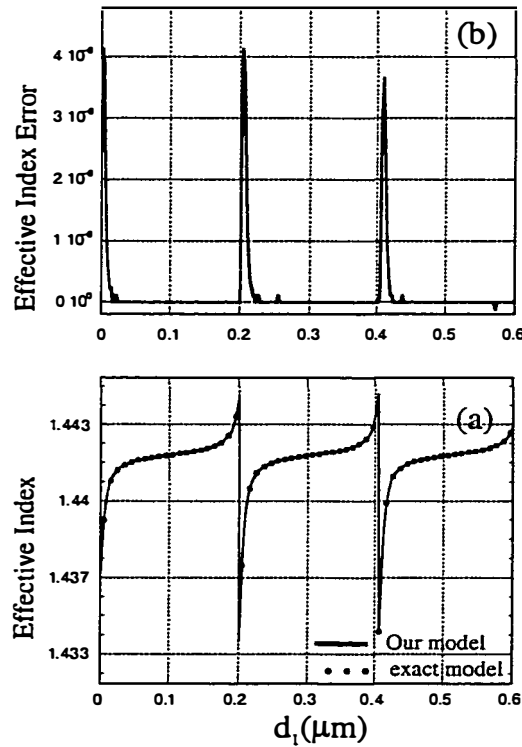


Figure B.2. The calculated effective index (a) of the TE_0 mode of ARROW-A structure as a function of the thickness of the first antiresonant layer. (b) is the error in our model comparing to the exact calculations.

B.3 Examples

In order to check the accuracy of our characteristic equations for different ARROW structures, we have compared the calculations with the exact model [8, 9]. Figure B.2 (a) (b) (c) and (d) show the calculated effective index, loss and error as a function of the first interference layer thickness d_1 of an ARROW-A

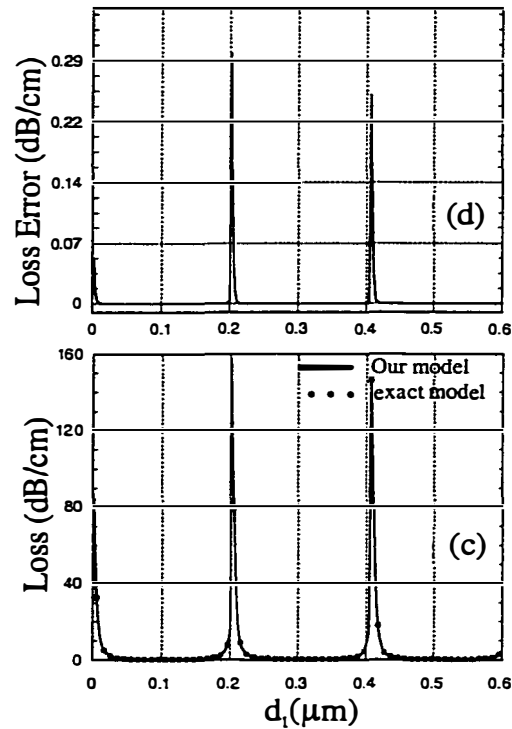


Figure B.2, continued. The calculated loss (c) of TE_0 mode of ARROW-A structure as a function of the thickness of the first antiresonant layer. (d) is the error in our model comparing to the exact calculations.

structure using our method and the exact model [8, 9]. Although this model is based on an antiresonant condition, our computation shows that antiresonance is not critical. Even when the thickness d_1 is far away from the antiresonant condition, the current model matches the exact calculations very well (see Figure B.2). For example, when d_1 is around the resonant point where loss is the highest, the error between our method and the exact model is still smaller than 0.2% for TE_1 mode. Table B.1 displays the effective index and loss for several ARROW waveguides including ARROW-B [5], two sided ARROWs and ARROW couplers [11]. We can see that for low loss ARROW modes, which are of main

interest in practical applications, the approximate model with real roots is identical to the exact analysis.

Structure*	Characteristic equation	mode	Effective index (this study)	Loss (dB/cm) (this study)	Effective index (exact)	Loss (dB/cm) (exact)
One sided ARROW-A	$t_{11}+t_{21}=0$	TE1	1.4417085	0.25	1.4417085	0.25
		TE2	1.41798	270	1.4176	407
One sided ARROW-B	$t_{11}+t_{21}=0$	TE1	1.5382528	0.11	1.5382527	0.11
		TE2	1.5336896	95	1.5336856	98
Two sided ARROW 1	$t_{11}-t_{12}+t_{21}-t_{22}=0$	TE1	1.4578523	0.11	1.4578523	0.11
		TE2	1.4518589	76	1.4518454	98
Two sided ARROW 2	$t_{11}+t_{12}-t_{21}-t_{22}=0$	TE1	3.1540497	0.53	3.1540497	0.53
		TE2	3.1393856	103	3.1393856	113
Two sided ARROW 3	$t_{11}+t_{12}+t_{21}+t_{22}=0$	TE1	1.4578558	0.06	1.4578558	0.06
		TE2	1.4518726	49	1.4518551	58
ARROW coupler	$t_{11}-t_{21}=0$	even	3.1541037	0.12	3.1541037	0.12
		odd	3.1539980	0.14	3.1539980	0.14

Table B.1. Comparison of the effective index and loss between our model and exact model

* The structures (index, thickness (from the cap to substrate layers) and wavelength) of calculated ARROWs are listed below:

1. ARROW-A: $n=1/1.45/3.5/1.45/3.5$; $d=\infty/4/0.1019/2.0985/\infty/\mu\text{m}$; $\lambda=1.3\mu\text{m}$ [6, 7, 9].
2. ARROW-B: $n=1/1.54/1.46/1.54/3.85$; $d=\infty/4/0.3/2/\infty/\mu\text{m}$; $\lambda=0.633\mu\text{m}$ [5].
3. Two sided ARROW 1: $n=3.8/1.46/2.3/1.46/2.3/1.46/3.8$;
 $d=\infty/2/0.088/4/0.088/2/\infty/\mu\text{m}$; $\lambda=0.633\mu\text{m}$.
4. Two sided ARROW 2: $n=3.16/3.55/3.16/3.55/3.16/3.55/3.16/3.55/3.16$;
 $d=\infty/0.237/2/0.237/4/0.237/2/0.237/\infty/\mu\text{m}$; $\lambda=1.55\mu\text{m}$
5. Two sided ARROW 3: $n=1.46/2.3/1.46/2.3/1.46/2.3/1.46/3.5$;

$$d = \infty / 0.089 / 2 / 0.089 / 4 / 0.089 / 2 / \infty / \mu\text{m}; \lambda = 0.6328 \mu\text{m}.$$

6. ARROW coupler:

$$n / 1 / 3.16 / 3.55 / 3.16 / 3.55 / 3.16 / 3.55 / 3.16 / 3.55 / 3.16 / 3.55 / 3.16 /;$$

$$d / \infty / 2 / 0.237 / 4 / 0.237 / 2 / 0.237 / 4 / 0.237 / 2 / \infty /; \lambda = 1.55 \mu\text{m} [11].$$

B.4 Conclusion

In this appendix, a set of simple and versatile characteristic equations is given for different ARROW structures. This method gives the precise effective index, loss and mode profile for low loss ARROW modes of practical interest (i.e. when their loss is smaller than a few dB/cm). This enables root searching in the real domain. The physical argument is simply based on the property of antiresonance and the small loss, which means that the reflection coefficient at the outermost boundaries is near 1, and a phase relation exists for the field at the outermost layers. The use of these characteristic equations is demonstrated for different ARROW waveguides, couplers and filters. This simple physical argument gives an accurate intuitive picture for low loss leaky modes and it can be used to design and optimize ARROW devices.

References

- [1] J. Gehler, A. Brauer, and W. Karthe, "Remote coupling over 93 μm using ARROW waveguides in strip configuration," *Electronics Letters*, vol. 30, pp. 218-20, 1994.
- [2] S. T. Chu, M. Miura, and Y. Kokubun, "Compact ARROW-type vertical coupler filter," *IEEE Photonics Technology Letters*, vol. 8, pp. 1492-4, 1996.
- [3] U. Trutschel, F. Ouellette, V. Delisle, M. A. Duguay, G. Fogarty, and F. Lederer, "Polarization splitter based on antiresonant reflecting optical waveguides," *Journal of Lightwave Technology*, vol. 13, pp. 239-43, 1995.
- [4] T. Baba, Y. Kokubun, T. Sakaki, and K. Iga, "Loss reduction of an ARROW waveguide in shorter wavelength and its stack configuration," *Journal of Lightwave Technology*, vol. 6, pp. 1440-5, 1988.
- [5] T. Baba and Y. Kokubun, "Dispersion and radiation loss characteristics of antiresonant reflecting optical waveguides-numerical results and analytical expressions," *IEEE Journal of Quantum Electronics*, vol. 28, pp. 1689-700, 1992.
- [6] J. Wenyan, J. Chrostowski, and M. Fontaine, "Analysis of ARROW waveguides," *Optics Communications*, vol. 72, pp. 180-6, 1989.
- [7] W. Huang, R. M. Shubair, A. Nathan, and Y. L. Chow, "The model characteristics of ARROW structures," *Journal of Lightwave Technology*, vol. 10, pp. 1015-22, 1992.
- [8] J. Chilwell and I. Hodgkinson, "Thin-films field-transfer matrix theory of planar multilayer waveguides and reflection from prism-loaded waveguides," *Journal of the Optical Society of America A*, vol. 1, pp. 742-53, 1984.

- [9] J. Kubica, D. Uttamchandani, and B. Culshaw, "Modal propagation within ARROW waveguides," *Optics Communications*, vol. 78, pp. 133-6, 1990.
- [10] B. Liu, "Characteristic Equations for Different ARROW Structures," *Optical and quantum electronics*, 1999.
- [11] C. Yeong-Her and H. Yang-Tung, "Coupling-efficiency analysis and control of dual antiresonant reflecting optical waveguides," *Journal of Lightwave Technology*, vol. 14, pp. 1507-13, 1996.